INTERROGATING ELECTROCATALYTIC MECHANISMS AND DEVELOPING NANO-POROUS CATALYSTS FOR ENERGY CONVERSION REACTIONS:
I. OXYGEN EVOLUTION REACTION, AND
II. CARBON DIOXIDE REDUCTION REACTION

BY

THAO THI HUONG HOANG

DISSERTATION

Submitted in partial fulfillment of the requirements
for the degree of Doctor of Philosophy in Chemistry
in the Graduate College of the
University of Illinois at Urbana-Champaign, 2016

Urbana, Illinois

Doctoral Committee:

Professor Andrew A. Gewirth, Chair
Assistant Professor Joaquín Rodríguez-López
Professor Ralph G. Nuzzo
Professor Paul A. J. Kenis

Abstract

The objectives of my thesis were to interrogate electrocatalytic mechanisms and develop new nano-porous catalysts for energy conversion reactions including the oxygen evolution reaction (OER) and carbon dioxide reduction reaction (CRR). First, I examined the oxygen evolution reaction in basic electrolytes using in situ electrochemical surface stress measurements. Second, I developed a new electrolyte additive-controlled electrodeposition method for the preparation of porous films of Ni and NiFe catalysts with high OER activity. Third, I exploited the additive-controlled electrodeposition method to synthesize Cu and CuAg films with high surface area and tunable morphology for high activity and selectivity of CRR to ethylene.

In Chapter 1, I provide background information to the electrochemical energy conversion reaction and lay out the challenges and potential approaches at present in the field.

In Chapter 2, I describe our effort to determine the relationship between changes in the OER catalyst surface and activity. In situ electrochemical surface stress measurements were utilized to interrogate oxide formation before and during OER on several common catalysts, including Ir, Ni, Co, Au, and Pt. The stress measurements report directly on changes in oxidation state and phase of the electrode material as the potential is varied. Hysteresis observed in the potential-dependent stress with Ir, Au and Pt electrodes is associated with irreversible composition and roughness changes in the electrode. The stress data also quantitatively reports on the in-plane change in strain developing in bonding during oxide oxidation. The magnitude of the surface stress is nearly identical to that the predicted from bond strains obtained from reported XAS data. Interestingly, there is a rough linear relationship between the change in stress and the amount of oxide formed. More importantly, the stress data shows that metals with higher activity exhibit

larger stress and more oxide formation. The origin of this relationship could be explained by differences in conductivity and porosity of different oxides.

In Chapter 3, I focus on developing a stable and effective OER catalyst using an additive-controlled electrodeposition. We find that 3,5-diamino-1,2,4-triazole (DAT) acts as a deposition inhibitor that dramatically changes Ni morphology resulting in black Ni films, a phenomenon indicative of small particle formation. Ni films electrodeposited with DAT (NiDAT) exhibit much higher active surface areas with fractal-like behavior. Correspondingly, NiDAT films show a much larger oxidation wave and higher OER rates compared to the Ni film deposited without the DAT additive. Co-electrodeposition of Ni and Fe in the presence of DAT (NiFeDAT) is also explored as Fe is known to increase the OER activity from Ni films. NiFeDAT films are very active toward OER exhibiting 100 mA/cm^2 with high stability > 72 hours at 1.50V vs RHE in 1 M NaOH. These metrics make NiFeDAT among the most active OER electrocatalyst reported to date. Equally important, the high activity can be tuned to nearly any arbitrary value by altering the amount of NiFe electrodeposited without film degradation.

In Chapter 4, I present electrochemical measurements that examine the effect of deuteration on the OER with Ni and Co catalysts, and an effort to identify the rate-determining step (RDS) of these intricate electrocatalytic reactions involving multiple proton-coupled electron transfer (PCET) processes. The OER Tafel slope and kinetic isotope effect (KIE) calculated from electrochemical data shows that both Ni and Co exhibits inverse secondary KIE, which is never observed before in an electrochemical experiment. These results contribute to a more complete understanding of the OER mechanism and allow for the future development of improved nonprecious-metal catalysts.

In Chapter 5, I discuss exploiting the additive-controlled electrodeposition method to synthesize Cu films with high surface area and tunable morphology for high activity and selectivity of CRR to ethylene. Electrodeposition of Cu films from plating baths containing DAT (CuDAT) as an inhibitor exhibit high surface area and high CO_2 reduction activities. By changing pH and deposition current density, the morphologies of the Cu films are varied to exhibit wires, dots, or amorphous structures. Among these Cu films, the CuDAT-wire samples exhibit the best CO_2 reduction activity with a Faradaic efficiency (FE) of the C_2H_4 product formation reaching 41% at -0.47 V vs. RHE, a FE for C_2H_5OH formation reaching 22% at -0.55 V vs. RHE, and a mass activity for CO_2 reduction at -0.65V vs. RHE of ~ 720 A/g.

In Chapter 6, I present our strategy to enhance C2 production from CO_2 electroreduction by doping low Ag contents (<10%) into Cu-wire film. The CuAg-wire catalyst with nanoporous structure and homogenous mixed of Cu and Ag atoms was fabricated by additive-controlled electrodeposition method using DAT. The CuAg-wire catalyst exhibits large active surface and high selectivity of CO2 reduction to C2H4 (~60% Faradaic efficiency - FE) and C2H5OH (~25% FE) at relatively low overpotential (~ -0.7V vs RHE).

To my Family and Friends,

especially Toan, who is both

Acknowledgements

Words cannot begin to express my sincere thanks and appreciation to all of my amazing family, teachers and friends, without whom this dissertation would not be possible.

First and foremost, I would like to thank my advisor, Professor Andrew A. Gewirth, who believed in me and provided guidance to become a good researcher. Thank you Andy, for accepting me to be your student, for teaching me about the research process, paper writing, and oral presentations, for providing me opportunity and the resources to make my research possible, and for all of your advice in science and in life. You are an amazing mentor, I am very grateful to work with you, and learn from you in last five years. Also I would like to thank the professors in my committee, Professor Paul A. J. Kenis, Professor Ralph G. Nuzzo, and Professor Joaquín Rodríguez-López, for their time, insights and helpful feedbacks during my graduate studies.

Next, I would like to thank my undergraduate research advisors in HUS, Professor Hoan Xuan Nguyen and Professor Ha Cam Nguyen for providing me a solid foundation in undergraduate research which inspired me to pursue graduate school. I owe my sincerest gratitude to Professor Alexander Scheeline, Professor James Lisy, Professor Martin Gruebele, and Professor Steven Zimmerman for going to HUS to teach me Chemistry, for helping me go to UIUC for summer research, and for encouraging me to go to graduate school. I would not be where I am now without your support and guidance.

I would also like to thank all Gewirth Group member, who are not only my labmates but also my closest friends. Thank you to Yeyoung Ha for being my friend, for bringing me closer to other members, for all of your awesome drinks, and for all of our fights which prove nothing but

the fact that we care about each other. Thank you to Dr. Claire Tornow and Dr. Laura Huff, and Dr. Hadi Tavassol for introducing me to electrochemistry when I first jointed the group. Thank you to Dr. Kevin Schmitt, Bruno Nicolau and Ryan Rooney for teaching me and discussing with me about Raman experiments. Thank you to Dr. Justin Oberst, Dr. Edmund Tse, Dr. Jen Esbenshade, Dr. Kimberly A. See, Jason Varnell and Kimberly Lundberg for your time and effort to help me improve my writing. Thank you to Dr. Heng-Liang Wu for sharing your experience on research and job searching. Thank you to Kim Ta for sharing Vietnamese home food with me making me feel less home sick. Thank you to Owen Liu, Minjeong Shin, Angela DiAscro, Dr. Lingzi Sang and Dr Teng Zhang for being wonderful labmates. Thank you all for being by my side making graduate school more fun.

During my time at UIUC, I had the opportunity to collaborate with Dr. Yair Cohen - visiting scholar from Israel and many members in the Kenis Group and Nuzzo Group. I thank Dr. Yair Cohen from Israel, Dr Mike Cason and Dr David Wesel from Nuzzo group for a productive collaboration on in situ surface stress measurement projects. I also appreciate the time and effort that Dr. Sichao Ma and Sumit Verma from Kenis group spent with me on CO_2 reduction projects. I have enjoyed working with you and also learned a lot from you.

Outside of the lab, I enjoy spending time having dinner and playing games with my Vietnamese friends. Anh chi Cuong – Huong, Thang – Cac, Long – Giang, Duc – Linh, Chinh – Ly, Duc Anh – Han, chi Lien Nguyen, and anh Vuong Le…; thank you all for helping me keep PhD life balance with fun card and board games and making me feel at home with authentic Vietnamese food that we had together.

I would like to thank my family, this journey would not have been possible without their love and support. Thank you to Mom -- me Tinh --, Dad -- bo Dien --, and my dearest sister -- chi

Tra -- for loving me, raising me and supporting me. I cannot start this journey without your inspiration, and cannot finish without your encouragement. I want to become a daughter that you are proud of. This dissertation is dedicated to you. I also thank my sister -- chi Tra --, and her small family -- anh Manh, be Minh (Nem), and be Long (Oi)-- for being an amazing "spy team" on my parents when they got sick but didn't tell me, and for taking good care of them when I am away from home. I thank my family in law - bo Viet, me Bach, chi Van, anh Thang and be Ngan (Gau) - for welcoming me into the family, unconditionally loving me, and encouraging me to follow my dreams.

Most importantly, this acknowledgement would not be completed without devoting my gratitude to my dear husband – Toan. Despite being halfway around the world, and 12 hours time differences between us, you called me every day, you listened to my lab and research stories for hours. You were there for me through all the ups and downs of the graduate school. Your love and optimism gave me inspiration to go to graduate school, strength to persevere through tough times and a burning desire to complete what I had started. I love you more than any words can describe.

Table of Contents

Chapter 1 Introduction ……..……...…..……..1

Chapter 2 In-Situ Electrochemical Stress Measurements
Examining the Oxygen Evolution Reaction in Basic Electrolytes…….....…10

Chapter 3 High Activity Oxygen Evolution Reaction Catalysts
from Additive-Controlled Electrodeposited Ni and NiFe Films….…….....…...46

Chapter 4 Observation of an Inverse Kinetic Isotope Effect in
Oxygen Evolution Electrochemistry….……..……...73

Chapter 5 Nano Porous Copper Films by Additive-Controlled Electrodeposition:
CO_2 Reduction Catalysis……..…..…..…..…...110

Chapter 6 Nano Porous Copper-Silver Alloys by Additive-Controlled Electrodeposition
for High Selectivity of CO_2 Reduction to Ethylene..……..…..…..…..…135

Appendix A Experimental procedures and cell designs…..……..…...151

Chapter 1

Introduction

1.1. Renewable energy and energy conversion

Over the past decades, large quantities of greenhouse gas, especially CO_2, have been emitted and accumulated into the atmosphere, mostly as a result of human activities involving the burning of fossil fuels for electricity, heat and transportation. The elevated level of greenhouse gas in the atmosphere has been contributed to global climate change, including but not limited to global warming, rising sea levels, and more erratic weather patterns. With increasing pressure to reduce greenhouse gas emissions, clean renewable energy sources such as wind and solar are attracting increased attention. The intermittency inherent in these sources means that efficient energy conversion and energy storage systems must be coupled to energy generation.

Several approaches to convert and store excess electricity from renewable energy to other forms of energy, such as potential energy (pumped hydro and compressed air) or chemical energy (batteries and electrolysis), have been proposed. The most common strategies to store energy in the U.S. are pumped hydro and compressed air, however, these methods are only capable of discharge over a few days at most and have very specific geographic requirements. Alternatively, energy storage in an energy-rich molecule is less dependent on geographic location and is more flexible with respect to discharge requirements. H_2 with its high mass specific energy density is considered to be a promising energy storage molecule that releases energy in fuel cells with only water as byproduct. H_2 can be produced via electrochemical splitting of water, which converts excess electricity from renewable sources into H_2 and O_2 and is an attractive way to store energy

in carbon-free H_2. The alternative method to both minimize CO_2 levels and utilize excess electricity from renewable sources is to capture CO_2 and convert it to value-added chemicals or synthetic fuels.

1.2. The electrochemical water splitting and oxygen evolution reaction

Electrochemical water splitting comprises two half reactions, the cathodic hydrogen evolution reaction (HER) at the cathode and the anodic oxygen evolution reaction (OER) at the anode:

Cathode	$2\ H^+ + 2\ e^- \rightarrow H_2$	E_{HER} (vs RHE) = 0 V
Anode	$4\ OH^- \rightarrow 2\ H_2O + 4\ e^- + O_2$ in alkaline	E_{OER} (vs RHE) = 1.23 V
	or $2\ H_2O \rightarrow O_2 + 4\ H^+ + 4\ e^-$ in acid	

The overall voltage $E_{overall}$ required for the water splitting reaction is given by:

$$E_{overall} = E^o + |\eta_{HER}| + \eta_{OER} + \eta_{iR}$$

where E^o is the thermodynamic potential for the water splitting reaction, which is 1.23 V under standard conditions; η_{HER} and η_{OER} are overpotentials for each half-reaction; and η_{iR} is the overpotential due to solution and contact resistances causing ohmic losses in the device. The HER is a fast two proton-two electron reaction occurring at low overpotentials (ranging from 1-10 mA/cm^2 at ~ 50 mV)[1,2] and the overpotential arising from ohmic losses can be minimized by engineering approaches of the cell design. Therefore, the efficiency of the overall reaction scheme is limited primarily by the OER overpotential and catalyst stability at the anode. The OER is a slow four proton-four electron reaction with high overpotential requiring a catalyst to facilitate the reduction. While Ru- and Ir-based catalysts exhibit low OER overpotentials in both acid and

base,[3,4] they are prohibitively expensive. Alternative OER catalysts in base are non-precious metals such as Ni, Co and their alloys, since these material are abundant and cheap, with high corrosion resistance.[5-7] However, Ni and Co catalysts exhibit relatively high overpotentials ranging from *ca.* 300 to 400 mV.[5-8] High stability and activity of nonprecious metal catalysts remain formidable challenges for the OER.

1.3. The CO_2 reduction reaction

There are several methods that can be used to convert CO_2 to various value-added chemicals and fuels including photochemical, biochemical, and electrochemical processes.[9-11] One promising approach is electrochemical conversion of CO_2 value-added chemicals, which has attracted increasing attention for decades due to its potential to facilitate a redox cycle that not only consumes CO_2, but also utilizes excess electricity from renewable sources.[12-14]

In a CO_2 electrolyzer, CO_2 is reduced at the cathode while water is oxidized to form oxygen at the anode. Possible products from the CO_2 reduction include CO, HCOOH, HCHO, CH_3OH, CH4, C2H4, C_2H_5OH and C_3H_7OH. The thermodynamic CO_2 reduction potentials in a pH 7 aqueous solution versus the Normal Hydrogen Electrode (NHE) to these products are as follows:[14,15]

$$CO_2 + 2H^+ + 2e^- \rightarrow CO + H_2O \qquad E^o = -0.52\ V$$

$$CO_2 + 2H^+ + 2e^- \rightarrow HCOOH \qquad E^o = -0.61\ V$$

$$CO_2 + 4H^+ + 4e^- \rightarrow HCHO + H_2O \qquad E^o = -0.48\ V$$

$$CO_2 + 6H^+ + 6e^- \rightarrow CH_3OH + H_2O \qquad E^o = -0.38\ V$$

$$CO_2 + 8H^+ + 8e^- \rightarrow CH_4 + 2H_2O \qquad E^o = -0.24\ V$$

$$2CO_2 + 12H^+ + 12e^- \rightarrow C_2H_4 + 4H_2O \qquad E^o = -0.34\ V$$

$$2CO_2 + 12H^+ + 12e^- \rightarrow C_2H_5OH + 3H_2O \qquad E^o = -0.33\ V$$

$$3CO_2 + 18H^+ + 18e^- \rightarrow C_3H_7OH + 5H_2O \qquad E^o = -0.32\ V$$

Electrocatalysts for the electroreduction of CO_2 are typically metal-based and are classified into four main groups.[14,16] The first group contains metals such as Pt, Ni, Fe and Ti that are not active catalysts for CO_2 reduction due to the strong binding and poisoning of the CO intermediate.[14,17] The second group contains Pb, Hg, Tl, In, Sn, Cd, and Bi which are active primarily for the production of formic acid or formate. The third group containing Ag, Au, Zn, Pd, and Ga primarily produces CO as the reduction product.[14,18] Lastly, the most interesting group contains Cu, which is the only known metal catalyst able to generate a variety of products, particularly hydrocarbons and oxygenates such as methane, ethylene and ethanol.[13,14,16,19-28] For large scale implementation of the CO_2 electrolyzer, high energy efficiencies, reaction rates, product selectivity, and stability must be achieved.

1.4. Additive controlled electrodeposition for nano porous metal film

As mentioned above, in order to commercialize electrochemical energy conversion, a key challenge is developing electrocatalysts with low cost, high activity, high selectivity and high stability. Many studies have focused on tuning reactivity and selectivity by controlling the morphology and composition of the catalysts.[19,21,29-33] Fabrication of nanoparticles, for example, is one well-known approach to increase the number of electrocatalytic active sites. Nanoparticles both increase the activity and decrease the material usage. However, nanoparticles are difficult to fabricate and require a binder such as Nafion when utilized in a real electrolyzer. These ‘glued’ nanoparticles exhibit poor stability, particularly when accompanied by substantial gas and/or

product evolution.[34,35] The presence of binders can also decrease contact sites and conductivity of the electrode leading to diminished reactivity.[36]

Electrodeposition is a conventional deposition technique to prepare smooth and bright polycrystalline metal films that do not require binders.[37] Additives in the electrodeposition bath can affect the roughness and morphology of electrode surface and thus play an important role in determining the catalytic activity of the electrodeposited films. Many additives have been studied, mostly to accelerate metal deposition for different applications such as corrosion protection, decoration, and electrical circuit preparation.[37] In this work, we introduce new electrodeposition class where additives act as inhibitor resulting in the formation of nanoporous metal films for application in electrocatalysis.

The mechanism by which additives, particularly 3,5-diamino-1,2,4-triazole (DAT) in this work, modify the electrodeposition process to yield the rough and porous metal surfaces can be explained by invoking a diffusion-limited aggregation (DLA) process in which the material accretion onto the surface is limited by diffusion and deposition occurs preferentially on protuberances.[38-40] One way to produce porous structures via electrodeposition with DLA is using high voltage (4 V to 20 V) to control diffusion.[41] However, this techniques is limited by stability of the film, especially at high loading. In this work, DAT binds to the substrate surface, reducing the number of nucleation sites for metal deposition, thus initiating roughness. These rough areas experience a high local current density and grow exponentially, while other areas are still DAT-covered and diffusion inhibited. The deposit acquires a nanoporous structure in the presence of DAT even without high voltage.

The additive-controlled electrodeposited film with porous structure exhibits a fractal-like structure, which has a power-law relationship between the number of active or surface sites and

the number of deposited particles. The effect of DAT on the morphology of the deposit was essentially independent of substrate and can be applied to the electrodeposition of various metals such as Ni, Fe, Cu, and their alloys.[42] These features open a wide range of catalytic applications for this type of electrodeposited film where reactivity increases exponentially with material loading.

1.5. References

(1) Trasatti, S. *J. Electroanal. Chem.* **1972**, *39*, 163.

(2) Liu, W.; Hu, E. Y.; Jiang, H.; Xiang, Y. J.; Weng, Z.; Li, M.; Fan, Q.; Yu, X. Q.; Altman, E. I.; Wang, H. L. *Nat. Commun.* **2016**, *7*.

(3) Smith, R. D. L.; Prevot, M. S.; Fagan, R. D.; Zhang, Z. P.; Sedach, P. A.; Siu, M. K. J.; Trudel, S.; Berlinguette, C. P. *Science* **2013**, *340*, 60.

(4) Reier, T.; Oezaslan, M.; Strasser, P. *Acs Catal* **2012**, *2*, 1765.

(5) Lyons, M. E. G.; Brandon, M. P. *J. Electroanal. Chem.* **2010**, *641*, 119.

(6) Hall, D. E. *J. Electrochem. Soc.* **1985**, *132*, C41.

(7) Dau, H.; Limberg, C.; Reier, T.; Risch, M.; Roggan, S.; Strasser, P. *Chemcatchem* **2010**, *2*, 724.

(8) Lyons, M. E. G.; Brandon, M. P. *Int. J. Electrochem. Sci.* **2008**, *3*, 1386.

(9) Whipple, D. T.; Kenis, P. J. A. *Journal of Physical Chemistry Letters* **2010**, *1*, 3451.

(10) Olah, G. A.; Prakash, G. K. S.; Goeppert, A. *Journal of the American Chemical Society* **2011**, *133*, 12881.

(11) Costentin, C.; Robert, M.; Saveant, J.-M. *Chemical Society Reviews* **2013**, *42*, 2423.

(12) Lim, R. J.; Xie, M. S.; Sk, M. A.; Lee, J. M.; Fisher, A.; Wang, X.; Lim, K. H. *Catal Today* **2014**, *233*, 169.

(13) Kortlever, R.; Shen, J.; Schouten, K. J. P.; Calle-Vallejo, F.; Koper, M. T. M. *J Phys Chem Lett* **2015**, *6*, 4073.

(14) Hori, Y. In *Modern Aspects of Electrochemistry*; Vayenas, C. G., White, R. E., Gamboa-Aldeco, M. E., Eds.; Springer New York: New York, NY, 2008, p 89.

(15) Benson, E. E.; Kubiak, C. P.; Sathrum, A. J.; Smieja, J. M. *Chemical Society Reviews* **2009**, *38*, 89.

(16) Noda, H.; Ikeda, S.; Oda, Y.; Imai, K.; Maeda, M.; Ito, K. *Bulletin of the Chemical Society of Japan* **1990**, *63*, 2459.

(17) Hansen, H. A.; Varley, J. B.; Peterson, A. A.; Norskov, J. K. *Journal of Physical Chemistry Letters* **2013**, *4*, 388.

(18) Noda, H.; Ikeda, S.; Yamamoto, A.; Einaga, H.; Ito, K. *Bulletin of the Chemical Society of Japan* **1995**, *68*, 1889.

(19) Tang, W.; Peterson, A. A.; Varela, A. S.; Jovanov, Z. P.; Bech, L.; Durand, W. J.; Dahl, S.; Norskov, J. K.; Chorkendorff, I. *Phys Chem Chem Phys* **2012**, *14*, 76.

(20) Kas, R.; Hummadi, K. K.; Kortlever, R.; de Wit, P.; Milbrat, A.; Luiten-Olieman, M. W. J.; Benes, N. E.; Koper, M. T. M.; Mul, G. *Nat Commun* **2016**, *7*.

(21) Ma, S. C.; Sadakiyo, M.; Luo, R.; Heima, M.; Yamauchi, M.; Kenis, P. J. A. *J Power Sources* **2016**, *301*, 219.

(22) Kas, R.; Kortlever, R.; Milbrat, A.; Koper, M. T. M.; Mul, G.; Baltrusaitis, J. *Phys Chem Chem Phys* **2014**, *16*, 12194.

(23) Li, C. W.; Kanan, M. W. *J Am Chem Soc* **2012**, *134*, 7231.

(24) Manthiram, K.; Beberwyck, B. J.; Aivisatos, A. P. *J Am Chem Soc* **2014**, *136*, 13319.

(25) Mistry, H.; Varela, A. S.; Bonifacio, C. S.; Zegkinoglou, I.; Sinev, I.; Choi, Y. W.; Kisslinger, K.; Stach, E. A.; Yang, J. C.; Strasser, P.; Cuenya, B. R. *Nat Commun* **2016**, *7*.

(26) Ma, M.; Djanashvili, K.; Smith, W. A. *Angew Chem Int Edit* **2016**, *55*, 6679.

(27) Christophe, J.; Doneux, T.; Buess-Herman, C. *Electrocatalysis* **2012**, *3*, 139.

(28) Ishimaru, S.; Shiratsuchi, R.; Nogami, G. *Journal of the Electrochemical Society* **2000**, *147*, 1864.

(29) Sen, S.; Liu, D.; Palmore, G. T. R. *Acs Catal* **2014**, *4*, 3091.

(30) Zhu, S. Q.; Shao, M. H. *J Solid State Electr* **2016**, *20*, 861.

(31) Feng, X. F.; Jiang, K. L.; Fan, S. S.; Kanan, M. W. *Acs Central Sci* **2016**, *2*, 169.

(32) Guo, Y. G.; Hu, J. S.; Wan, L. J. *Adv Mater* **2008**, *20*, 4384.

(33) Mistry, H.; Varela, A. S.; Kuhl, S.; Strasser, P.; Cuenya, B. R. *Nat Rev Mater* **2016**, *1*.

(34) Ji, J. Y.; Zhang, L. L.; Ji, H. X.; Li, Y.; Zhao, X.; Bai, X.; Fan, X. B.; Zhang, F. B.; Ruoff, R. S. *Acs Nano* **2013**, *7*, 6237.

(35) Garg, G.; Basu, S. *Electrochim Acta* **2015**, *177*, 359.

(36) Lu, X. Y.; Zhao, C. A. *Nat. Commun.* **2015**, *6*, 6616.

(37) Schlesinger, M.; Paunovic, M. *Modern electroplating*; 5th ed.; Wiley: Hoboken, NJ, 2010.

(38) Witten, T. A.; Sander, L. M. *Phys. Rev. Lett.* **1981**, *47*, 1400.

(39) Godorr, S. A.; Young, B. D.; Bryson, A. W. *Chem. Eng. Commun.* **1992**, *117*, 307.

(40) Russ, J. C. *Fractal surfaces*; Plenum Press New York 1994.

(41) Trigueros, P. P.; Claret, J.; Mas, F.; Sagues, F. *J. Electroanal. Chem.* **1991**, *312*, 219.

(42) Hoang, T. T. H.; Gewirth, A. A. *Acs Catal* **2016**, *6*, 1159.

Chapter 2

In-Situ Electrochemical Stress Measurements Examining the Oxygen Evolution Reaction in Basic Electrolytes

2.1. Introduction

The electrochemical splitting of water using electricity from renewable sources offers an attractive way to provide a carbon free source of hydrogen.[1-3] Electrochemical water splitting comprises two half reactions: the anodic oxygen evolution reaction (OER, $4OH^- \rightarrow 2H_2O + 4e^- + O_2$ in alkaline or $2\ H_2O \rightarrow O_2 + 4\ H^+ + 4\ e^-$ in acid), and the cathodic hydrogen evolution reaction (HER, $2\ H^+ + 2\ e^- \rightarrow H_2$). The efficiency of the overall reaction is limited primarily by the overpotential of the OER and stability of electrode material.[4]

In acid electrolyte, Ru and Ir based materials are among the best anodes with low overpotentials.[5] However, the high cost and poor long-term stability of these precious metal catalysts are impediments to their widespread application. In alkaline electrolyte, non-precious metals such as Ni, Co, and their alloys are used as the electrocatalysts for OER, since these materials are abundant and relatively cheap, with high corrosion resistance in alkaline solution.[6-8] However, overpotentials for the OER using Ni and Co range from *ca.* 300 to 400 mV relative to the thermodynamic value of 1.23 V *vs*. RHE.[4,6-8]

An important challenge for the OER is to discover and develop catalysts that can reduce the overpotential to at least the thermoneutral potential of 1.48 V *vs*. RHE.[2,9] Moreover, the catalyst must be cheap and stable at practical current densities (at least 10 mA/cm^2). Real-world thermodynamic efficiencies for water splitting are only *ca.* 75% with currently available Ni-based catalysts.[2] However, catalyst design to eliminate the high OER overpotential is still limited because insight into the OER mechanism is lacking.[8]

Mechanistic studies of the OER focus on the electrode materials, which are now known to be surface oxides and oxyhydroxides formed on the metal prior to the OER.[10] OER mechanism and activity depends on the composition and oxidation state of the oxide layer. Density functional theory (DFT) studies predicted that the binding energy of surface oxygen species such as *O, *OH, *OOH is the activity controlling parameter.[3,8,10] Additionally, compositionally identical oxides may give rise to disparate electrochemical activities, with strong dependencies found for the thickness, bond distance, morphology and interaction with anions of the oxide layer.[6,11] In order to understand the OER mechanism on oxidized metals, it is important to interrogate the nature of the oxide layers formed due to phase changes and oxidation processes prior to and during the OER.

Extensive voltammetric studies of the OER on metal and oxide electrodes have been reported. [5,12,13] Film oxidation state and compositional and structural changes upon redox cycling have been studied using a variety of techniques, including Raman,[14-17] XPS,[18-21] XRD,[22,23] and XAS.[24-26] Morphological examination of oxidized metals has been accomplished by using SEM and TEM,[22,27] STM,[28] ellipsometry,[29,30] and AFM[31,32] techniques. Evolution of the oxide lattice during redox processes has been studied EQCM.[33-36] A direct *in situ* method to interrogate the oxide film during potential cycling, along with its evolution over time and multiple

electrochemical cycles would help provide a more comprehensive description of the oxide before and during the OER process.

In situ electrochemical surface stress measurements are a useful technique to investigate surface interactions and electrode evolution during electrochemical processes.[37,38,39-41] The technique has also been applied to study metal electrode oxidation and reduction including the stress-potential behavior of Pt and Au electrodes during oxygen reduction,[42] the changes in surface stress of Pt electrodes in acidic and alkaline solutions,[43] and the surface stress-charge response of a Pt electrode in the double layer region,[44] and during hydrogen adsorption/desorption and surface oxidation/reduction.[40]

In this section, we use *in situ* electrochemical stress measurements to interrogate oxide evolution before and during the OER in several common electrodes, including those exhibiting high activity for the OER such as Ir, Ni, and Co, along with those exhibiting much less activity, such as Au and Pt. The stress measurements report on the state of the electrode during the OER, along with electrode stability.

2.2. Experimental section

Cantilever fabrication: Au cantilevers for stress measurements were fabricated from glass microscope cover-slips (Gold Seal No.1, 150 μm thick) modified on one side by electron beam deposition of 20 nm Ti followed by 100 nm Au. Pt cantilevers were fabricated from glass microscope cover-slips modified on one side by DC magnetron sputter deposition of 20 nm Ti followed by 200 nm Pt. The Ni, Co, and Ir cantilevers were prepared by electrodeposition of 300 nm of the appropriate metal onto Au cantilevers. The Ni, Co, and Ir cantilevers were prepared by

electrodeposition of 300 nm of the appropriate metal onto Au cantilevers. The bath compositions were as follows: (a) Ni plating bath: 199 g/L $NiSO_4 \cdot 6H_2O$, 25 g/L H_3BO_3, and 1 g/L Saccharin;[45] (b) Co plating bath: 213 g/L $CoSO_4 \cdot 7H_2O$, 25 g/L H_3BO_3;[45] (c) Ir plating bath: 0.5 M H_2SO_4, and 1 mM Na_2IrCl_6.[46] Ni and Co were deposited galvanostatically at current density of 4.33 mA/cm^2. Ir was deposited potentiostatically at constant potential of 0.2 V *vs.* Ag/AgCl. Cantilever with dimensions approximately 30 × 4 mm were then cut from the modified cover-slips. All cantilevers were rinsed and stored in Milli-Q water (>18 MΩ cm) until used. The Au and Pt cantilever were annealed with a H_2 flame prior to use.[47]

In-Situ electrochemical stress measurements: In situ stress data was collected by using an electrochemical cell and optical stress measurement setup described previously.[47,48] Surface stress was measured using the bending-beam method and the cantilever curvature was calculated using Stoney's equation[49]. Cyclic voltammetry (CV) was conducted using the glass/metal cantilever as the working electrode, a Pt mesh counter electrode, and an Ag/AgCl reference electrode. Potentials are reported with respect to RHE. CV was measured at room temperature in Ar saturated 1 M NaOH (>99%, Sigma) at 10 mV/s. Both the surface stress changes and the electrochemical data was recorded using a home-built program written using LabVIEW (National Instruments). The refractive index of 1 M NaOH was measured on a Refracto 30GS (Mettler Toledo) and were found to be 1.3439±0.0001.

Nanoindentation and Young's modulus calculation: $Ni(OH)_2$ and $Co(OH)_2$ samples for nanoindentation were prepared on microscope glass slide by using the following steps. First, a glass microscope slide was modified on one side by electron beam deposition of 20 nm Ti followed by 150 nm Au. 300 nm Ni or Co was electrodeposited on the Au surface to provide better adhesion for the $Ni(OH)_2$ or $Co(OH)_2$ overlayer. This step also helps to imitate the effect of the metal

underlayer on the hydroxide modulus that may be present in the stress measurement samples. Ca. 1 μm $Ni(OH)_2$ was electrodeposited on Ni at 0.9 V vs Ag/AgCl in 0.01M of $Ni(NO_3)_2$. Ca. 1 μm $Co(OH)_2$ was electrodeposited on Co at 1.0 V vs Ag/AgCl in 0.01M of $Co(NO_3)_2$. After preparation, samples were rinsed with Milli-Q water (>18 MΩ cm^{-1}) and stored in 1M NaOH until the measurement. Samples were maintained wet during the measurement. Dry samples were found to flake and were unstable.

A Hysitron TI 950 TriboIndenter was used to perform nanoindentation tests to calculate the Young's modulus of $Ni(OH)_2$ and $Co(OH)_2$. A three-sided pyramidal diamond (Berkovich) tip was used for the indentation. The applied peak load was 3000 - 10000 μN. The nanoindenter monitors and records the load and displacement of the indenter during indentation. Young's modulus is calculated from the load-displacement curves by the following equations:

Unloading stiffness (*S*) was obtained from the slope of unloading part in load (*P*)-displacement (*h*) curve by the equation:

$$S = \frac{dP}{dh}$$

Reduced Young's modulus can be calculated from stiffness (*S*) by the equation:

$$E_r = \frac{S}{2\beta}\sqrt{\frac{\pi}{A}}$$

Where β is a constant that depends on the geometry of the indenter, β=1.034 for a Berkovich indenter. A is the projected contact area of the indenter. [50]

E_r is the reduced Young's modulus, which accounts the fact that elastic deformation occurs in both the sample and the indenter. E_r is related to Young's modulus (E) of sample by the equation:

$$\frac{1}{E_r} = \frac{1-\vartheta^2}{E} + \frac{1-\vartheta_i^2}{E_i}$$

Where ϑ is Poisson's ratio of the sample and $\vartheta_i = 0.07$ is Poisson's ratio of the tip. For diamond tip, Young's modulus E_i =1141 GPa.

Oxidation charge and oxide thickness calculation: Oxidation charge (Q) of electrode surface is equal to integrated oxidation current divided by scan rate (10mV/s). Thickness (s) of oxyhydroxide films of Ni and Co electrode are calculated by the following equation:

$$s = \frac{Q.M}{n.F.d.A}$$

Where Q is oxidation charge (C); M is molecular weight of the oxyhydroxide (g/mol), n is the number of electrons transfer, F is Faraday constant (96500 C/mol), A is electrode area (cm^2), and d is density of the oxide product ($g.cm^3$) (density of β-NiOOH is 4.68 g/cm^3, and density of CoOOH is 3.60 g/cm^3).

2.3. Results

2.3.1. OER and stress from Ni electrodes

Figure 2.1a shows CV obtained from a Ni(poly) electrode in 1 M NaOH, cycled between 0.55 V and 1.60 V *vs.* RHE. After immersion in the alkaline solution, the Ni metal is spontaneously oxidized to $Ni(OH)_2$.[23,51] $Ni(OH)_2$ is oxidized to form NiOOH at 1.4 V on the anodic sweep. OER occurs at *ca.* 1.5 V. Reduction of the NiOOH film to $Ni(OH)_2$ occurs at 1.3 V on the cathodic sweep. Two features are observed in the reduction, which are associated with γ- and β-NiOOH, from positive to negative potentials, respectively. This voltammetry is identical with that reported previously.[1,52,53]

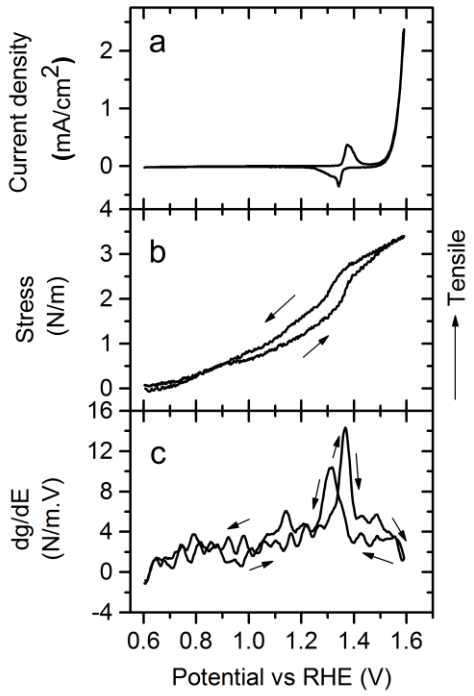

Figure 2.1. (a) CV of Ni(poly) in 1 M NaOH at 10 mV/s (b) corresponding in situ stress data of Ni and (c) first derivative of surface stress change with respect to the surface potential.

Figure 2.1b shows the corresponding surface stress changes occurring during the voltammetry. The stress becomes tensile as the potential is swept to more anodic values. The increasing tensile stress between 0.6 V and 1.3 V is associated with changes in the $Ni(OH)_2$ film. At 0.6 V, α-$Ni(OH)_2$ exhibits a distorted rhombic structure with unit cell parameters a_0 = 5.42 Å and c_0 = 8.05 Å.[23,54] At higher potential the α-$Ni(OH)_2$ converts partially to hexagonal β-$Ni(OH)_2$ [55,56] with a_0 = 3.13 Å and c_0 = 4.59 Å.[23,54] The conversion to the denser β-$Ni(OH)_2$ is the origin of the tensile stress observed.

Figure 2.1b shows that the rate of increase in the tensile stress accelerates from 1.3 V to 1.5 V, when $Ni(OH)_2$ is oxidized to form NiOOH. Both γ and β - NiOOH has a_0 = 2.82 Å, smaller than that found in the $Ni(OH)_2$ form and the conversion between the two is the origin of the tensile

stress.[32,54] In the region where the OER occurs (above 1.5 V) the tensile stress continues to increase, albeit at rates slower than found in the previous region. The β–NiOOH may convert to γ–NiOOH in this region,[54] but they have the same $a_{0=}$ 2.82 Å, thus no change in stress due to this phenomenon is observed. As the potential is cycled back to 0.55 V the film converts back to $Ni(OH)_2$ and the stress returns to its original value. The lack of hysteresis in the stress at the and of each cycle means that the film has fully converted back to its original $Ni(OH)_2$ phases consistent with prior work.[28,29,31,35].

The 1st derivative of the stress with respect to the potential (Figure 2.1c) mimics the voltammetry shown in Figure 21a. The largest change in slope, between 1.3 and 1.5 V on the anodic sweep, and 1.4 V and 1.2 V on the cathodic sweep are associated with the reversible β-$Ni(OH)_2$ conversion to NiOOH.

2.3.2. OER and stress from Co electrodes

Figure 2.2a shows CV obtained from a Co(poly) electrode in 1 M NaOH, cycled between 0.3 V and 1.60 V *vs.* RHE. After immersion in the alkaline solution, the Co metal is oxidized to form $Co(OH)_2$ film on the electrode surface, albeit at a rate slower than that found for Ni.[18,57] The CV shows three anodic features. The large peak at 0.87 V is associated with the oxidation of $Co(OH)_2$ to CoOOH.[13,58] The broad oxidation region from 1.0 V to 1.3 V with a small peak at 1.11 V is associated with deeper oxidation of $Co(OH)_2$ and transformations between different Co(III) oxides.[58,59] The peak at 1.43 V is attributed to the oxidation of Co(III)-based oxides to Co(IV) species.[58,60,61] OER occurs at *ca.* 1.5 V. On the cathodic sweep, three reduction peaks observed at 1.42 V, 1.10 V and *ca.* 0.7 V are associated with reduction of Co(IV) species to Co(III),

transformations between different Co(III) oxides, and reduction of CoOOH to $Co(OH)_2$, respectively. This CV is similar to those reported.[6,13,24]

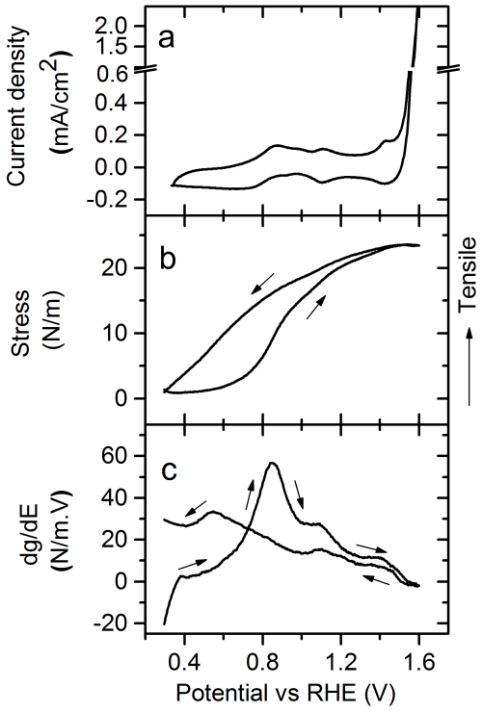

Figure 2.2. (a) CV of Co(poly) in 1M NaOH at 10 mV/s (b) corresponding *in situ* stress data of Co and (c) first derivative of surface stress change with respect to the surface potential.

The first cycle of Co in base[58] shows a peak at 1.1 V which evolves over time to yield the voltammetry shown in Figure 2.2a. EXAFS[24] showed this wave was associated with changes in Co-Co distances which were different on the first cycle relative to the second. Consequently, the voltammetry and stress reported here is for the fourth cycle. Figure 2.2b shows the corresponding surface stress changes. In general, the stress becomes tensile as the potential is swept to more anodic values. The increasing tensile stress between 0.6 V and 1.0 V is associated with the oxidation of $Co(OH)_2$ to CoOOH. $Co(OH)_2$ exhibits a Co-O distance of 2.09 Å and a Co-Co distance of 3.17 Å. CoOOH, on the other hand, exhibits a Co-O distance of 1.92 Å and a Co-Co distance of 2.85 Å, which are smaller than that found in $Co(OH)_2$.[21,22,24] Figure 2.2b also shows

that the rate of tensile stress change decreases (i.e. exhibits smaller slope) between 1.0 V and 1.3 V, where deeper oxidation of $Co(OH)_2$ to COOH and transformations between different Co(III) oxides take place. CoOOH could change to Co_2O_3, which has Co-O distance of 1.90 Å, and Co-Co of 2.64 Å,[62] smaller than that found in the CoOOH form. The conversion between the two is the origin of the tensile stress. From 1.3 V to 1.5 V, where Co(III)-based oxides (mostly CoOOH) are oxidized to Co(IV) species, the tensile stress continues to increase, but with a lower rate. There are suggestions that the Co(IV) species present in this potential region.[13,58] The loss of hydrogen from CoOOH to form CoO_2 could be the origin of the tensile stress. The three different regions are clearly seen in the derivative in Fig. 2c.

In OER region (*ca.* 1.5 V), the stress is potential independent, suggesting that further film transformation does not occur. As cycling back to 0.3 V, the tensile strain is removed, the film converts back to $Co(OH)_2$ and the stress returns to its original value. The lack of hysteresis in the stress means that the film has fully converted back to its original $Co(OH)_2$ phases.[24] We note, however, that the path taken by the stress in the anodic sweep differs from that taken in the cathodic sweep, in contrast to the Ni case. The origin of this behavior is likely related to the hysteresis in the cathodic and anodic waves (at *ca.* 0.8V) associated with $Co(OH)_2$ oxidation.

Figure 2.2c reports the first derivative of the stress with respect to the applied potential. The three oxidation features in the CV appear as steps in the derivative of the stress. The largest change in slope, between 0.6 V and 1 V, is associated with the reversible $Co(OH)_2$ conversion to CoOOH. The second change in slope, between 1 V and 1.3 V, is associated with transformations between different Co(III) oxides. And the last change, between 1.3 V and 1.5 V, is associated with the oxidation to Co(IV). [58,60]

2.3.3. OER and stress from Ir electrodes

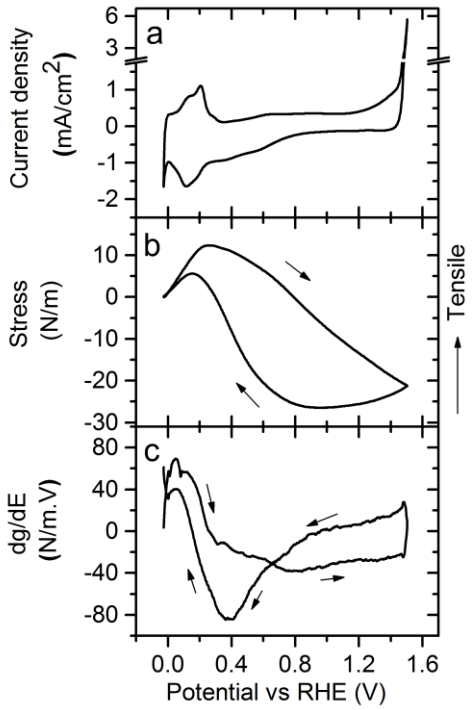

Figure 2.3. (a) CV of Ir(poly) in 1M NaOH at 10 mV/s (b) corresponding *in situ* stress data of Ir and (c) first derivative of surface stress change with respect to the surface potential.

Figure 2.3a shows CV obtained from a Ir(poly) electrode immersed in 1 M NaOH and cycled between -0.1 V and 1.55 V *vs.* RHE. In the anodic sweep, hydrogen desorption from the Ir surface occurs between -0.1 V and 0.3 V. The double layer region starts at 0.3 V. Above 0.4 V, the voltammetry shows an ill-defined wave, which is associated oxidation of Ir. From 0.4 V to 0.7 V, oxygen is chemisorbed on Ir to form $Ir(OH)_3$.[12,34] From 0.7 V to 1.2 V, oxidation of Ir principally and $Ir(OH)_3$ secondarily to Ir(IV) takes place.[34] Above 1.2 V, further oxidation to Ir(IV) and Ir(V) along with nascent oxygen evolution causes a rise in current density.[12] OER occurs at 1.46 V. In the cathodic sweep, the CV also shows a series of ill-defined waves associated with Ir oxide reduction. In particular, reductions are observed for Ir(V) to Ir(IV) (ca. 1.4 V) , for Ir(IV) to Ir(III) (*ca.* 0.9 V), and for Ir(III) to Ir metal (between 0.8 V and 0.2 V). From 0.2 V to -0.05 V, the

voltammetry exhibits a large peak associated with hydrogen adsorption on the Ir surface, during which continued reduction of Ir(III) to Ir also occurs. Hydrogen evolution occurs at -0.05 V. This voltammetry is similar to that reported previously.[12,34,63,64] We note that Ir voltammetry is a sensitive to cycle history, with pronounced peaks associated with Ir(IV) formation found only after extended high rate cycling in dilute solution.[64,65]

Figure 2.3b shows the corresponding surface stress changes occurring during the voltammetry. In contrast to the surface stress exhibited by both Co and Ni, the stress is generally compressive during the anodic sweep. The Ir surface exhibits four activity regions. First, the stress is tensile as the potential is swept from -0.1 V to 0.3 V. This tensile stress is assigned to surface contraction resulting from hydrogen removal from Ir surface.[12] At *ca.* 0.3 V, the stress abruptly becomes compressive because of Ir oxidation. While the voltammetry in the Co and Ni cases is consistent with a well-defined change to different metal oxidation states (corresponding to dehydrogenation of the initially hydrous Ni or Co material), the changes here occur as a result of oxidation of the zero valent Ir metal. The compressive stress observed between 0.3 V and 0.8 V is associated with the surface expansion during oxidation of Ir metal to $Ir(OH)_3$. Between 0.8 V and 1.2 V, the stress remains compressive, which is associated with the oxidation of Ir metal to Ir(IV) (the species could be $IrO(OH)_2$ or IrO_2 [19]). Above 1.2 V, the compressive stress continues to increase, albeit at rates slower than found in the previous region, associated with continued oxidation of the Ir film. The continuous increasing in compressive stress due to the continuous oxidation of Ir metal to Ir oxides is consistent with the continuous increase in Ir electrode mass studied by EQCM previously.[34]

When the potential is cycled back to negative values, the stress returns back to its original value, but not via the same path as during the anodic sweep. Initially, the stress is compressive as

the potential is swept from 1.55 V to 0.8 V. This compressive stress could be explained by the addition of hydrogen to $IrO(OH)_2$ and/or IrO_2 to form $Ir(OH)_3$. At 0.8 V on the cathodic sweep, the stress turns from compressive to tensile, which is associated with the removal of oxygen when $Ir(OH)_3$ is reduced to Ir metal. The stress remains tensile with a constant slope until *ca.* 0.2 V when Ir(III) reduction and hydrogen chemisorption occur simultaneously. The Ir(III) reduction (causing surface contraction) competes with the hydrogen adsorptionon Ir surface (causing surface expansion). Thus, the rate of tensile stress starts decreasing at 0.2 V and the stress turns compressive at 0.1 V - the peak of hydrogen adsorption. After each cycle, the stress returns to almost the same value, which means that the film has mostly been converted back to Ir metal. A small drift after each cycle was observed at -0.1 V and could be due to limited dissolution of Ir oxides which was reported previously.[5,33,34]

The first derivative of the stress with respect to the applied potential (Fig. 3c) mimics the voltammetry shown in Fig. 3a.

2.3.4. OER and stress from Au electrodes

As the potential is cycled back to 0.3 V, the film is reduced and Au metal is recovered. The stress becomes more tensile as the potential is swept to more cathodic values, but in contrast to the Ni, Co, and Ir cases, it does not return to the original value. Initially, from 1.6 V to 1.2 V, the stress is slightly tensile which may be a consequence of place exchange - known to occur in this region.[66] However, the lack of current in the voltammetry excludes Faradaic processes. Between 1.2 V and 1.0 V, Au(III) is reduced to AuOH and the tensile stress increase accelerates. The removal of oxygen and/or hydroxide from the Au oxide layer is the origin of this tensile stress. Between 1.0 V and 0.3 V, reduction of AuOH to Au occurs. The removal of surface hydroxide should yield

tensile stress on the electrode. Interestingly, this tensile stress is not observed; instead, the stress becomes slightly compressive. This compressive stress could be the result of Au oxide dissolution during Au hydroxide reduction, follow Au oxidation peak.[67,68] The dissolution causes a rougher Au surface. Stronger absorption of ions on this roughened Au relative to the smoother surface prior to oxidation would be the origin of compressive stress at 1.0 V to 0.3 V.

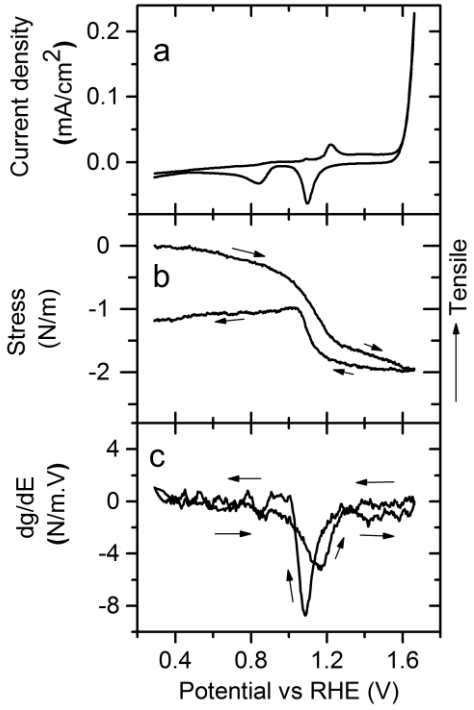

Figure 2.4. (a) CV of Au(poly) in 1 M NaOH at 10 mV/s (b) corresponding in situ stress data of Au and (c) first derivative of surface stress change with respect to the surface potential.

Figure 2.4c reports the first derivative of the stress with respect to the applied potential. The largest change in slope, between 1.0 and 1.2 V on the anodic and cathodic sweep is associated with the reversible AuOH conversion to $Au(OH)_3$ and mimics the voltammetry shown in Figure 2.4a.

2.3.5. OER and stress from Pt electrodes

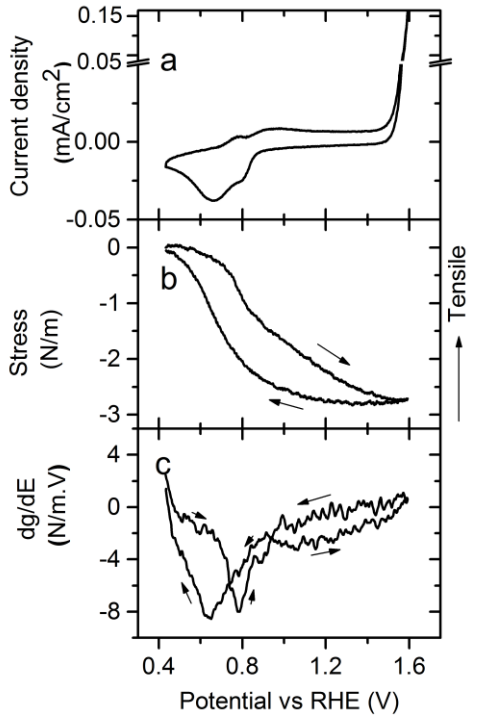

Figure 2.5. (a) CV of Pt(poly) in 1M NaOH at 10 mV/s (b) corresponding *in situ* stress data of Pt and (c) first derivative of surface stress change with respect to the surface potential.

Figure 2.5a shows CV obtained from a Pt(poly) electrode 1 M NaOH and cycled between 0.4 V and 1.6 V *vs.* RHE. The CV shows OH^- chemisorption on Pt at *ca.* 0.7 V. The main oxidation peak occurs at *ca.* 0.9 V. This peak is followed by a current plateau which extends up to OER at *ca.* 1.6 V. The cathodic peak at 0.80 V and 0.66 V is associated with reduction of the Pt oxides film to Pt, and reduction of the oxygen generated during the OER is reduced The voltammetry is similar to that reported previously.[20,69,70]

Figure 2.5b shows the corresponding surface stress changes of Pt occurring during the voltammetry. Generally, the stress becomes compressive as the potential is swept to more anodic values, which is associated with Pt oxidation. The adsorption of OH- in the prepeak region and the

addition of oxygen and hydrogen into the Pt adlayer is the origin of this compressive stress. As the potential is cycled back to 0.4 V, the compressive strain is removed, the film converts back to Pt and the stress returns to its original value. The lack of hysteresis in the stress means that the film has fully converted back to its original Pt.

Figure 2.5c reports the first derivative of the stress with respect to the applied potential, which mimics the voltammetry (Figure 2.5a). Two derivative peaks at *ca.* 0.8 V (anodic) and *ca.* 0.6 V (cathodic) are associated with the reversible Pt redox.

2.3.6. Evolution of stress after cycling of Ir

The stress observed for Ni and Co was generally invariant with cycle number. However, Pt, Au, and Ir exhibited evolution of the stress with cycling. Figure 2.6a shows CV obtained from a Ir(poly) electrode in 1 M NaOH and cycled between 0.3 V (which is more anodic than the Ir hydrogen adsorption region) and 1.60 V *vs.* RHE (where OER occurs). During the 10 cycles (Figure 2.6a), the OER current drops by 40% and the oxide reduction peak intensity at 0.4 V loses 60%. The change in these peaks with cycle number has previously been associated with surface deactivation by strong anodization in the OER region resulting in surface corrosion and loss of material.[64]

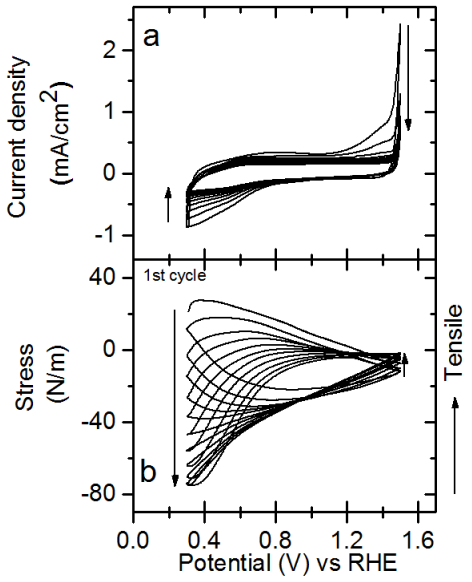

Figure 2.6. a) CV of Ir in 1M NaOH at 10 mV/s from 0.3 V to 1.5 V, (b) corresponding *in situ* stress data of Ir.

The charge passed reducing the oxide film (Q_c) is only 68% of the oxidation charge (Q_a) in the first cycle, and gradually increases to 97% during the 10th cycle. A similar effect has been reported by Burke *et al*[64] where the ratio Q_c/Q_a is approximately 1:2 and decreases in subsequent cycling to values approaching 1:1. The ratio of $Q_c/Q_a < 1$ suggests that some oxides are retained on the surface, even at negative potentials. The irreversibility in oxidation and reduction of the Ir is associated with slow migration of oxygen and hydroxide through a thick oxide film. On the other hand, the ratio Q_c/Q_a approaching 1:1 after cycling suggests that redox of the Ir oxide film (after cycling Ir) is more reversible than Iridium. This effect is associated with migration of hydrogen into and out of the oxide film, which is more likely to be faster.

Figure 2.6b shows the corresponding surface stress changes of Ir occurring during the voltammetry. During the first cycle, the stress is similar to that reported above during the OER – the stress becomes compressive with anodic potential sweep. With additional cycling, the stress at

1.5 V slightly becomes more tensile, which could be explained by surface corrosion in the OER region.[64] The stress value at more cathodic potentials becomes more compressive in subsequent cycles, which could be explained by the accumulation of Ir oxides on the electrode surface. $Ir(OH)_3$ is not fully converted back to Ir at 0.3 V.[5,34,71]

After 10 cycles, the potential-dependent stress observed for the Ir electrode has evolved to exhibit a slope opposite to its initial value. The tensile stress on the anodic sweep, which is observed clearly after the 10^{th} cycle, is associated with oxidation of $Ir(OH)_3$ – now present at cathodic potentials on the electrode surface – to $IrO(OH)_2$ and/or IrO_2. EXAFS measurements on $Ir(OH)_3$ films showed that the Ir-O and Ir-Ir distances decreased about 0.1 Å when the surface is oxidized from 0.4 V to 1.5 V[25,26] As with the Co and Ni cases, the oxidation of $Ir(OH)_3$ to denser oxides is the origin of the tensile stress observed. As the potential is cycled back to 0.3 V, the tensile strain is removed, the film converts back to $Ir(OH)_3$ leading to compressive stress through the cathodic sweep.

This stress evolution suggests that redox cycling of the Ir electrode between 0.6 V and 0.5 V, respectively, is irreversible. During the first cycle, the stress features are associated with oxidation of Ir(0). After 10 cycles, the stress features are associated with oxidation of a $Ir(OH)_3$ film. The rate of change in the stress after each cycle becomes smaller and smaller. Since the anodic and cathodic stress sweeps of $Ir(OH)_3$ film follows the same path, we suggest that electrochemical reaction of $Ir(OH)_3$ film is reversible.[5,72]

2.3.7. Evolution of stress after cycling of Au electrode

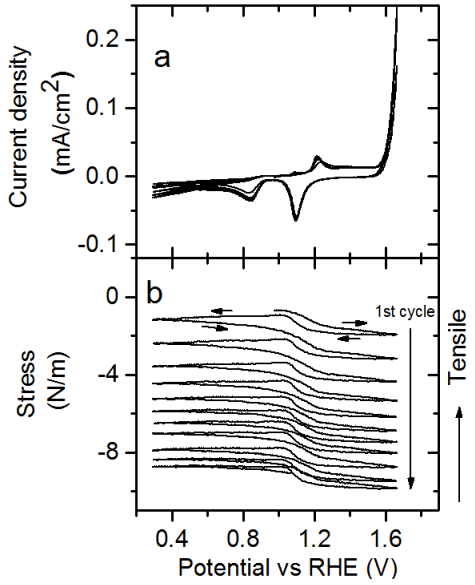

Figure 2.7. a) CV of Au(poly) in 1M NaOH at 10 mV/s from 0.3 V to 1.5 V (b) *in situ* stress data of Au in 1M NaOH.

Figure 2.7a shows CV obtained from an Au(poly) electrode in 1 M NaOH and cycled between 0.3V and 1.65 V *vs.* RHE after 11 full cycles. Figure 2.7b shows the corresponding surface stress changes of Au occurring during the voltammetry. The shape and magnitude of stress of single cycle is similar to that shown in Figure 2.4. The stress becomes more compressive in subsequent cycles. Two possibilities could contribute to this compressive evolution. The first cause is place exchange of oxygen atoms from surface to sub-surface positions.[67,73] Those sub-surface oxygen atoms cannot be removed when potential is swept back to more negative values. With increased cycling there would then be increased oxygen diffusion into the bulk of the Au electrode, leading to more compressive stress. The second possible cause is dissolution of Au oxides at high potentials following surface oxidation.[67,68] In this case increased cycling leads to a rougher surface which then leads to increased anion absorption which in turn leads to development of more

compressive stress. Increasing roughness of the Au surface was estimated by analyzing the evolution of oxide stripping in the Au voltammetry. We found that the cathodic peak feature at 1.1 V increases by 10% of its initial current density.

2.3.8. Evolution of stress after cycling Pt electrodes

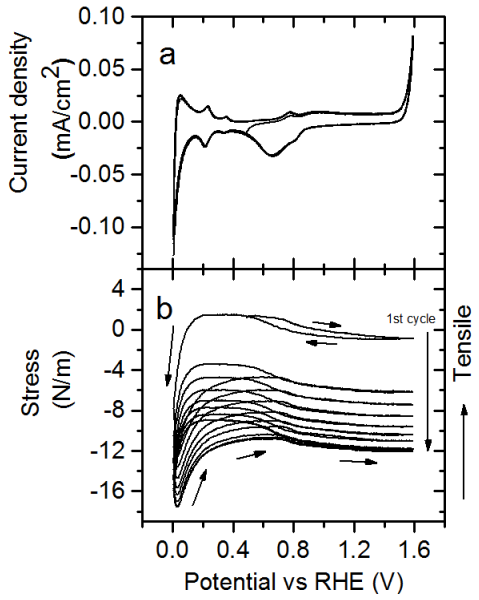

Figure 2.8. a) CV of Pt(poly) in 1 M NaOH at 10 mV/s from 0.3 V to 1.5 V (b) *in situ* stress data of Pt in 1M NaOH.

Figure 2.8a shows CV obtained from a Pt(poly) electrode in 1 M NaOH and cycled between 0.3 V and 1.65 V *vs.* RHE for 10 full cycles. The anodic sweep shows hydrogen desorption between 0 V and 0.4 V, the double layer region between 0.4 V and 0.6 V, OH^- chemisorption at *ca.* 0.7 V, Pt oxidation at *ca.* 0.9 V, and OER at above 1.6 V. The cathodic sweep shows oxide stripping merging with oxygen reduction between 0.9 to 0.5 V, hydrogen absorption associated features below 0.3 V, and hydrogen evolution at 0 V.

Figure 2.8b shows the corresponding surface stress changes from Pt occurring during the voltammetry. The 1st cycle starts at *ca.* 0.4 V in the double layer region, and scans to the OER region. The stress during the 1st cycle is similar to that shown in Figure 2.5. The stress exhibits a compressive change during Pt oxidation, and returns to more tensile values during the reduction of Pt oxides, as explained in Section 3.5. In the double layer region, the stress changes little. In the potential range between 0.2 V to 0.0 V during the cathodic sweep, the stress abruptly becomes more compressive. This compressive stress is associated with adsorption of upd H^+ and H_2 evolution, in which newly generated H_2 species on the Pt surface repel each other. When potential is cycled back to more positive potentials, the stress abruptly becomes tensile again. This tensile stress is assigned to surface contraction resulting from H_2 release.

Interestingly, the stress after one cycle does not come back to its original value but rather becomes more compressive in subsequent cycles. Two possible reasons to explain this compressive evolution are place-exchanged oxygen[74-76], and/or irreversibly adsorbed hydrogen on the Pt surface.[77] We note that if the potential reversal occurs more positive of the hydrogen region, then the stress is reversible upon cycling as shown in Figure 2.5. Therefore, the compressive evolution of stress shown in Figure 2.8b is not associated with Pt surface oxidation and is likely not explained by the place exchange mechanism. On the other hand, Figure 2.8b shows that the compressive stress resulting from H_2 adsorption does not return even when cycling the potential up to OER. This strongly suggests that hydrogen adsorption/desorption occurring at potentials more negative than the double layer region (< 0.4 V) is irreversible, and some H_2 remains on Pt surface even at high positive potential. Hence, residual H_2 – possibly subsurface – is the main origin of compressive evolution of Pt after cycling. The compressive difference in stress of the 1st and the 2nd cycle is largely due to a large number of available Pt sites for H_2 absorption. The difference

between 2 consecutive cycles becomes smaller as the number of cycle increases and becomes negligible after 8 cycles. The stress of cycle 8 - 10 are identical (Figure 2.8b), suggesting that H_2 adsorption reaches critical coverage on the Pt surface. However, the voltammetry does not evolve with stress, suggesting that the surface properties of Pt are unaffected.[78-80]

Figure 2.8b also shows that in the 1st cycle, the cathodic stress is more compressive than the anodic stress. This data agrees with that shown in Figure 2.5b when Pt is cycled between the double layer region and OER. This difference in cathodic and anodic stress could be explained by surface repulsion caused by place-exchanged oxygen (O_{ex}), and/or adsorption of O_2 ($O_{2\text{-}ad}$) generated at OER on the Pt surface. Those strains release when potential is swept back to the double layer region. Thus the stress returns back to its original value, as seen the crossing at *ca.* 0.5 V in Figure 2.8 and Figure 2.5. From the 2nd cycle, there is no large gap in stress between the anodic and cathodic sweeps (between 0.5 V and 1.5 V), as seen in the 1st cycle. Cathodic and anodic stress here are identical and overlapped.

In another words, after H_2 is generated and adsobed for the first time, no evidence of O_{ex}, and/or $O_{2\text{-}ad}$ could be found in the oxygen region. This result suggests that residual H_2 blocks O_{ex} and/or $O_{2\text{-}ad}$ from happening on the Pt electrode. This result might also suggest that two processes with opposite effects (H_2 desorption causing tensile stress, and O_{ex} and/or $O_{2\text{-}ad}$ causing compressive stress) occur at the same time, resulting in no net change in stress. . However, if the exchange between H_2 and O_{ex} or O_{2ad} occurs, differences in size of these species should cause some change in the measured stress.

2.4. Discussion

The data presented above show that each electrode studied is dynamic, with a variety of different processes occurring during redox cycling. The derivative of the stress with respect to potential generally correlates well with the voltammetry, and shows that there are no stress changes during the OER itself, demonstrating that the oxidation state of the electrode material present just prior to the OER is maintained during the OER.

Long term cycling studies show that some of the electrodes studied here are dynamic. While Ni and Co exhibit reversible stress-potential behavior, such is not true for Pt, Au, or Ir, where the stress develops with time. For Au, this evolution might be a result of electrode dissolution or place exchange occurring during electrode surface oxidation. For Pt and Ir, however, the exact stress evolution depends on electrode history, with slow reduction of oxides found for Ir and hysteresis associated with the HER found for Pt.

2.4.1. Calculation of strain from the stress measurements

We next examined whether the stress measurement coupled with the voltammetry could provide quantitative insight into the strain associated with electrode oxidation itself.

Stress is proportional to the (elastic) strain via the Young's modulus of a material:[81]

$$\frac{\Delta f}{s} = \sigma = \epsilon Y$$

where Δf is the stress (N/m), s is the thickness of the oxide film (m), σ is the stress/thickness in the film (Pa), ϵ is the strain in the film, and Y is the Young's modulus of the film (Pa). The interatomic expansion/contraction is related to the strain:

$$\epsilon = \frac{\Delta D}{a}$$

where ΔD is the change in interatomic distance and a is the interatomic distance (Å).

The potential range where oxidation of Ni and Co electrode from hydroxide to oxyhydroxide was interrogated. The thickness of the oxyhydroxide film was calculated from the integrated oxidation current as described in the experimental section. Assuming that only β-oxyhydroxide is produced over the range of the interrogated potential with 100% current efficiency, the thickness (s) of the oxyhydroxide layer is reported in Table 2.1. Young's modulus of $Ni(OH)_2$ sample was found to be 6.5 GPa and Young's modulus of $Co(OH)_2$ sample was found to be 14.9 GPa by nanoindentation measurements. We assume here that the Young's modulus is isotropic, as is likely given the thickness of the film probed during the Young's modulus determination. We also assume that the Young's modulus of the oxide film is constant over the range of interrogated potential. Pt, Ir, and Au were not considered due to the difficulty encountered in distinguishing oxidation peaks, calculating oxide product thickness and measuring the Young's modulus of the thin oxide on these metals formed at high potentials. These values are additionally not reported in the literature.

Table 2.1 reports the contraction calculated from the experimentally determined stress, oxide thickness, and Young's modulus. The table shows that the in-plane contractions going from the hydroxide to the oxyhydroxide so determined range from 0.2 to 0.3 Å. These numbers can be compared with those determined by the in-plane change in unit cell parameters between the two oxide forms. Both the hydroxide and the oxyhydroxide forms are thought to grow with the c-axis perpendicular to the electrode surface,[82,83] so only the a-axis change is considered here. The table shows that the value obtained by the a_0 (i.e M-M bond) change between the hydroxide and

oxyhydroxide forms agrees well with that determined from the stress, electrochemistry, and nanoindentation measurements. The agreement provides an indication that the stress measurements are in both qualitative and quantitative agreement with known changes in oxide strain.

Table 2.1. Calculation of bond contraction from changes in electrochemical stress.

	$\lvert\Delta f\rvert$ (N/m)	s (Å)	σ (GPa)	Y (GPa)	ϵ %	In plane contraction calculated from stress ΔD^* (Å)	M-M bond distance (Å)		Contraction calculated from unit cell change* (Å)
							Red form	Ox form	
Ni	0.72	21.1	0.45	6.5	7.0%	0.22	$Ni(OH)_2$ 3.13[23,54]	NiOOH 2.82[23,54]	0.31 (9.9%)
Co	20.5	163.3	1.26	14.9	8.4%	0.27	$Co(OH)_2$ 3.17[30]	CoOOH 2.85[30]	0.32 (10.0%)

2.4.2. Correlation of oxidation charge density and absolute change in stress

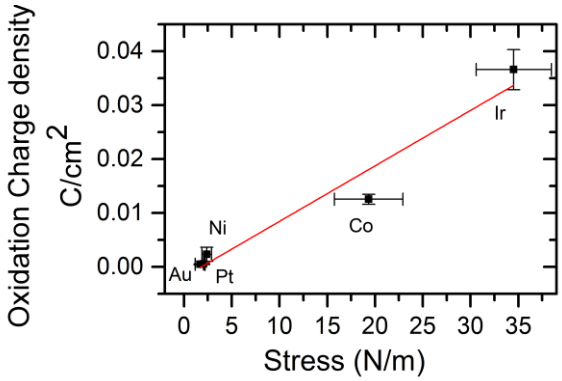

Figure 2.9. Correlation of oxidation charge density and absolute change in stress of Au, Pt, Ni, Co, and Ir.

We next compare the measured stress change with the amount of oxide formed during electrode oxidation. Figure 2.9 shows the correlation between oxidation charge density and the absolute change in stress during this process. The figure shows that there is a roughly linear relationship between the change in stress and the amount of oxide formed. Ir exhibits the greatest

amount of charge formed during oxidation and correspondingly exhibits the largest stress change (first cycle). Au and Pt, on the other hand, form only a surface oxide during electrode oxidation and exhibit relatively little stress change. Thus, change in stress is simply proportional to the amount of material that is further oxidized.

Oxidation charge density was calculated from oxidation current curve from CV and geometric area of each electrode. The surface roughness for each electrode is assumed to be similar. Moreover, the differences in charge density relate to differing degrees of bulk oxidation of the material, which is only weakly affected by the surface roughness.

Differences in the amount of oxide formed going from Au to Ir are related to differences in the properties of the oxide itself. A model of the oxide film growing on Ir is proposed by Conway[84] based on the change of conductivity and porosity of oxide layers. At low anodic potential Ir metal is oxidized to Ir(III), which is poorly conductive, but exhibits a highly porous structure and is loosely bound to the Ir metal surface. The porous structure leads to significant electrolyte availability at metal/oxide interface, thus allowing numerous hydroxide layers to grow. As the potential becomes more positive, Ir metal and Ir(III) are oxidized to Ir(IV), which is less porous but very conductive.[85,86] This conductivity facilitates the electron transfer process with which the electrode itself is bulk oxidized. Au and Pt only form a few oxide monolayers because of the low conductivity of their oxides.[87] Additionally, during the growth process dipolar ($Au^{\delta+}OH^{\delta-}$ and $Pt^{\delta+}OH^{\delta-}$) species are produced. At appreciable coverage, they repel one another and this repulsion raises the energy required to generate additional oxides.[88] The hydroxide and oxyhydroxide of Co and Ni are less conductive[89,90] than Ir oxides, so they form fewer layers relative to those formed by Ir. However, Co and Ni hydroxides and oxyhydroxides exhibit a loose,

layered structure with weak interaction between layers. This allows electrolyte intercalation, which facilitates bulk oxide formation.[23,52]

2.4.3. Correlation of OER activity and the amount of oxide formed

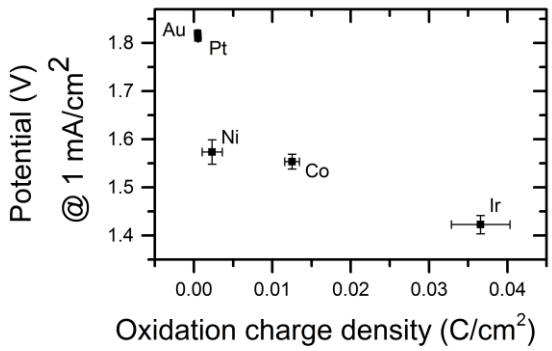

Figure 2.10. Correlation of potential at 1 mA/cm^2 of OER and oxidation charge density of Au, Pt, Ni, Co, Ir.

We next compare the amount of oxide formed during electrode oxidation with their OER activities. Figure 2.10 shows the correlation between potential at 1 mA/cm^2 of OER and oxidation charge density. The figure shows that there is a trend that metal with larger amount of oxide formed prior to OER show higher activity (lower potential is required to drive OER to 1 mA/cm^2). The origin of this trend is likely related to similarities between the mechanism of water and hydroxide activation required to form the oxide in the first place, and the mechanism of the OER, thought to involve formation of M-OH and M=O species.[3,4,8]

2.5. Conclusions

In this work, the changes in surface stress of Ir, Ni, Co, Au and Pt electrode in alkaline solution were measured by the bending-beam method. Each electrode studied is dynamic, with a variety of different processes occurring as the electrode during redox cycling. The stress measurements report directly on changes in oxidation state of the electrode as the potential is moved from cathodic to anodic values and back again. Hysteresis in the stress relates to irreversibility in electrode composition, particularly for Ir. The stress measurements also show that the oxide formed just prior to the OER onset does not change substantially (at least in-plane) during the OER, a result which shows that water oxidation deep in the film during the OER is unlikely. At least in systems where the Young's modulus can be measured, the stress quantitatively reports on the in plane change in strain during oxide oxidation, which provides further utility to these measurements. We also show that the magnitude of the change in stress is proportional to the amount of material that is further oxidized. The similarity between processes yielding higher oxides and those involved with the OER mechanism yields are rough correlation between film thickness and OER onset.

2.6. References

(1) Doyle, R. L.; Godwin, I. J.; Brandon, M. P.; Lyons, M. E. G. *Physical Chemistry Chemical Physics* **2013**, *15*, 13737-13783.

(2) Laguna-Bercero, M. A. *Journal of Power Sources* **2012**, *203*, 4-16.

(3) Man, I. C.; Su, H. Y.; Calle-Vallejo, F.; Hansen, H. A.; Martinez, J. I.; Inoglu, N. G.; Kitchin, J.; Jaramillo, T. F.; Norskov, J. K.; Rossmeisl, J. *Chemcatchem* **2011**, *3*, 1159-1165.

(4) Lyons, M. E. G.; Brandon, M. P. *International Journal of Electrochemical Science* **2008**, *3*, 1386-1424.

(5) Reier, T.; Oezaslan, M.; Strasser, P. *Acs Catalysis* **2012**, *2*, 1765-1772.

(6) Lyons, M. E. G.; Brandon, M. P. *Journal of Electroanalytical Chemistry* **2010**, *641*, 119-130.

(7) Hall, D. E. *Journal of the Electrochemical Society* **1985**, *132*, C41-C48.

(8) Dau, H.; Limberg, C.; Reier, T.; Risch, M.; Roggan, S.; Strasser, P. *Chemcatchem* **2010**, *2*, 724-761.

(9) Miles, M. H.; Kissel, G.; Lu, P. W. T.; Srinivasan, S. *Journal of the Electrochemical Society* **1976**, *123*, 332-336.

(10) Rossmeisl, J.; Logadottir, A.; Norskov, J. K. *Chemical Physics* **2005**, *319*, 178-184.

(11) Godwin, I. J.; Lyons, M. E. G. *Electrochemistry Communications* **2013**, *32*, 39-42.

(12) Jaksic, M. M.; Johansen, B.; Tunold, R. *International Journal of Hydrogen Energy* **1994**, *19*, 321-335.

(13) Behl, W. K.; Toni, J. E. *Journal of Electroanalytical Chemistry and Interfacial Electrochemistry* **1971**, *31*, 63-75.

(14) Desilvestro, J.; Corrigan, D. A.; Weaver, M. J. *Journal of the Electrochemical Society* **1988**, *135*, 885-892.

(15) Melendres, C. A.; Xu, S. *Journal of the Electrochemical Society* **1984**, *131*, 2239-2243.

(16) Yeo, B. S.; Bell, A. T. *Journal of Physical Chemistry C* **2012**, *116*, 8394-8400.

(17) Bewick, A.; Gutiérrez, C.; Larramona, G. *Journal of Electroanalytical Chemistry* **1992**, *333*, 165-175.

(18) Ismail, K. M.; Badawy, W. A. *Journal of Applied Electrochemistry* **2000**, *30*, 1303-1311.

(19) Kötz, R.; Neff, H.; Stucki, S. *Journal of the Electrochemical Society* **1984**, *131*, 72-77.

(20) Peuckert, M. *Electrochimica Acta* **1984**, *29*, 1315-1320.

(21) Foelske, A.; Strehblow, H. H. *Surface and Interface Analysis* **2002**, *34*, 125-129.

(22) Pralong, V.; Delahaye-Vidal, A.; Beaudoin, B.; Gerand, B.; Tarascon, J. M. *Journal of Materials Chemistry* **1999**, *9*, 955-960.

(23) Medway, S. L.; Lucas, C. A.; Kowal, A.; Nichols, R. J.; Johnson, D. *Journal of Electroanalytical Chemistry* **2006**, *587*, 172-181.

(24) Totir, D.; Mo, Y.; Kim, S.; Antonio, M. R.; Scherson, D. A. *Journal of the Electrochemical Society* **2000**, *147*, 4594-4597.

(25) Mo, Y.; Stefan, I. C.; Cai, W.-B.; Dong, J.; Carey, P.; Scherson, D. A. *The Journal of Physical Chemistry B* **2002**, *106*, 3681-3686.

(26) Hillman, A. R.; Skopek, M. A.; Gurman, S. J. *Physical Chemistry Chemical Physics* **2011**, *13*, 5252-5263.

(27) Li, X. H.; Walsh, F. C.; Pletcher, D. *Physical Chemistry Chemical Physics* **2011**, *13*, 1162-1167.

(28) Yau, S.-L.; Fan, F.-R. F.; Moffat, T. P.; Bard, A. J. *The Journal of Physical Chemistry* **1994**, *98*, 5493-5499.

(29) Kong, F.; Kostecki, R.; McLarnon, F.; Muller, R. H. *Thin Solid Films* **1998**, *313–314*, 775-780.

(30) Lu, P. W. T.; Srinivasan, S. *Journal of the Electrochemical Society* **1978**, *125*, 1416-1422.

(31) Kowal, A.; Niewiara, R.; Perończyk, B.; Haber, J. *Langmuir* **1996**, *12*, 2332-2333.

(32) Hu, Y.; Scherson, D. A. *The Journal of Physical Chemistry B* **1997**, *101*, 5370-5376.

(33) Birss, V. I.; Elzanowska, H.; Gottesfeld, S. *Journal of Electroanalytical Chemistry* **1991**, *318*, 327-333.

(34) Juodkazyte, J.; Sebeka, B.; Stalnionis, G.; Juodkazis, K. *Electroanalysis* **2005**, *17*, 1734-1739.

(35) Mo, Y.; Hwang, E.; Scherson, D. A. *Journal of the Electrochemical Society* **1996**, *143*, 37-43.

(36) Zhen, C. H.; Sun, S. G.; Fan, C. J.; Chen, S. P.; Mao, B. W.; Fan, Y. J. *Electrochimica Acta* **2004**, *49*, 1249-1255.

(37) Haiss, W. *Reports on Progress in Physics* **2001**, *64*, 591-648.

(38) Lang, G. G. *Laser techniques for the study of electrode processes*; Springer: New York, 2012.

(39) Kongstein, O. E.; Bertocci, U.; Stafford, G. R. *Journal of the Electrochemical Society* **2005**, *152*, C116-C123.

(40) Viswanath, R. N.; Kramer, D.; Weissmuller, J. *Electrochimica Acta* **2008**, *53*, 2757-2767.

(41) Zangmeister, C. D.; Bertocci, U.; Beauchamp, C. R.; Stafford, G. R. *Electrochimica Acta* **2008**, *53*, 6778-6786.

(42) Heaton, T.; Friesen, C. *The Journal of Physical Chemistry C* **2007**, *111*, 14433-14439.

(43) Seo, M.; Serizawa , Y. *Journal of the Electrochemical Society* **2003**, *150*, E472-E476.

(44) Viswanath, R. N.; Kramer, D.; Weissmuller, J. *Langmuir* **2005**, *21*, 4604-4609.

(45) Schlesinger, M.; Paunovic, M. *Modern electroplating*; 5th ed.; Wiley: Hoboken, NJ, 2010.

(46) El Sawy, E. N.; Birss, V. I. *Journal of the Electrochemical Society* **2013**, *160*, D386-D393.

(47) Tavassol, H.; Chan, M. K. Y.; Catarello, M. G.; Greeley, J.; Cahill, D. G.; Gewirth, A. A. *Journal of the Electrochemical Society* **2013**, *160*, A888-A896.

(48) Zhang, X. J.; Cahill, D. G. *Langmuir* **2006**, *22*, 9062-9066.

(49) Stoney, G. G. In *Proceedings of the Royal Society of London Series a-Containing Papers of a Mathematical and Physical Character* 1909; Vol. 82, p 172-175.

(50) Li, X.; Gao, H.; Murphy, C. J.; Caswell, K. K. *Nano Letters* **2003**, *3*, 1495-1498.

(51) Pourbaix, M. *Atlas of electrochemical equilibria in aqueous solutions*; 2nd English ed.; National Association of Corrosion Engineers: Houston, Tex., 1974.

(52) Trotochaud, L.; Ranney, J. K.; Williams, K. N.; Boettcher, S. W. *Journal of the American Chemical Society* **2012**, *134*, 17253-17261.

(53) Lyons, M. E. G.; Doyle, R. L.; Godwin, I.; O'Brien, M.; Russell, L. *Journal of the Electrochemical Society* **2012**, *159*, H932-H944.

(54) Oliva, P.; Leonardi, J.; Laurent, J. F.; Delmas, C.; Braconnier, J. J.; Figlarz, M.; Fievet, F.; Guibert, A. d. *Journal of Power Sources* **1982**, *8*, 229-255.

(55) Vuković, M. *Journal of Applied Electrochemistry* **1994**, *24*, 878-882.

(56) Hahn, F.; Floner, D.; Beden, B.; Lamy, C. *Electrochimica Acta* **1987**, *32*, 1631-1636.

(57) Badawy, W. A.; Al-Kharafi, F. M.; Al-Ajmi, J. R. *Journal of Applied Electrochemistry* **2000**, *30*, 693-704.

(58) Liu, T. C.; Pell, W. G.; Conway, B. E. *Electrochimica Acta* **1999**, *44*, 2829-2842.

(59) Simpraga, R. P. *Journal of Electroanalytical Chemistry* **1993**, *355*, 79-96.

(60) Simmons, G. W.; Kellerman, E.; Leidheiser, H. *Journal of the Electrochemical Society* **1976**, *123*, 1276-1284.

(61) Gerken, J. B.; McAlpin, J. G.; Chen, J. Y. C.; Rigsby, M. L.; Casey, W. H.; Britt, R. D.; Stahl, S. S. *Journal of the American Chemical Society* **2011**, *133*, 14431-14442.

(62) Chenavas, J.; Joubert, J. C.; Marezio, M. *Solid State Communications* **1971**, *9*, 1057-1060.

(63) Juodkazytė, J.; Šebeka, B.; Valsiunas, I.; Juodkazis, K. *Electroanalysis* **2005**, *17*, 947-952.

(64) Buckley, D. N.; Burke, L. D. *Journal of the Chemical Society, Faraday Transactions 1: Physical Chemistry in Condensed Phases* **1975**, *71*, 1447-1459.

(65) Buckley, D. N.; Burke, L. D.; Mulcahy, J. K. *Journal of the Chemical Society, Faraday Transactions 1: Physical Chemistry in Condensed Phases* **1976**, *72*, 1896-1902.

(66) Bruckenstein, S.; Shay, M. *Journal of Electroanalytical Chemistry and Interfacial Electrochemistry* **1985**, *188*, 131-136.

(67) Diaz-Morales, O.; Calle-Vallejo, F.; de Munck, C.; Koper, M. T. M. *Chemical Science* **2013**, *4*, 2334-2343.

(68) Sargent, A.; Sadik, O. A.; Matienzo, L. J. *Journal of the Electrochemical Society* **2001**, *148*, C257-C265.

(69) Mayrhofer, K. J. J.; Wiberg, G. K. H.; Arenz, M. *Journal of the Electrochemical Society* **2008**, *155*, P1-P5.

(70) El-Shafei, A. A.; El-Maksoud, S. A. A.; Moussa, M. N. H. *Journal of Electroanalytical Chemistry* **1992**, *336*, 73-83.

(71) El Sawy, E. N.; Birss, V. I. *Journal of Materials Chemistry* **2009**, *19*, 8244-8252.

(72) Steegstra, P.; Busch, M.; Panas, I.; Ahlberg, E. *The Journal of Physical Chemistry C* **2013**, *117*, 20975-20981.

(73) Burke, L. D.; Nugent, P. F. *Gold Bulletin* **1998**, *31*, 39-50.

(74) Topalov, A. A.; Cherevko, S.; Zeradjanin, A. R.; Meier, J. C.; Katsounaros, I.; Mayrhofer, K. J. J. *Chemical Science* **2014**, *5*, 631-638.

(75) Merzougui, B.; Swathirajan, S. *Journal of the Electrochemical Society* **2006**, *153*, A2220-A2226.

(76) Markovic, N. M.; Gasteiger, H. A.; Philip, N. *Journal of Physical Chemistry* **1996**, *100*, 6715-6721.

(77) Oudenhuijzen, M. K.; Bitter, J. H.; Koningsberger, D. C. *Journal of Physical Chemistry B* **2001**, *105*, 4616-4622.

(78) Raudonis, R.; Plausinaitis, D.; Daujotis, V. *Journal of Electroanalytical Chemistry* **1993**, *358*, 351-356.

(79) Dong, Y.; Hu, G.; Hu, X.; Xie, G.; Lu, J.; Luo, M. *The Journal of Physical Chemistry C* **2013**, *117*, 12537-12543.

(80) Frelink, T.; Visscher, W.; van Veen, J. A. R. *Electrochimica Acta* **1995**, *40*, 545-549.

(81) Stoney, G. G. *Proceedings of the Royal Society of London. Series A, Containing Papers of a Mathematical and Physical Character* **1909**, *82*, 172-175.

(82) Delahayevidal, A.; Beaudoin, B.; Figlarz, M. *Reactivity of Solids* **1986**, *2*, 223-233.

(83) Delahayevidal, A.; Figlarz, M. *Journal of Applied Electrochemistry* **1987**, *17*, 589-599.

(84) Conway, B. E.; Mozota, J. *Electrochimica Acta* **1983**, *28*, 9-16.

(85) Trupina, L.; Miclea, C.; Tanasoiu, C.; Amarande, L.; Miclea, C. T.; Cioangher, M. *Journal of Optoelectronics and Advanced Materials* **2007**, *9*, 1508-1510.

(86) Ryden, W. D.; Lawson, A. W. *Physical Review B* **1970**, *1*, 1494-&.

(87) Maya, L.; Riester, L.; Thundat, T.; Yust, C. S. *Journal of Applied Physics* **1998**, *84*, 6382-6386.

(88) Burke, L. D.; Nugent, P. F. *Gold Bulletin* **1997**, *30*, 43-53.

(89) Ueta, H.; Abe, Y.; Kato, K.; Kawamura, M.; Sasaki, K.; Itoh, H. *Japanese Journal of Applied Physics* **2009**, *48*.

(90) Morishita, M.; Kakeya, T.; Kanemoto, M.; Kodama, M.; Sakai, T. *Journal of the Electrochemical Society* **2012**, *159*, A2069-A2075.

Chapter 3

High Activity Oxygen Evolution Reaction Catalysts from Additive-Controlled Electrodeposited Ni and NiFe Films

3.1. Introduction

The electrochemical splitting of water offers an attractive way to provide a carbon-free source of hydrogen.[1,2] Water splitting efficiency is limited primarily by the high overpotential (η) required by the anodic oxygen evolution reaction (OER, $4OH^- \rightarrow 2H_2O + 4e^- + O_2$ in alkaline or $2 H_2O \rightarrow O_2 + 4 H^+ + 4 e^-$ in acid).[2,3] In alkaline electrolyte, non-precious metals such as Ni, Co, and their alloys (NiFe, CoFe, etc.) are used as electrocatalysts for the OER, since they are abundant, cheap, and exhibit high corrosion resistance. However, these materials still exhibit η = 350-450 mV relative to the thermodynamic value of 1.23 V vs.[4,5] at a nominal 10 mA/cm^2 current density (j).[3,6,7] Stability and reasonable activity at high j (500 mA/cm^2) remains a challenge.[8]

Tremendous amount of effort has been invested to develop active and stable non-precious metal catalysts for OER in alkaline solutions. One way is to introduce Fe into Ni-containing materials.[9-13] To further enhance the OER activity of Ni, NiFe and Co-based materials, another strategy is to fabricate them into nanoparticles to increase the number of active sites per geometric area. Currently, most high activity catalysts for the OER in alkaline electrolyte are nanostructured Co_xO_y, $Ni(OH)_2$, and $Ni_xFe_y(OH)_2$ powders,[13-15] which are glued on electrode surface by binders

such as Nafion. However, these 'glued' nanoparticles exhibit poor stability under conditions of high OER current density where vigorous gas evolution occurs. Additionally, the use of binders decreases contact between and conductivity of the electrode and electrolyte, leading to diminished activity.[16]

Another active Ni OER catalyst is formed from Raney Ni - a Ni alloy with Al or Zn.[17,18] In alkaline solution, Al and Zn is leached from the Ni to produce a high surface area material. Raney Ni exhibits a 50 mV decrease in η relative to Ni foil, i.e. ~1.53 V vs RHE, for the OER at j = 1 mA/cm^2.[17]

Precipitation of $Ni(OH)_2$, and $Ni_xFe_y(OH)_2$ from nitrate solution onto electrode surfaces has long been used to yield porous catalysts exhibiting high OER activity.[19-21] In this method, $Ni(OH)_2$ and/or $Ni_xFe_y(OH)_2$ is formed and precipitated from a metal salt near the electrode by OH^- produced during NO_3^- reduction. While active at low loadings, these materials exhibit poor stability at high loadings because the precipitated hydroxide is loosely bound to the underlying electrode. Additionally, thick precipitates limit access to underlying material and inhibit charge and electrolyte transfer between substrate and hydroxide.[16,19] A recent application of this method used thin layer of $Ni_xFe_y(OH)_2$ precipitated on macroporous Ni foam substrates to yield j = 100 mA/cm^2 at ~ 1.6 V vs RHE in 1 M NaOH.[16] For thicker deposits, pulse-deposition improves the adhesion between the deposited layers and the substrate as well as conductivity of the whole film.[22]

In this chapter, we present a simple, single-step electrodeposition method with which to fabricate nanostructured, fractal-like Ni, and NiFe catalysts exhibiting high OER activity. Using electrodeposition we constructed a NiFe film exhibiting an OER j = 100 mA/cm^2 , i.e mass activity ~ 1200 A/g of catalyst at η = 300 mV (1.53V vs RHE) in 1M NaOH which is among the most active OER electrocatalyst in alkaline electrolyte reported to date. Moreover, we can tune this

current density to nearly any arbitrary value by altering amount of NiFe electrodeposited, without any evidence of material or activity degradation due to the metallic nature of the initial deposit.

3.2. Experimental section

Deposition of metal: Ni, NiFe, and Co were electrodeposited galvanostatically at a constant current density of -4 mA/cm^2 until a final deposition charge was reached (typically 2 C/cm^2, unless otherwise stated). A 10 sec resting time after passage of each 0.8 - 1 C/cm^2 was applied in order to minimize formation of deleterious concentration gradients. Au, Pt, Ni foil, Ni foam, stainless steel, and Fluorine-doped Tin Oxide (FTO) were used as the deposition substrates. Pt or glassy carbon were used as counter electrodes and separated from the working electrode by a glass frit in an electrochemical H-cell. A 'leakless' Ag/AgCl (eDAQ) electrode was placed near the working to measure the deposition potential.

Substrates for electrodeposition were cleaned just before used. Au (200 nm thickness, fabricated on one side of glass coverslips by e-beam deposition) was rinsed with Milli-Q water, and then flamed under H_2. Stainless steel disks were mechanically polished with sand paper, immersed in 0.1 M H_2SO_4 for 2 minutes to remove the native oxide layer, and then rinsed thoroughly with Milli-Q water. Ni foil (Sigma Aldrich, thickness 0.125 mm, purity 99.9%) and Ni foam (MTI corporation, purity 99.99%, density 346 g/m^2, 80-110 pores per inch, average hole diameter 0.25mm) were immersed in 0.1 M H_2SO_4 for 2 minutes to remove the native oxide layer, and then rinsed thoroughly with Milli-Q water. Deposition current was calculated from the geometric area of each substrate, which was typically ~ 1 cm^2. Each deposition bath contained typically ~ 15 ml solution.

The Ni plating baths were made from 0.5 M $NiSO_4.6H_2O$ + 0.4 M H_3BO_3 adjusted to pH 3 with H_2SO_4 and plating was performed either without an additive, or with 4 mM of 3,5-diamino-1,2,4-triazole (DAT), 10 mM of 3-Amino-1,2,4-triazole (AT), or 30 mM of 1,2,4-triazole-3,4,5-triamine (TAT). The Ni and NiFe plating baths were made from (0.5 M - 0.25 M) $NiSO_4.6H_2O$ + 0.4 M H_3BO_3 + $FeSO_4.7H_2O$ (0 M - 0.25 M), adjusted to pH 3 with H_2SO_4 and plating was performed either without an additive, or with 3,5-diamino-1,2,4-triazole (DAT). Concentration of metal ions (Ni^{2+} and Fe^{2+}) in deposition solutions equaled to 0.5 M in total. The ratio of Ni/Fe is measured by ICP-OES (Table 1). The Co plating baths were made from 0.5 M $CoSO_4.7H_2O$ + 0.4 M H_3BO_3, adjusted to pH 3 with H_2SO_4 and plating was performed either without an additive, or with 4 mM of 3,5-diamino-1,2,4-triazole (DAT).

Table 3.1. Composition of NiFe platting bath and film composition measured by ICP-OES.

$NiSO_4$	$FeSO_4$	NiFe film composition (±5%)
0.5 M	0 M	Ni
0.475 M	0.025 M	$Ni_{90}Fe_{10}$
0.375 M	0.125 M	$Ni_{50}Fe_{50}$
0.25 M	0.25 M	$Ni_{30}Fe_{70}$

Material characterization: The amount of Ni, Co, and NiFe electrodeposited on Au substrate was measured by ICP-OES, which was carried out on a PerkinElmer 2000 DV, optical emission spectrometer in the UIUC SCS microanalysis laboratory. Scanning electron microscope (SEM) images were obtained from a Hitachi A-4700 high resolution microscope with an emission gun capable of 2.5 nm resolution. The Ni, Fe and N in the electrodeposited samples was determined

by using X-Ray Photoelectron Spectroscopy (XPS) (Physical Electronics PHI 5400). Atomic force microscopy (AFM) images were obtained in tapping mode using Asylum Research MFP-3D AFM.

Electrochemical measurements: Cyclic voltammetry (CV), chronoamperometry (CA) and chronopotentiometry (CP) were performed at room temperature using a CHI 760D or Biologic SP-150 with a Pt mesh counter electrode and an Ag/AgCl reference electrode. Before the electrochemical measurement, the electrolyte (1 M NaOH, pH=14) was purged by Ar. The Ag/AgCl reference electrode was calibrated before each experiment with an RHE in 1M NaOH. Potential are reported with respect to RHE, unless otherwise stated. The voltammetry was IR corrected. Mass activity (A/g of catalyst) was calculated from the measured current (A) and the amount of catalyst that electrodeposited (g). Turnover frequency of catalysts (TOF) was calculated using the following equation:

$$TOF = \frac{mol\ of\ O_2\ generated/sec}{mol\ of\ metal} = \frac{\frac{j(\frac{A}{cm^2})}{4 \times F(\frac{C}{mol})}}{mol\ of\ total\ metal}$$

where the mol of metal was calculated by integrating the oxidation peak of the M(II)/M(III) wave.

3.3. Results

3.3.1. Electrodeposition of Ni-nanostructures

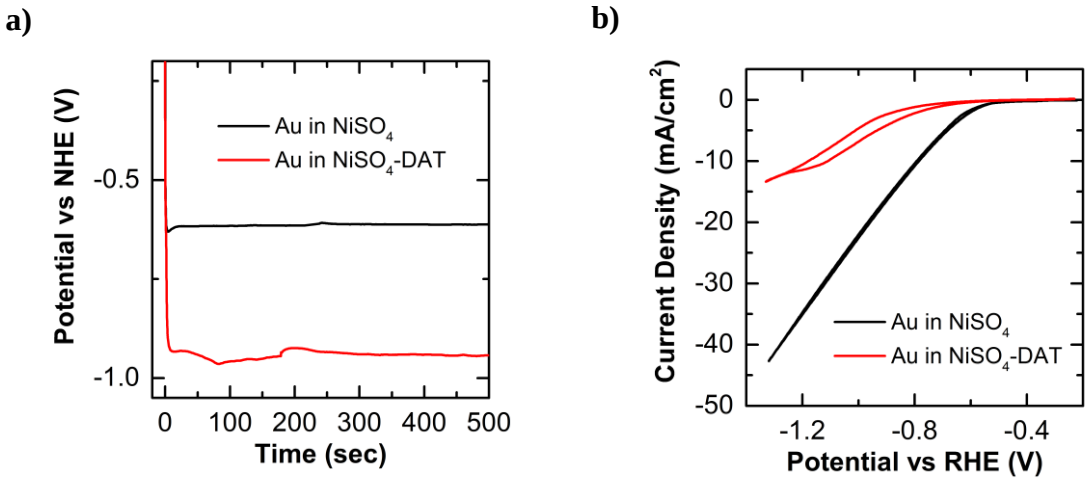

Figure 3.1. a) Chronopotentiometry at – 4mA/cm^2; and b) CV at scan rate 10 mV/s of Au electrode in Ni-deposition solutions with and without DAT.

Figure 3.1a shows the electrodeposition profile of Ni with DAT as additive (Ni-DAT film), and without DAT (Ni film) on an Au substrate. A deposition current of – 4 mA/cm^2 was obtained at ~ – 0.9 V and – 0.6 V vs NHE, respectively. Figure 3.1b shows CVs obtained from Au substrates in the Ni deposition solutions with and without DAT from – 0.2 V to – 1.3 V where H_2 evolution and Ni deposition occur simultaneously. With the same concentration of Ni^{2+}, the current density in the additive-free solution is higher than in the presence of DAT. Chronopotentiometry and CV both indicate that DAT inhibits Ni deposition and/or the hydrogen evolution reaction. ICP-OES data shows that the Coulombic efficiency of Ni electrodeposited in the additive-free solution is 91 ± 3 %, while the Coulombic efficiency of Ni electrodeposited with DAT is 14 ± 3 %. Low deposition efficiency of solution containing DAT once again indicates that DAT inhibits Ni electrodeposition.

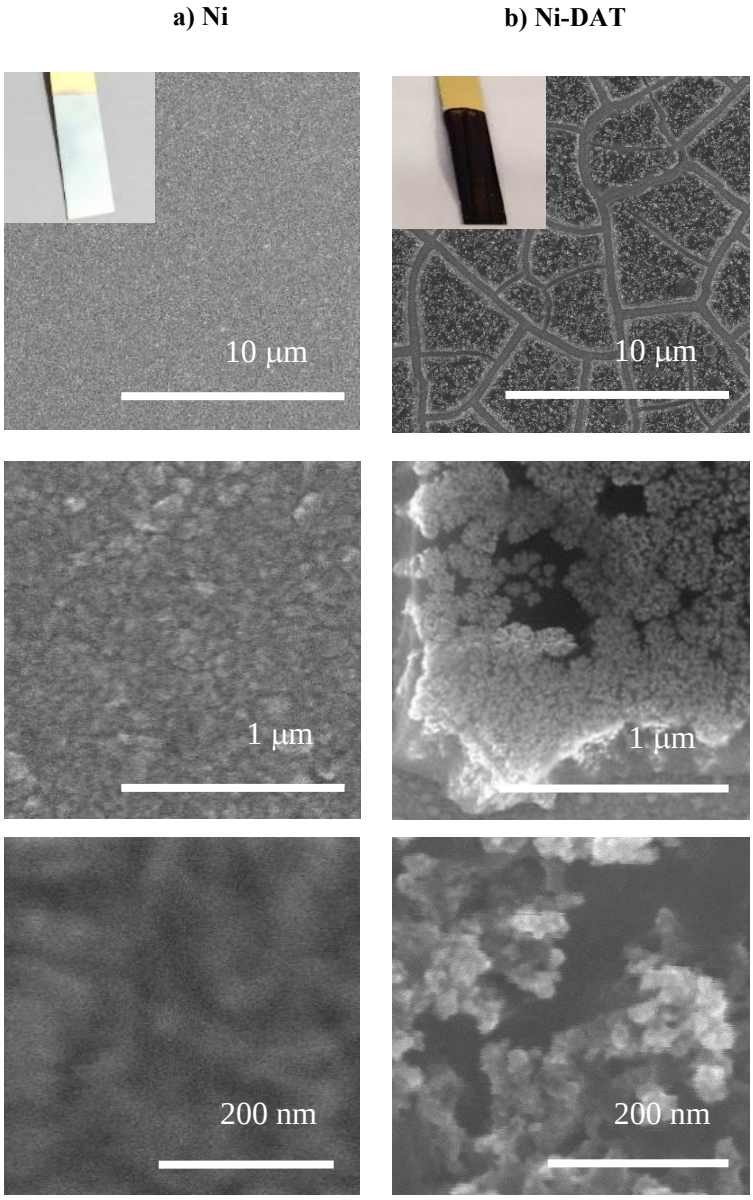

Figure 3.2. SEM images of a) Ni and b) Ni-DAT film electrodeposited on Au substrate. The photos show an optical image of the electrodeposited films.

Figure 3.2 shows SEM images of the Ni film electrodeposited with and without DAT. Without the additive, the Ni film exhibits a shiny metallic color (Figure 3.2a, inset). SEM (Figure 3.2a) and AFM (Figure 3.3a) show that the film is smooth with roughness of 7.6 nm ± 2.1 nm.

Analysis of the AFM image shows that the measured and geometric surface area are roughly the same ($A_{measured}/A_{geometric}$ = 1.02 ± 0.01). In contrast, the Ni film deposited with DAT (Ni-DAT) exhibits a black color (Figure 3.2b, inset). SEM images of Ni-DAT film at different magnifications (Figure 3.2b) show that the Ni-DAT film exhibits a cracked and porous surface with apparent agglomerated clusters of particles. The roughness of the Ni-DAT film from AFM (Figure 3.3b) is 226 nm ± 70 nm. The ratio of the measured and geometric surface area is $A_{measured}/A_{geometric}$ = 1.80 ± 0.12. Interestingly, XPS measurements (Figure 3.4) evince no detectible N on the electrode after cycling, which suggests that any retained DAT is oxidized and removed from the electrode during the OER.

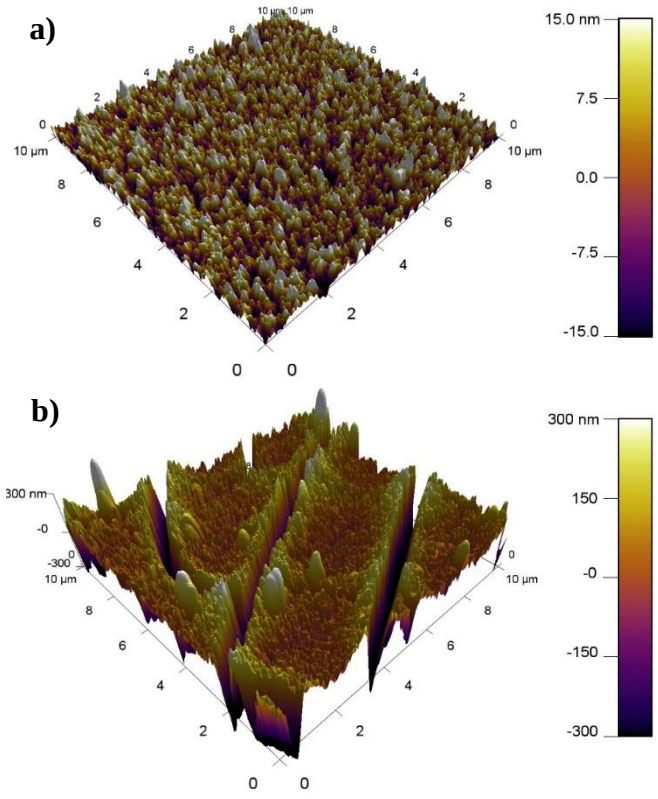

Figure 3.3. AFM of a) Ni film electrodeposited on Au substrate (without additive); and b) Ni-DAT film electrodeposited on Au substrate (with DAT).

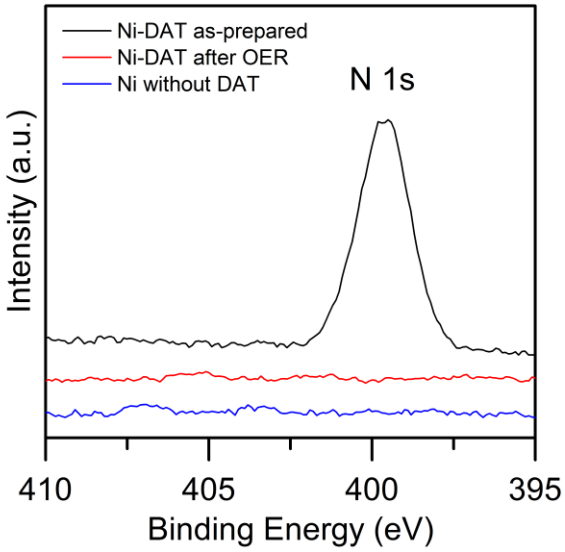

Figure 3.4. XPS spectra of N 1s in Ni and Ni-DAT films.

3.3.2. OER activity of Ni films

Figure 3.5a shows an iR corrected CV obtained from Ni or Ni-DAT deposited on Au in 1 M NaOH. In alkaline solution the Ni surface is spontaneously oxidized to $Ni(OH)_2$.[23,24] Following first cycle oxidation of Ni to $Ni(OH)_2$,[24] $Ni(OH)_2$ is oxidized to form NiOOH at ~1.4 V. The inset of Figure 3.5a shows the CV of a Ni film electrodeposited from additive-free solution in NaOH, which is similar to that reported previously.[3,24,25] The red line in Figure 3.5a shows the CV of the Ni-DAT film. The CV shows the substantially larger current density associated with the Ni-DAT film relative to Ni alone. The charge associated with the $Ni(OH)_2$/NiOOH wave of Ni-DAT film is 113 ± 18 times larger than the corresponding wave for the Ni film. Interestingly, the amount of Ni in the NiDAT film is only ~ 15% of that in the Ni film.

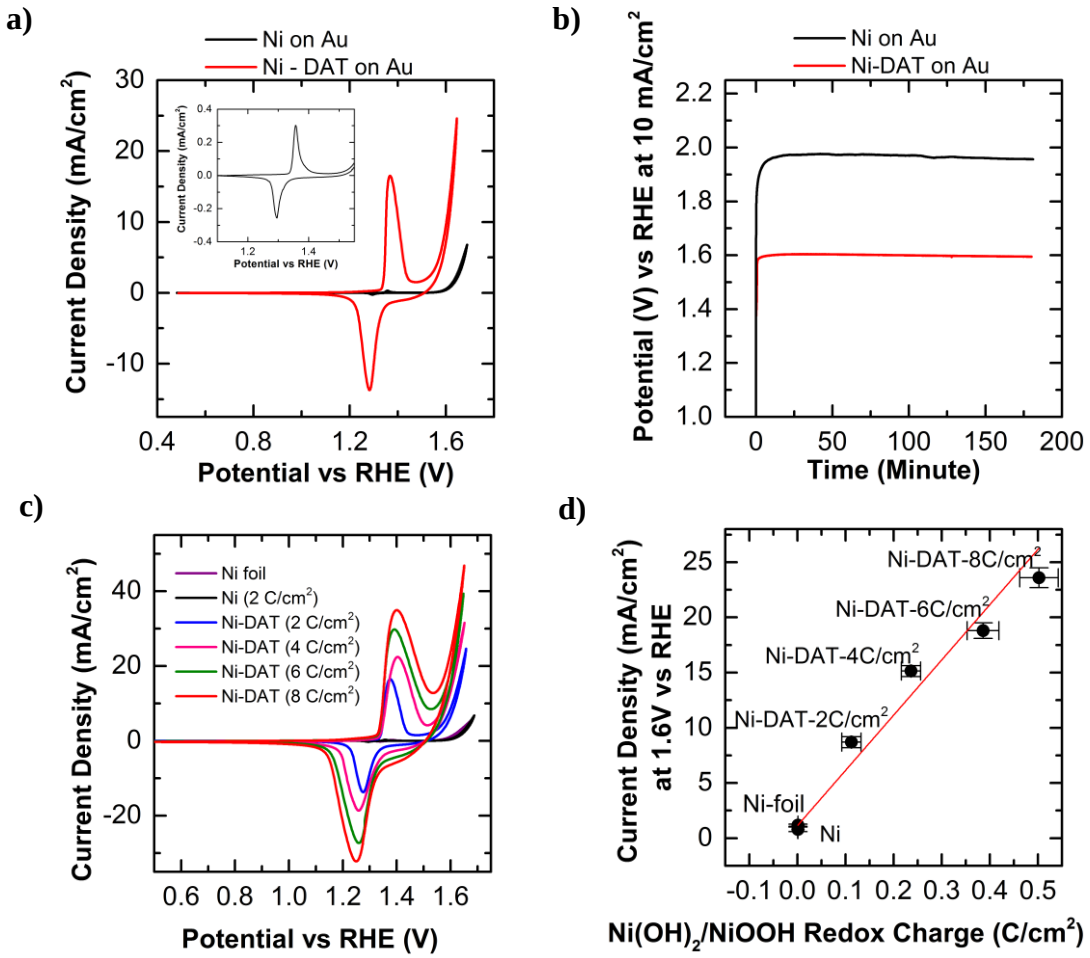

Figure 3.5. a) CV at scan rate 10mV/s (iR corrected); b) Chronopotentiometry (iR corrected) at constant j = 10 mA/cm^2 in 1M NaOH from electrodeposited Ni and Ni-DAT. Inset a) shows the Ni(II)/(III) redox waves of Ni film; c) CV at scan rate 10mV/s (iR corrected) in 1 M NaOH of Ni foil, Ni film on Au, and Ni-DAT film with deposition charge of 2 C/cm^2, 4 C/cm^2, 6 C/cm^2 and 8 C/cm^2; and d) Correlation of current density of OER at 1.6V vs RHE and $Ni(OH)_2$/NiOOH redox charge of Ni-DAT films with different thickness (measured by charge passed during deposition).

The OER occurs above 1.5V for both Ni and Ni-DAT. However, Ni-DAT exhibits a much higher OER current than does the Ni film. The OER current at 1.6 V vs. RHE taken from the CV

(Figure 3.5a) of Ni-DAT is j ~ 10 mA/cm^2, while on Ni, j ~ 1 mA/cm^2. Chronopotentiometry measurements carried out at a constant current of 10 mA/cm^2 (iR corrected) in 1M NaOH (Figure 3.5b) show that the voltage at which the Ni-DAT film can support this current density is 1.60 V while the corresponding voltage for the Ni film alone is > 1.9 V. The figure shows that the film maintains the 1.60 V potential over 180 min of continuous operation, suggesting the Ni-DAT catalyst is very durable.

The integrated current associated with the Ni oxidation peaks shows that ~ 80% of total Ni atoms (the total amount of Ni is quantified by ICP-OES) are electrochemically active. The ratio of oxidation charge and reduction charge ~ 1 for all cycles (even in the 1st cycle), suggests high electrochemical reversibility of the Ni-DAT film, even following extensive OER testing. The TOFs of Ni-DAT are ~ 0.005 s^{-1}, ~ 0.015 s^{-1} and ~ 0.041 s^{-1} at η = 300 mV, 350 mV, and 400 mV, respectively, which are consistent with prior reports examining other Ni nanoparticle catalysts.[14]

We next evaluate the effect of deposition time on the OER rate. Figure 3.5c and 3.5d shows that a Ni film electrodepsited to 2 C/cm^2 (estimated thickness ~ 600 nm), and Ni foil (thickness ~ 0.125 mm) exhibit similar OER activity, indicating that OER activity is independent of Ni film thickness. In contrast, the OER activity of the Ni-DAT film is related to deposition charge, i.e. the amount of Ni electrodeposited. Figure 3.5c and 3.5d shows that as the charge used to deposit Ni-DAT is increased, the $Ni(OH)_2$/NiOOH wave and OER current density also increase.

3.3.3. OER activity of Co films

Co electrodeposited in the presence of DAT (CO-DAT film) yeilds a film which also exhibits a black color. This similarity with the Ni-DAT film may indicate a similar rough surface

structure. Figure 3.6 shows CVs obtained from a Co and a Co-DAT electrode in 1 M NaOH. The 1st oxidation peak (from 0 to 0.4 V vs RHE for Co-DAT, and from 0.2 to 0.6 V vs RHE for Co) is associated to oxidation of Co to $Co(OH)_2$. Reduction of $Co(OH)_2$ back to Co on the cathodic sweep gives a wave much smaller than the associated oxidation peak, suggesting that the reaction is irreversible. The 2nd oxidation wave starting at ca. 0.9 V vs RHE is associated with the oxidation of Co(II) to Co(III) and Co(IV). The OER occurs above 1.5V for both Co and Co-DAT.

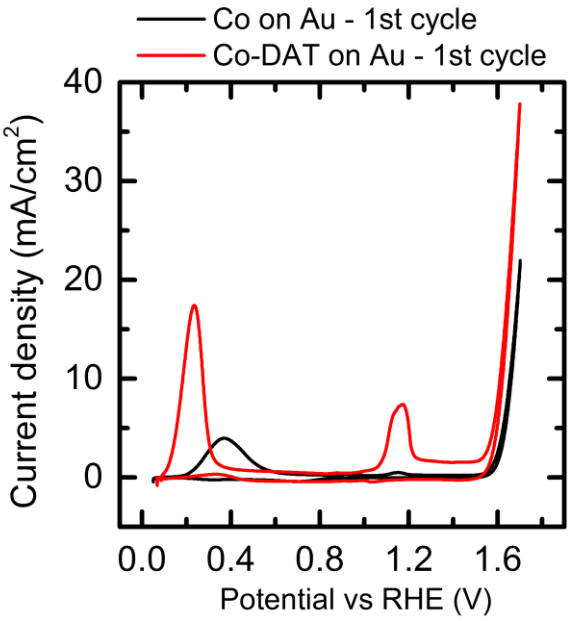

Figure 3.6. CV of the 1st cycle in 1 M NaOH of Co electrodeposited on Au substrate with and without DAT in deposition solution. (scan rate 10mV/s. iR corrected)

The first cycle CV shows that both the oxidation current which ultimately makes CoOOH and the OER current from the Co-DAT film are greater in magnitude than the corresponding waves from the Co film deposited absent DAT. Interestingly, while the oxidation wave starting at ca. 0.9 V is ~ 100 times greater in CoDAT relative to Co, the OER current density at 1.6 V is only ~ 3 times greater, substantially less than the increase found for NiDAT relative to Ni. Additionally, material was observed to flake off of the electrode during the oxidation process. While activity

for Co-DAT was slightly larger on the first scan relative to Co, such was not the case on subsequent scans, likely due to instability of the deposit during oxidation and under OER conditions. In particular, we note that while the Ni-DAT film was found to crack during electrodeposition, such was not the case with Co-DAT. The lack of cracking in the Co-DAT film likely leads to more intrinsic stress upon oxidation, making the film unstable. The higher potential of Co deposition relative to Ni means among other things that there will be less H_2 production for Co relative to Ni. The lower H_2 production could allow the Co-DAT film to be more continuous.

3.3.4. Effect of substrate on Ni-DAT film and OER activity

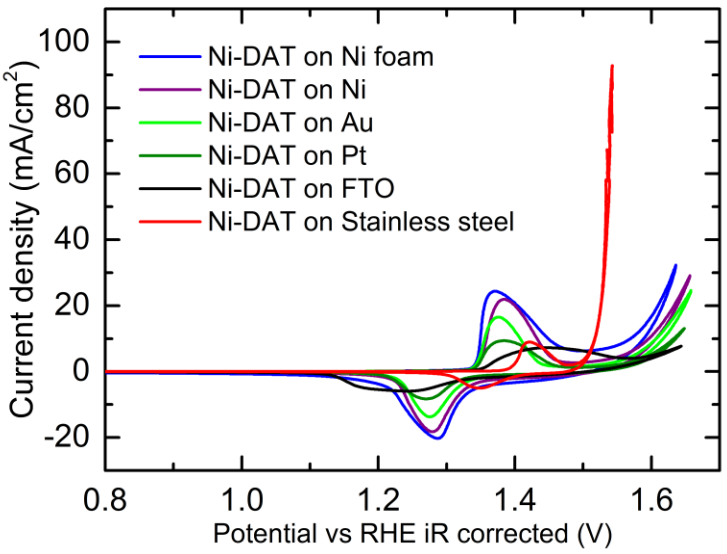

Figure 3.7. CV of Ni-DAT on different substrate in 1 M NaOH at scan rate 10mV/s.

We found that Ni-DAT could be electrodeposited various substrates, including FTO, Pt, Ni foil and Ni foam, in addition to Au. Ni-DAT films on all type of substrates exhibits the black color indicative of rough Ni films. Figure 3.7 shows that activities of Ni-DAT films are somewhat related to the properties of substrate.

Ni-DAT on FTO exhibits a broad oxidation peak, higher OER onset and lower OER current density than those on other substrates due to the lower conductivity of FTO.

Ni-DAT on Pt exhibits a smaller Ni oxidation peak and diminished OER current relative to that on Au because the HER current during Ni-DAT deposition on Pt is higher than that on Au, i.e. the Coulombic efficiency of Ni-DAT on Pt is smaller than that on Au.

Ni-DAT on Ni foil and Ni foam exhibits a higher $Ni(OH)_2$ oxidation current and higher OER current relative to Au likely due to participation of the Ni substrate in the OER process. Ni-DAT on Ni foam shows higher activity than on Ni foil because Ni foam has higher surface area than Ni foil.

Interestingly, Ni-DAT on stainless steel substrate exhibits a very high OER activity, with earlier onset and higher OER current density than Ni-DAT on the other substrates. The origin of this enhancement is associated with exposure of Fe in the stainless steel substrate to the electrolyte, subsequent dissolution of Fe, and its redeposition into the Ni film, which converts the Ni-DAT film into a NiFe-DAT film. We discuss the enhanced activity of NiFe-DAT relative to Ni-DAT in the next sections.

3.3.5. Similar additives to DAT

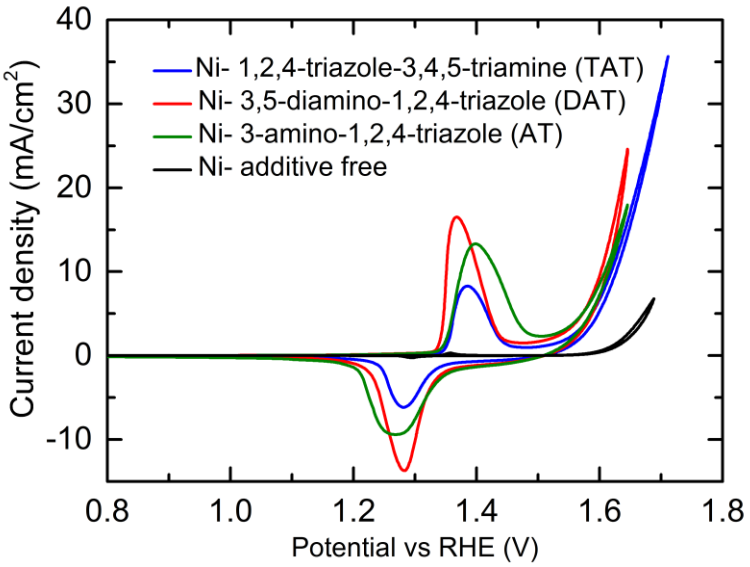

Figure 3.8. CV of Ni electrodes electrodeposited without TAT, DAT, and AT in 1 M NaOH at scan rate 10mV/s, with with iR compensations.

Compounds similar to DAT, such as 3-Amino-1,2,4-triazole (AT), and 1,2,4-triazole-3,4,5-triamine (TAT) also show inhibition activity during Ni electrodeposition and produced black Ni films. However, we found both TAT and AT are weaker inhibitors of Ni electrodeposition relative to DAT, at least under the conditions used in this study (deposition at - 4mA/cm^2, pH 3, room temperature). ~ 4 mM of DAT is required to obtain visible and uniform inhibition (i.e. a black, rough Ni film), while ~ 10 mM of AT and ~ 30 mM of TAT are required to achieve similar results. Figure 3.8 shows CVs obtained from Ni electrodes electrodeposited with DAT (4 mM), AT (10 mM) and TAT (30 mM). All Ni electrodes electrodeposited with additives shows higher Ni(II)/Ni(III) oxidation wave and also exhibit higher OER current density than the Ni electrodeposited without additives.

3.3.6. Electrodeposition and OER activity of NiFe-DAT

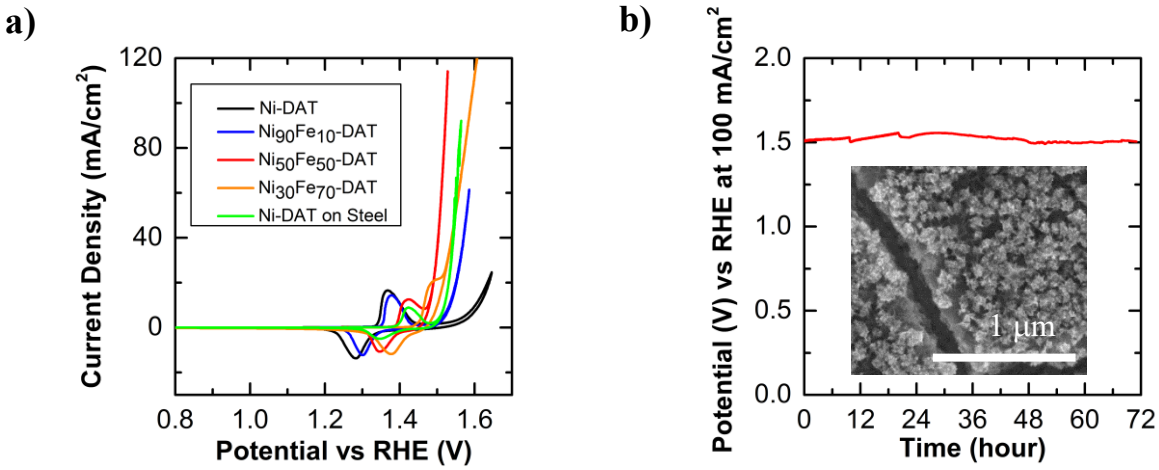

Figure 3.9. a) CV of Ni-DAT, NiFe-DAT films in 1M NaOH at scan rate 10mV/s (iR corrected); b) Chronopotentiometry (iR corrected) at constant j = 100 mA/cm^2 in 1 M NaOH from electrodeposited NiFe-DAT. Inset shows SEM image of a $Ni_{50}Fe_{50}$-DAT film.

Addition of Fe is known to increase the OER activity from Ni films.[9,10,20,26,27] We wondered whether codeposition of Ni and Fe in the presence of DAT (NiFe-DAT) could produce high OER activity materials. Figure 3.9 shows CVs of NiFe-DAT films with varying Ni/Fe ratios (Table 3.1). The CVs for NiFe-DAT films are noticeably different in their $Ni(OH)_2$/NiOOH redox waves and OER activities. As more Fe is incorporated into the NiFe-DAT film, the $Ni(OH)_2$/NiOOH redox couple shifts to higher potentials, consistent with previous reports.[9,10,20] At a Fe content of ~ 70%, the oxidation wave merges with OER current. The shift in the redox potential implies that the electrochemical oxidation of $Ni(OH)_2$ to NiOOH is thermodynamically less favorable in the presence of Fe. The $Ni(OH)_2$/NiOOH redox peak area in the NiFe-DAT film is slightly smaller than that found in the Ni-DAT film. This behaviour is similar to that found with smooth films of NiFe in which the peak area decreases with increases of % Fe. However, small decrease in peak

area of NiFe-DAT film implies that the number of Ni active sites does not vary much with increasing Fe content. This suggests the NiFe-DAT film is very porous.

The OER activity from NiFe-DAT films increases with increasing of Fe content in the film as Fe content varies from 0% to ~ 50%, and then decreases when the Fe content is at 70%. $Ni_{50}Fe_{50}$-DAT exhibits the highest OER activity among the films produced here, giving OER current density of 100 mA/cm^2 at 1.53V (η = 300 mV), which is among the most active OER electrocatalyst in alkaline electrolytes reported so far, to the best of our knowledge. The mass activity of this $Ni_{50}Fe_{50}$-DAT is ~1200 A/g of catalyst at η = 300 mV, which is higher than RuO_2 nanoparticle IrO_2 nanoparticle (range from 20 to 60 A/g at η = 300 mV).[2,6,28] Chronopotentiometry was carried out at a constant j = 100 mA/cm^2 in 1M NaOH. Figure 3.9b shows this current density can be maintained for at least 72 hours at ~ 1.53 V vs RHE.

The integrated current associated with the metal oxidation peaks of NiFe-DAT films shows that ~ 50% of total metal atoms (the total amount of metal is quantified by ICP-OES) are electrochemically active. The TOF from a NiFe-DAT film at η = 300 mV is ~ 0.42 s^{-1}, which is similar to other reports from this type of catalyst.[22,26,29] The correspondence of TOFs indicates that the intrinsic activity of our Ni-DAT and NiFe-DAT catalysts are unchanged relative to other Ni and NiFe catalyst reported previously, but the increased activity we observed originates from the enhancement in surface area of the catalyst film.

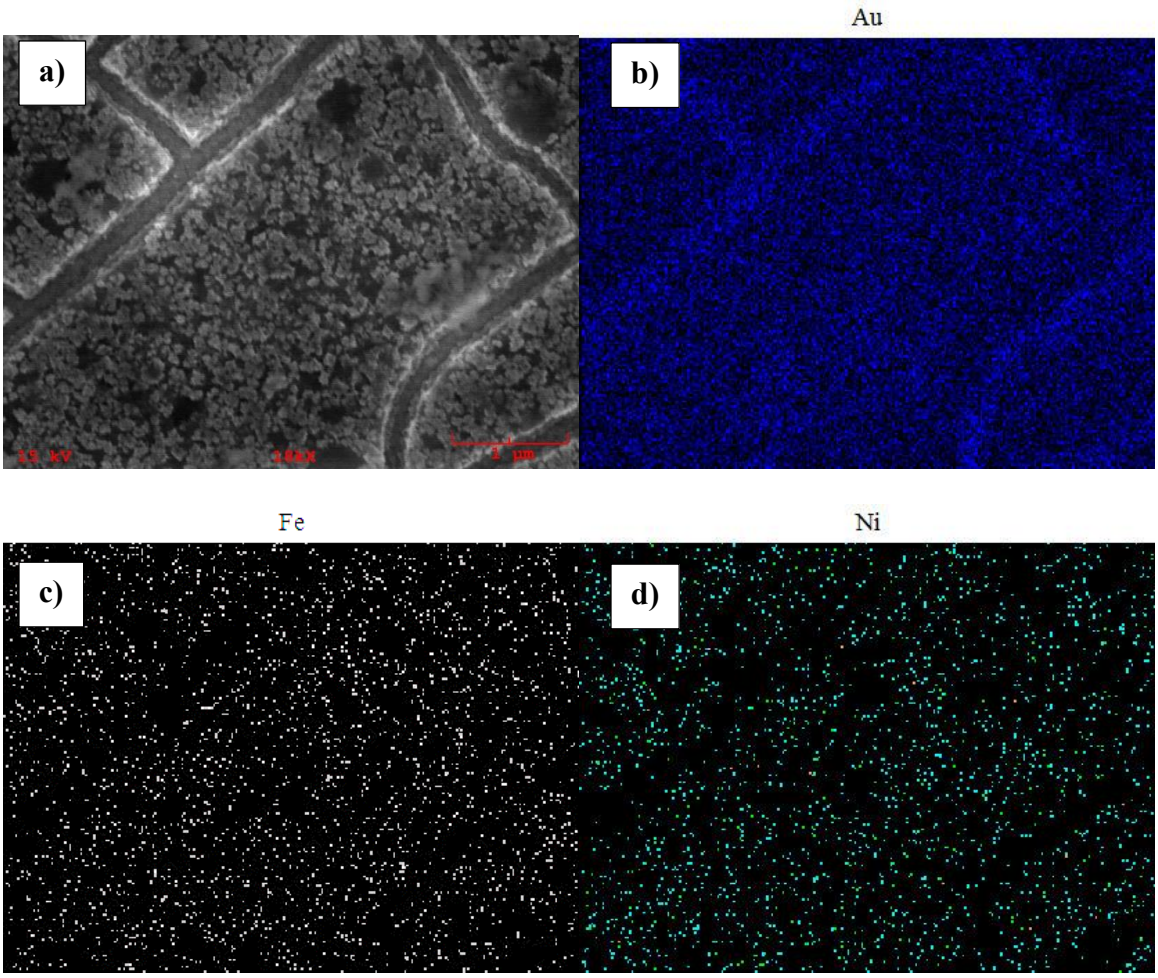

Figure 3.10. SEM and corresponding EDS maps obtained from a $Ni_{50}Fe_{50}$-DAT electrode deposited on Au.

Figure 3.10a shows the presence of a rough, cracked surface as described in section 3.3.1. Figure 3.10b shows the presence of the underlying Au substrate. The EDS obtained from Fe (Figure 3.10c) and Ni (Figure 3.10d) exhibit a good correspondance with the SEM, showing that both Ni and Fe are well-mixed in the deposit.

3.4. Discussion

3.4.1. Ni and NiFe electrodeposition

Conventional additives developed for Ni electrodeposition usually contain aromatic sulphones, or unsaturated groups. Among the most prominent are saccharin, benzene sulfonic acid, coumarin, and picoline, all of which produce smooth and bright Ni deposits. The mechanism by which organic additives modify the electrodeposition process to yield a bright Ni surface involves adsorption of the organic compound and subsequent growth rate alteration on different crystal faces.[30-33]

Some Ni plating additives, such as thiourea,[34] and mixture of sodium naphthalene-2-sulphonate and acrylamide,[35] can produce dull or black Ni deposits exhibiting rough surfaces. The high surface roughness of Ni-DAT and NiFe-DAT is a consequence of both inhibition of electrodeposition by DAT and H_2 adsorption on the electrode surface. Inhibition through DAT and H_2 adsorption on the electrode surface lowers the number of nucleation sites for Ni, each of which however will experience a high local current density. A consequence is the rapid growth of small crystals and development of a rough surface. Similar mechanisms are invoked in a Ag electrodeposition system yielding powdery films.[36] A rough Ni film could also be produced using electrodeposition in the presence of other additives similar to DAT and on different types of substrates (Figure 3.7, 3.8).

3.4.2. Effects of DAT on OER activity

To evaluate whether DAT remain in the deposited films, we conducted XPS measurements on N 1s of Ni samples. Figure 3.4 shows XPS spectra obtained in the N region from Ni and Ni-

DAT films. As-deposited Ni-DAT film exhibits a peak at 399 eV associated with N, which is likely due to DAT retained in or on the Ni deposit. However, after 30 min of OER, there is no detectible N found on the Ni-DAT electrode immersed from solution, which suggests that any retained DAT is oxidized and removed from the electrode during the OER.

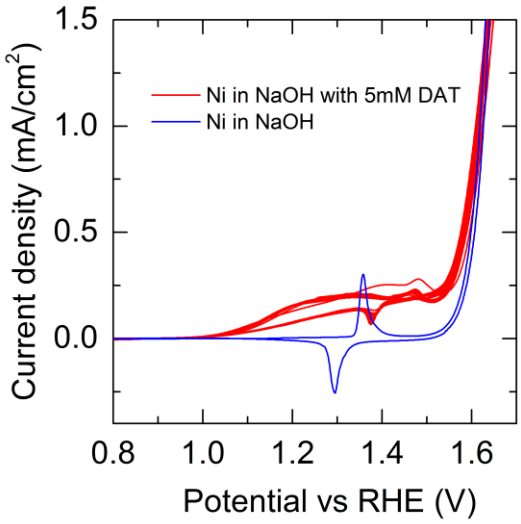

Figure 3.11. a) CV of Ni electrodeposited without DAT in electrolyte of 1M NaOH and 5 mM DAT.

To evaluate whether DAT in the solution could enhance the OER, we tested a Ni film in 1 M NaOH with and without the presence of DAT (5 mM). Figure 3.11 shows a CV of Ni electrodeposited without DAT in electrolyte containing 1M NaOH with and without 5mM DAT. The insets shows that the low potential CV of Ni in 1 M NaOH containing DAT exhibits an oxidation wave between 1.1 and 1.5 V which must be associated with DAT oxidation. Additonally, the voltammetry shows that the presence of DAT moves the $Ni(OH)_2$/NiOOH wave to more positive potentials, showing that further oxidation of Ni is inihibited by this additive. The main CV shows that no enhancement in OER activity was observed with the presence of DAT in the

electrolyte. Thus, both XPS and CV data suggest that DAT has no role in the high OER activity of the Ni-DAT film.

3.4.3. Fractal-like behaviour of Ni-DAT

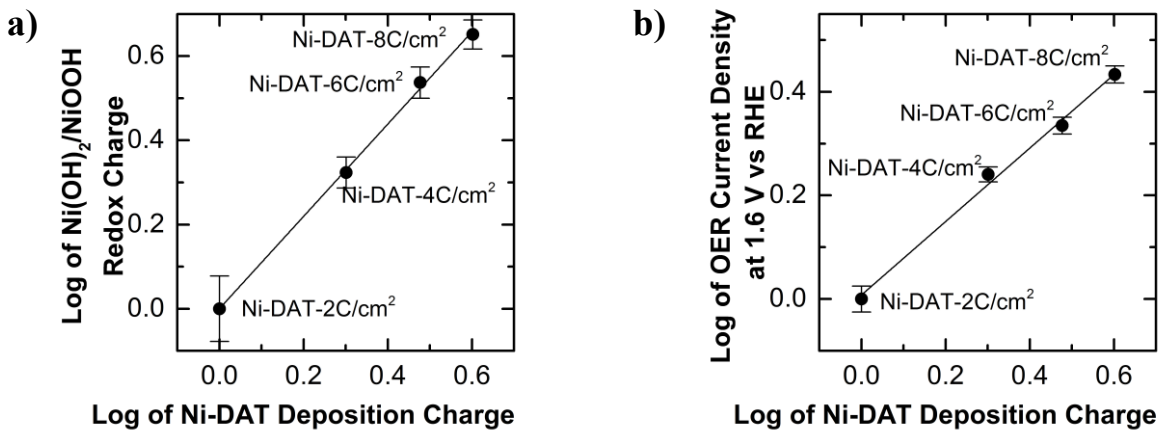

Figure 3.12. Power-law relationship between a) $Ni(OH)_2$/NiOOH redox charge and Ni-DAT deposition charge; and b) OER current density and Ni-DAT deposition charge.

Our results show that by electrodepositing Ni in the presence of DAT we can produce a very active OER catalyst in alkaline passed in forming NiOOH and OER activity, for Ni deposits of different thicknesses (or differing amounts of charge passed during electrodeposition).

Figure 3.12a shows that the redox charge associated with the $Ni(OH)_2$/NiOOH wave increases linearly with increasing charge associated with Ni-DAT deposition; the slope of the log-log graph is 1.10 ± 0.03 ($R^2 = 0.999$). The NiOOH formation wave is a measure of Ni accessibility on the electrodeposited Ni surface, i.e. reports on the number of Ni active sites. The deposition charge represents the number of deposited particles since the deposition efficiency is constant at ~ 14%. Thus, figure 3.12a also shows that Ni-DAT film exhibits a power-law relationship between

the number of active sites and the number of deposited particles. Such behaviour is evidence that the Ni-DAT films exhibit a fractal-like structure.[37,38]

Formation of a fractal-like Ni-DAT deposit could be explained by diffusion-limited aggregation growth in which fractal structures occur when the material accretion onto the surface is limited by diffusion, and deposition occurs preferentially on protuberances.[39-41] High voltage (4 V to 20 V) has been used to reduce diffusion in fractal structure electrodeposition.[42] In our research, DAT binds to substrate surface, initiating roughness, following which these rough areas grow exponentially while other areas on the electrode are still DAT and diffusion inhibited. The deposit acquires fractal character in the presence of DAT even without high voltage.

Figure 3.12b shows that Ni-DAT films also exhibits a power-law relationship between OER activity and deposition charge. In this case, however, the slope is 0.71 ± 0.04 ($R^2 = 0.997$) which is smaller than that of Figure 3.12a. The power law relationship suggest that Ni-DAT films still exhibit a fractal-like structure even during the OER. OER activity is controlled by diffusion of OH^- and O_2 into and out of the porous Ni-DAT films, while $Ni(OH)_2$/NiOOH redox reactions (described above) are controlled by diffusion of H^+ in and out of the film. Slower diffusion of OH^- and O_2 during OER could be the origin of the smaller slope in the power-law graph relating OER activity and deposition charge relative to that relating NiOOH/$Ni(OH)_2$ charge to deposition charge.

3.4.4. NiFe-DAT

We found that the same protocol which produced an OER active Ni film could be translated to the Ni/Fe system. The origin of increased activity in Ni/Fe relative to Ni is thought to be

associated with high OER activity of Fe, where the Ni both inhibits Fe dissolution and enhances the conductivity of Fe hydroxide/oxyhydroxide films.[10,27] In our work, we demonstrate that, as with the Ni case, rougher films give rise to increased activity. However, by increasing the Fe content in the codeposited NiFe film we show that we can increase the OER activity to a very high level. $Ni_{50}Fe_{50}$-DAT exhibits the highest OER activity the films studied here, yielding current densities of 100 mA/cm^2 at 1.53V, which is among the most active OER electrocatalyst in alkaline electrolyte reported to date.

3.5. Conclusion

We developed a simple method to make Ni, Co, and NiFe films exhibiting fractal-like behavior with nano-size clusters by using 3,5-diamino-1,2,4-triazole (DAT) as additive for the metal electrodeposition processes.

NiFe-DAT electrodeposited by this method exhibits very high activity for the OER, stable activity as high as 100 mA/cm^2 (geometric area), mass activity as high as 1200 A/g of catalyst at 1.53 V was found. This activity is among the highest reported for this material or for the OER in base. Equally important, we found that we could in part tune this activity by changing the amount of metal electrodeposited. The effect was essentially independent of substrate. Interestingly, we found that electrodeposition of Ni onto steel produced a NiFe film exhibiting very high activity without any further Fe incorporation. The origin of this high activity is fractal-like behavior i.e film roughness, caused by inhibition of electrodeposition by the DAT additive.

3.6. References

(1) Lewis, N. S.; Nocera, D. G. *P. Natl. Acad. Sci. USA* **2007**, *104*, 20142-20142.

(2) Carmo, M.; Fritz, D. L.; Merge, J.; Stolten, D. *Int. J. Hydrogen Energy* **2013**, *38*, 4901-4934.

(3) Lyons, M. E. G.; Brandon, M. P. *Int. J. Electrochem. Sci.* **2008**, *3*, 1386-1424.

(4) Laguna-Bercero, M. A. *J. Power Sources* **2012**, *203*, 4-16.

(5) Miles, M. H.; Kissel, G.; Lu, P. W. T.; Srinivasan, S. *J. Electrochem. Soc.* **1976**, *123*, 332-336.

(6) Trotochaud, L.; Ranney, J. K.; Williams, K. N.; Boettcher, S. W. *J. Am. Chem. Soc.* **2012**, *134*, 17253-17261.

(7) Lyons, M. E. G.; Brandon, M. P. *J. Electroanal. Chem.* **2010**, *641*, 119-130.

(8) Ayers, K. E.; Anderson, E. B.; Capuano, C. B.; Carter, B. D.; Dalton, L. T.; Hanlon, G.; Manco, J.; Niedzwiecki, M. *Polymer Electrolyte Fuel Cells 10, Pts 1 and 2* **2010**, *33*, 3-15.

(9) Corrigan, D. A. *J. Electrochem. Soc.* **1987**, *134*, 377-384.

(10) Trotochaud, L.; Young, S. L.; Ranney, J. K.; Boettcher, S. W. *J. Am. Chem. Soc.* **2014**, *136*, 6744-6753.

(11) Klaus, S.; Louie, M. W.; Trotochaud, L.; Bell, A. T. *J. Phys. Chem. C* **2015**, *119*, 18303-18316.

(12) Swierk, J. R.; Klaus, S.; Trotochaud, L.; Bell, A. T.; Tilley, T. D. *J. Phys. Chem. C* **2015**, *119*, 19022-19029.

(13) Gong, M.; Li, Y. G.; Wang, H. L.; Liang, Y. Y.; Wu, J. Z.; Zhou, J. G.; Wang, J.; Regier, T.; Wei, F.; Dai, H. J. *J. Am. Chem. Soc.* **2013**, *135*, 8452-8455.

(14) Gao, M. R.; Sheng, W. C.; Zhuang, Z. B.; Fang, Q. R.; Gu, S.; Jiang, J.; Yan, Y. S. *J. Am. Chem. Soc.* **2014**, *136*, 7077-7084.

(15) Esswein, A. J.; McMurdo, M. J.; Ross, P. N.; Bell, A. T.; Tilley, T. D. *J. Phys. Chem. C* **2009**, *113*, 15068-15072.

(16) Lu, X. Y.; Zhao, C. A. *Nat. Commun.* **2015**, *6*, 6616.

(17) Wendt, H.; Plzak, V. *Electrochim. Acta* **1983**, *28*, 27-34.

(18) Balej, J.; Divisek, J.; Schmitz, H.; Mergel, J. *J. Appl. Electrochem.* **1992**, *22*, 705-710.

(19) Hall, D. E. *J. Electrochem. Soc.* **1983**, *130*, 317-321.

(20) Li, X. H.; Walsh, F. C.; Pletcher, D. *Phys. Chem. Chem. Phys.* **2011**, *13*, 1162-1167.

(21) Walcarius, A.; Mandler, D.; Cox, J. A.; Collinson, M.; Lev, O. *J. Mater. Chem.* **2005**, *15*, 3663-3689.

(22) Batchellor, A. S.; Boettcher, S. W. *ACS Catal.* **2015**, *5*, 6680-6689.

(23) Pourbaix, M. *Atlas of electrochemical equilibria in aqueous solutions*; 2nd English ed.; National Association of Corrosion Engineers: Houston, Tex., 1974.

(24) Medway, S. L.; Lucas, C. A.; Kowal, A.; Nichols, R. J.; Johnson, D. *J. Electroanal. Chem.* **2006**, *587*, 172-181.

(25) Hoang, T. T. H.; Cohen, Y.; Gewirth, A. A. *Anal. Chem.* **2014**, *86*, 11290-11297.

(26) Louie, M. W.; Bell, A. T. *J. Am. Chem. Soc.* **2013**, *135*, 12329-12337.

(27) Friebel, D.; Louie, M. W.; Bajdich, M.; Sanwald, K. E.; Cai, Y.; Wise, A. M.; Cheng, M. J.; Sokaras, D.; Weng, T. C.; Alonso-Mori, R.; Davis, R. C.; Bargar, J. R.; Norskov, J. K.; Nilsson, A.; Bell, A. T. *J. Am. Chem. Soc.* **2015**, *137*, 1305-1313.

(28) Lee, Y.; Suntivich, J.; May, K. J.; Perry, E. E.; Shao-Horn, Y. *J. Phys. Chem. Lett.* **2012**, *3*, 399-404.

(29) Hunter, B. M.; Blakemore, J. D.; Deimund, M.; Gray, H. B.; Winkler, J. R.; Muller, A. M. *J. Am. Chem. Soc.* **2014**, *136*, 13118-13121.

(30) Schlesinger, M.; Paunovic, M. *Modern electroplating*; 5th ed.; Wiley: Hoboken, NJ, 2010.

(31) Amblard, J.; Epelboin, I.; Froment, M.; Maurin, G. *J. Appl. Electrochem.* **1979**, *9*, 233-242.

(32) Costavar.Ta; Froment, M.; Goff, A. H. L.; Georgoul.C *J. Electrochem. Soc.* **1973**, *120*, 867-874.

(33) Szeptycka, B. *Russ. J. Electrochem.* **2001**, *37*, 684-689.

(34) Mohanty, U. S.; Tripathy, B. C.; Das, S. C.; Misra, V. N. *Metall. Mater. Trans. B* **2005**, *36*, 737-741.

(35) Nayak, B.; Karunakaran, K. *J. Appl. Electrochem.* **1982**, *12*, 323-328.

(36) Makino, T.; Aogaki, R.; Niki, E. *J. Chem. Phys.* **1984**, *81*, 5145-5150.

(37) Sagues, F.; Costa, J. M. *J. Chem. Educ.* **1989**, *66*, 502-506.

(38) Russ, J. C. *Fractal surfaces*; Plenum Press New York 1994.

(39) Godorr, S. A.; Young, B. D.; Bryson, A. W. *Chem. Eng. Commun.* **1992**, *117*, 307-335.

(40) Voss, R. F.; Tomkiewicz, M. *J. Electrochem. Soc.* **1985**, *132*, 371-375.

(41) Sander, L. M. *Contemp. Phys.* **2000**, *41*, 203-218.

(42) Trigueros, P. P.; Claret, J.; Mas, F.; Sagues, F. *J. Electroanal. Chem.* **1991**, *312*, 219-235.

Chapter 4

Observation of an Inverse Kinetic Isotope Effect in Oxygen Evolution Electrochemistry

4.1. Introduction

Redox reactions involving multiple proton-coupled electron transfer (PCET) steps are ubiquitous and have gathered a significant amount of interest toward understanding biological systems and developing alternative energy conversion schemes over the past decades.[1-9] Using renewable sources of energy to power water-splitting electrolyzers offers a promising system to generate H_2 with almost no carbon footprint.[10-12] An electrolyzer is an energy conversion device that splits water into H_2 and O_2 via the following two half-cell reactions: the cathodic hydrogen evolution reaction (HER, $2H^+ + 2e^- \rightarrow H_2$) and the anodic oxygen evolution reaction (OER, $4OH^- \rightarrow 2H_2O + 4e^- + O_2$),[13] also known as the water oxidation reaction.[14] The performance of an electrolyzer is not limited by the reaction involving hydrogen,[13,15-17] but is limited by the sluggish kinetics of the reaction involving oxygen which requires a large OER overpotential at the anode.[18,19] Ir and Ru are the anodes of choice in acidic electrolyte with low OER overpotentials.[20] However, the widespread application of Ir/Ru-based anodes is hindered by the prohibitive high cost and poor long-term stability of these precious metal catalysts. Ni, Co, and their alloys are attractive electrocatalysts for OER in alkaline electrolyte, because these relatively inexpensive non-precious metal (NPM) materials are abundant and durable in basic conditions.[21-23] However, OER overpotentials using Ni/Co-based materials range from ca. 300 to 400 mV relative to the

thermodynamic potential of 1.23 V versus RHE.[10,24] Real-world thermodynamic efficiencies for water splitting are only ~75% with currently available Ni-based catalysts.[10] However, catalyst design to eliminate the high OER overpotential is still limited because insight into the OER mechanism is missing.[22]

Currently, tremendous effort is invested to elucidate the identity and surface structure of the bulk anode materials used to facilitate the OER.[23,25] Reports suggest that surface oxides and oxyhydroxides, which are formed on the metal prior to the OER, are the active catalytic species.[26] Compositional and morphological changes upon redox cycling of these porous thin film OER catalysts have been investigated using various techniques, including but not limited to voltammetric studies,[20,27-29] Raman spectroscopy,[30-33] X-ray photoelectron spectroscopy (XPS),[34-37] X-ray diffraction (XRD),[38,39] X-ray absorption spectroscopy (XAS),[40-42] scanning electron microscopy (SEM) and transmission electron microscopy (TEM),[39,43] scanning tunneling microscopy (STM),[44] ellipsometry,[45,46] atomic force microscopy (AFM),[47,48] electrochemical quartz crystal microbalance (EQCM),[49-52] and *in situ* stress measurement.[53] EQCM experiments corroborate that the catalyst film does not dissolve during electrocatalysis and remains stable in basic conditions.[54] Despite the extensive effort expended in these areas,[55] a complete understanding of the reaction mechanism has not been achieved.

In order to understand the OER mechanism on oxidized metals, it is important to interrogate the OER process at the molecular level. Density functional theory (DFT) calculations predicted that the binding energy of surface oxygen species such as *O, *OH, *OOH controls the OER activity.[11,22,26] However, the use of computational methods to interrogate the kinetics of heterogeneous catalytic systems is extremely challenging,[9,54,56] and the explicit role of protons in OER remains poorly understood. The use of the kinetic isotope effect (KIE) is an established

experimental technique to study chemical reactions involving protons.[57,58] Specifically, the substitution of hydrogen with deuterium has been carried out extensively due to the large differences in reaction rates arising from the reduced mass differences between the isotopes.[59,60] For electrocatalysis involving protons, Conway et al. investigated KIE of the HER catalyzed by Pt, and Yeager et al. conducted a similar KIE study on oxygen reduction reaction catalyzed by Pt.[61-64] For OER, only several systems involving precious metals have been reported.[28,65-67] ^{18}O labeling experiments were performed on Ni and other metal surfaces to rule out soluble hydrated metal species as the active catalyst material.[68] Therefore, we seek to expand the use of KIE studies to further understand the OER on NPM catalysts at the molecular level.

Here, we launched comprehensive and comparative KIE studies of several precious and NPM OER catalysts to gain direct mechanistic insight into these intricate reactions involving multiple PCET steps. In particular, we interrogated the difference in OER response of NPM OER catalysts in the condition at which they are stable and active. We envision these results to provide unique information that will allow the development of next-generation, high-performance, durable, and affordable OER catalysts for practical energy conversion devices under operation conditions in the near future.

4.2. Experimental section

Chemicals were obtained from commercial sources and used without further purification unless otherwise specified. All proteo and deutero aqueous solutions were prepared freshly each day using Milli-Q water (> 18 MΩ cm) and D_2O, respectively. NaOH (1 M) and NaOD (1 M) solutions were used as electrolytes to maintain a sufficiently high ionic conductivity for accurate

electrochemical measurements and subsequent analyses.[69] Solutions were sparged with Ar, which was dried using a drying tube, for 30 min prior to each experiment.

Electrochemical studies were carried out using a CH Instruments 760 D Electrochemical Workstation (Austin, TX) at room temperature (24 °C to 26 °C). OER experiments were performed in a sealed cell with a Pt mesh counter electrode and a "no leak" Ag/AgCl reference electrode. Electrochemical impedance spectra (EIS) for iR correction were collected using a SP-150 potentiostat (Bio-Logic). The resistance, R, was typically ca. 3 Ω, and iR correction was done following published procedures.[69-71] Unless otherwise stated, the scan rate was 10 mV s^{-1}. The measured potential by the Ag/AgCl reference electrode did not shift in proteo and deutero solutions, as confirmed by the peak position of the Fe(II/III) wave of $K_3Fe(CN)_6$.[72,73] Electrochemical potentials are reported relative to the reversible hydrogen electrode (RHE), the value of which was measured by sparging the solution with H_2 (1 atm) and monitoring the open circuit potential between the Ag/AgCl reference and a Pt wire introduced following the measurement.[74,75] All experiments performed were at least quadruplicated. Voltammograms shown are from representative trials. Error bars presented represent standard deviations of all trials.

For cyclic voltammetry studies, Ni films (~ 300 nm) were electrodeposited onto Au substrates in an aqueous bath of $NiSO_4$ (0.5 M) and H_3BO_3 (0.4 M) adjusted to pH 3 using H_2SO_4 using a pulse deposition method: held at −4 mA cm^{-2} for 100 s followed by 10 s of resting time, and repeated for two more times.[53] For studies in deutero solutions, the bath was prepared using D_3BO_3 (0.4 M) in D_2O and adjusted to pD 3 using D_2SO_4. Co films (~ 300 nm) were prepared in an analogous manner using $CoSO_4$ (0.5 M) instead. Au substrates were fabricated from glass microscope coverslips (Gold Seal No. 1, 150 μm thick) modified on one side by electron beam deposition of 20 nm Ti followed by 200 nm Au. The geometric areas of the electrodes were

typically ca. 1 cm^2. The Au electrodes were annealed for ca. 1 min using a H_2 flame to clean the Au surfaces prior to use.[27,53,76,77]

Rotating ring-disk electrode (RRDE) experiments were performed using a ring-disk assembly with an interchangeable disk (E5 series, Pine instruments) connected to a MSRX rotator (Pine Instruments). A Au disk electrode (A = 0.196 cm^2) was polished sequentially with 0.25μm and 0.05 μm diameter diamond polish (Buehler), and sonicated in water after each polishing step. A Ni film was electrodeposited onto the Au disk electrode in a manner analogous to the procedure described above. The Pt ring electrode (Pine Instruments) was cleaned electrochemically by cycling from −0.4 V to +1.7 V vs. Ag/AgCl reference at 100 mV/s in an aqueous solution of $HClO_4$ (0.1 M) until the oxide stripping feature at ∼+0.35 V vs. Ag/AgCl reference remained constant.[74,75]

Raman Studies were performed using a polycrystalline Au disk working electrode which was sequentially polished using 9 μm, 3 μm, 1 μm, 0.25 μm, and 0.05 μm diamond suspensions to a mirror finish. After each 5-min polishing step, the electrode was sonicated in Milli-Q water for 5 min and thoroughly rinsed. The Au disk was flamed using a H_2 torch for ca. 1 min and quenched in Milli-Q water. The flamed Au electrode was then electrochemically roughened in a cell consisting of an aqueous Ag/AgCl reference electrode, a Au counter electrode, and a KCl (0.5 M) electrolyte by cycling between −0.25 V and +1.3 V vs. Ag/AgCl for 50 roughening cycles as previously described.[76,77] For deuterated studies, the flamed Au disk was quenched in D_2O and electrochemically roughened in D_2O containing KCl (0.5 M). Electrodeposition of metal thin films was performed as described above with the exception that a current density of −3 mA cm^{-2} was held for 40 s.

In situ surface-enhanced Raman spectroscopy (SERS) measurements were conducted using a spectroelectrochemical cell described previously.[78] A He–Ne laser (50 mW, 632.8 nm,

Meredith Instruments) was utilized to provide sample excitation at an incident angle of approximately 45° relative to an 85 mm f/1.2 collection lens (Canon). The scattered radiation was then focused using an f/1.2 lens to the 10 μm slit of a SpectraPro 2300i monochromator (Princeton Instruments) with grating of 1200 grooves per mm. The estimated spectral resolution was 2-3 cm^{-1}. The CCD detector (Andor) was thermoelectrically cooled to −80 °C. Acquisition time for the spectra reported was 30 s.

Calculating kinetic isotope effect from Tafel slope analysis.[1]

$$overpotential = \eta = \frac{R\,T}{\alpha\, n_a\, F}\ln j_0 - \frac{R\,T}{\alpha\, n_a\, F}\ln j$$

where R = ideal gas constant, T = temperature, α = transfer coefficient, n_a = number of electrons transferred during the rate-determining step, F = Faraday's constant, and j = current density. Plotting $y = \eta$ and $x = \ln j$ gives:

$$slope = -\frac{R\,T}{\alpha\, n_a\, F}$$

$$intercept = \frac{R\,T}{\alpha\, n_a\, F}\ln j_0$$

$$intercept = (-slope)\ln j_0$$

$$j_0 = e^{\frac{intercept}{-slope}}$$

Exchange current density (j_0) is described by the following equation:[2]

$$j_0 = nFk_0C^*$$

where n = total number of electrons transferred, k_0 = standard heterogeneous rate constant, and C^* = bulk concentration of species.

Dividing j_0^H obtained in proteo solution by j_0^D obtained in deutero solution gives:

$$\frac{j_0^H}{j_0^D} = \frac{n^H k_0^H C^{*,H}}{n^D k_0^D C^{*,D}}$$

$C^{*,H} = C^{*,D}$ because the experiments were conducted in pH 14 and pD 14 solutions, i.e. the hydroxide and deuteroxide concentrations are the same.

Assuming n remains unchanged in proteo and deutero solutions:

$$\frac{j_0^H}{j_0^D} = \frac{k_0^H}{k_0^D}$$

Using Tafel slope analysis to calculate kinetic isotope effect is not meaningful at high overpotential because the reaction is limited by mass transport. Therefore, to obtain meaningful interpretation of the kinetic isotope effect of OER catalyzed by Ni and Co, we utilize Tafel slope analysis at overpotentials less than 0.5 V where the reaction is not limited by mass transport.[3]

To maintain consistency in Tafel slope analysis, Tafel slopes are obtained in the same potential window for both proteo and deutero solutions where the second derivatives of the CV traces are zero. The Tafel slopes measured for proteo solutions at both low and high overpotentials match with literature reported values. Recent Tafel slope values for the OER on Ni at high overpotential range from 126 to 132 mV dec^{-1}.[4] However, we focus our attention to the low overpotential region where the kinetics of the reaction is not plagued by mass diffusion from bulk solution to the electrode surface then through the layered-structure of the metal oxides/oxyhydroxides/hydroxides.

For porous thin films with complex layered structures, interlayer water diffusion is expected to be much slower. In fact, the diffusion coefficient of water in confined spaces such as those found in artificial membranes (like Nafion and ionomers) and natural channels (like cellulose membranes) is at least an order of magnitude lower than the self-diffusion coefficient of bulk water.[5-8] The significant smaller diffusion coefficient is explained by the strong first solvation shell

hydrogen-bonding interaction with surface species,[9,10] a scenario similar to the porous structure featured in Ni and Co oxyhydroxide thin films.

4.3. Results and discussion

4.3.1. Electrodeposited Ni OER catalysts in proteo and deutero solutions

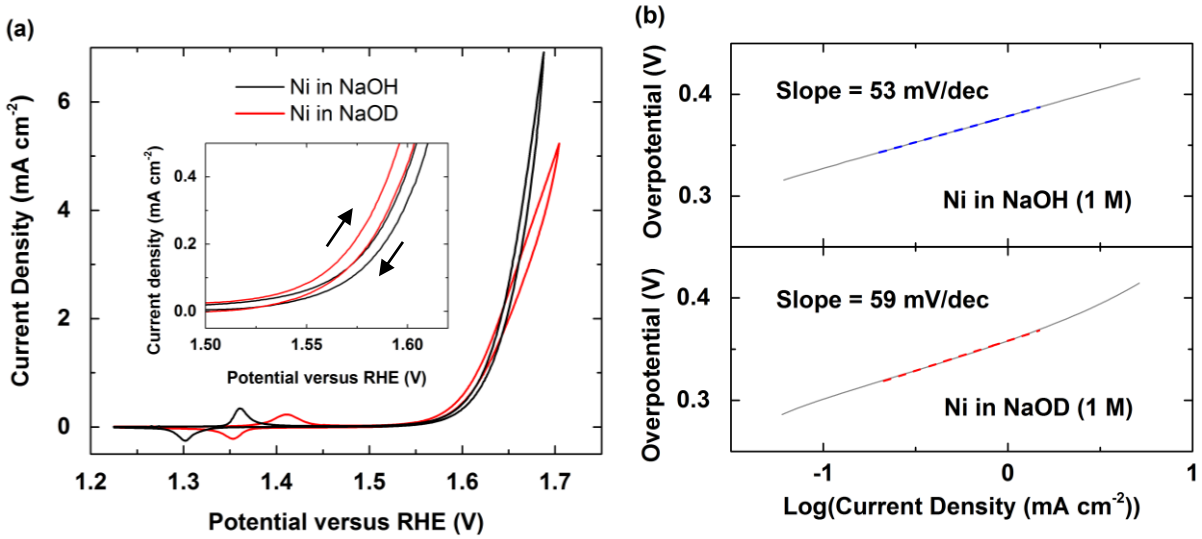

Figure 4.1. (a) IR-corrected CVs of Ni in NaOH (1 M) and NaOD (1 M) solutions. Inset displays the OER onset region. (b) Tafel plots of Ni in (top) 1 M NaOH and (bottom) 1 M NaOD solutions.

To investigate the effect of protons on the OER, we utilized Au electrodes as a platform to study the KIE both electrochemically and spectroscopically. The well-established Au system exhibits a normal KIE during OER by inspection of reported voltammograms,[79] and a corresponding redshift of the potential-dependent Au-OH band using *in situ* surface-enhanced Raman spectroscopy (SERS) upon deuteration.[80] Leveraging the stability and the SERS capability of Au surfaces, we examined transition metal films electrochemically deposited on Au. First, we consider the Ni film on Au system. Figure 4.1a shows cyclic voltammograms (CVs) obtained from

Ni in basic proteo and deutero solutions starting with the anodic sweep. Similar to previous reports in alkaline solutions,[12,81,82] Ni metal is spontaneously oxidized to Ni(II) hydroxide upon immersion,[38,83] and is then further oxidized to generate Ni(III) oxyhydroxide at 1.362 V. At 1.600 V, the electrodeposited Ni electrode delivers an OER current density of 0.5 mA cm^{-2}.

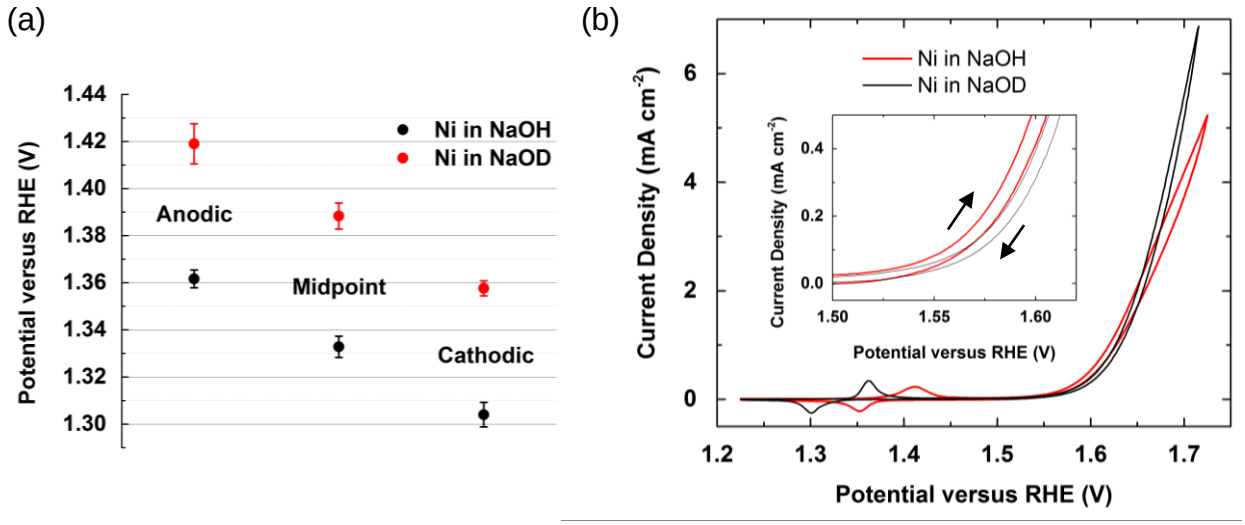

Figure 4.2. (a) Anodic, cathodic, and midpoint potentials of the $Ni(OH)_2$/NiOOH wave in 1 M NaOH (black) and 1 M NaOD (red). (b) IR-uncorrected CVs of Ni in NaOH (1 M) and NaOD (1 M) solutions. Inset displays the OER onset region.

The black line in Figure 4.1a displays the $Ni(OH)_2$/NiOOH redox wave with a midpoint potential ($E_{1/2}$) of 1.333 V. The red line displays the $Ni(OD)_2$/NiOOD redox wave with a $E_{1/2}$ of 1.388 V. The position of the redox wave in deutero solution is ca. 55 mV more positive than that obtained in proteo solution, indicating that the oxidation of $Ni(OD)_2$ to NiOOD is thermodynamically more difficult than the oxidation of $Ni(OH)_2$ to NiOOH.

Figure 4.2a summarizes anodic, cathodic and midpoint potentials of the Ni(II/III) redox wave. Without iR-correction (Figure 4.2b, we observe more OER current in proteo solution than deutero solution at potentials greater than 1.66 V for the case of Ni, likely because the diffusion

coefficient of H_2O is larger than that of D_2O.[14,15] At potentials lower than 1.66 V, OER occurs at a slower rate and the interlayer $H(D)_2O$ inside the NiOOH(D) film is preferentially oxidized. At high potentials, interlayer $H(D)_2O$ is depleted and the gaps are replenished by bulk $H(D)_2O$. This bulk-to-interlayer diffusion process of $H(D)_2O$ likely limits the OER rates. We note that Co exhibits the same crossing behavior as Ni (*vide infra*), suggesting that this feature is likely not dependent on the identity of the OER catalysts, but rather a general phenomenon when running experiments in and comparing results between proteo and deutero solutions.

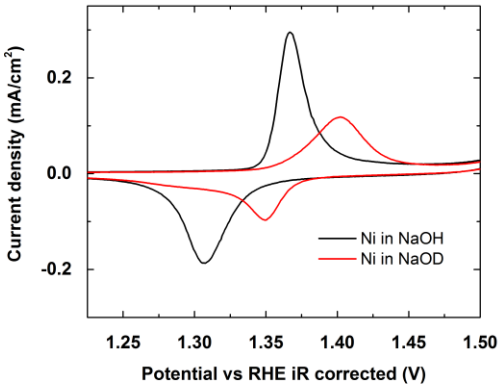

Figure 4.3. CVs of Ni foil in 1 M NaOH (black) and 1 M NaOD (red) solutions.

To confirm the shift in the Ni(II/III) wave upon deuteration, we carried out similar experiments using Ni foil in proteo and deutero solutions and observed a 40 mV positive shift in deutero solution similar to the case using electrodeposited Ni (Figure 4.3). We note that these shifts in potential are not due to reference electrode effects, as confirmed by experiments with $K_3Fe(CN)_6$ which demonstrated identical potentials for the Fe(II/III) wave in both proteo and deutero media.[72] The difference in current observed in Figure 4.3 could be due to many reasons, one of which could be the difference in surface roughness of the Ni foil used. The Ni foil was polished with sand paper and dipped into H_2SO_4 or D_2SO_4 to expose fresh Ni surfaces prior to electrochemical studies, so

the geometric area used to calculate current density does not reflect the actual electrochemical active surface area. We would like to stress that the point of this experiment is to check whether the Ni(II/III) peak shifts depending on the bulk solution content—in particular H versus D. This experiment clearly demonstrates that the Ni(II/III) peak in deutero solution is more positive than the case in proteo solution.

Similar positive potential shifts upon deuteration have been observed for a variety of cationic transition metal complexes and are explained in two ways.[72,84,85] First, because the O-D bond is stronger than the O-H bond,[86] breaking the O-D bond is energetically more costly and the anodic wave shifts positive. Second, Ni(III) has a tighter solvation shell than Ni(II) and D_2O forms a stronger deuterium bonding network relative to the hydrogen bonding network of H_2O.[73] Therefore, there is a greater increase in entropy when the deuterated solvent structure relaxes during the reduction of Ni(III) to Ni(II).[84] Due to the more favorable change in entropy that occurs upon reducing Ni(III) to Ni(II) in deutero solutions, the cathodic wave shifts positive. Since both the anodic and cathodic waves shift positive, the $E_{1/2}$ shifts positive accordingly.

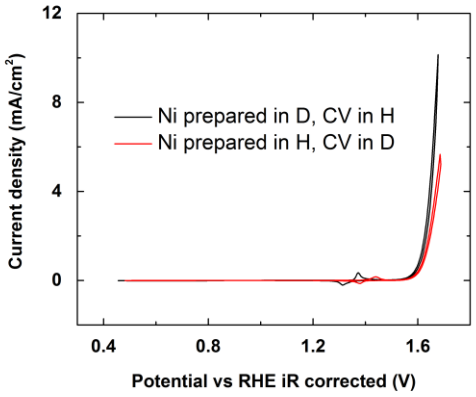

Figure 4.4. CVs of Ni prepared in proteo solution and ran CVs in NaOD (1 M) solution and prepared in deutero solution and ran in NaOH (1 M) solution.

Figure 4.4 shows the CVs of Ni prepared in proteo solution and interrogated in deutero solution and CVs of Ni prepared in deutero solution and interrogated in proteo solutions. The CVs show that Ni metal film prepared in H solution and interrogated in D solution exhibit a Ni(II/III) redox wave more positive than that found using a Ni metal film prepared in D solution and interrogated in H solution. This result confirms that the shift in redox potential does not depend on the solution in which the film is prepared. Instead, the shift depends upon the solution in which the voltammetry is recorded, a condition analogous to the case presented in Figure 4.1. This "cross" experiment further demonstrates that preparing Ni metal film in H and D solution does not leave a detectable trace amount of H or D residual in the electrodeposited film. Therefore, pulse deposition of Ni in pH- or pD-controlled solution likely leads to electrodeposits consisting of pure Ni metal films absent hydroxide, deuteroxide, oxyhydroxide, and/or oxydeuteroxide contamination.

The inset to Figure 4.1a shows a blowup of the OER onset region in both proteo and deutero solutions. Interestingly, the inset shows that the OER in D_2O exhibits a more negative onset and a lower overpotential at 0.5 mA cm^{-2} relative to the same system in H_2O. Figure 4.1b shows the Tafel slopes of OER catalyzed by Ni in proteo and deutero basic solutions. The Tafel slope found in NaOD at the low overpotential region (where η ranges between 0.3 and 0.4 V) is 59 mV dec^{-1} (Figure 4.1b, top), a value that is somewhat greater than the corresponding slope (53 mV dec^{-1}) found in NaOH (Figure 4.1b, bottom). Recent Tafel slope values for the OER in NaOH on Ni at the low overpotential range from 51 to 54 mV dec^{-1}.[87] At higher overpotentials, the NaOH and NaOD OER traces cross at 1.65 V versus RHE, likely due to the faster interlayer diffusion rate of H_2O relative to D_2O in between the confined structure of the electrochemically deposited metal thin films during OER.[88,89] The contribution of differential diffusion rates at low overpotential is

insignificant because there are enough reactants between the oxide layers when the rate of OER is low. Therefore, for the KIE analysis, we focus at the low overpotential region where the kinetics of the reaction are not dominated by the diffusion of reactants from the bulk solution to the catalytic sites located inside the layered structure of the complex metal electrocatalysts.

Table 4.1. Summary of the overpotential at 0.5 mA cm^{-2}, Tafel slope and kinetic isotope effect of OER catalyzed by Ni and Co in 1 M NaOH and 1 M NaOD solutions.

Condition	**Overpotential at 0.5 mA cm^{-2} (V)**	**Tafel Slope (mV dec^{-1})**	**k_H/k_D**
Ni in 1 M NaOH	0.370 ± 0.006	53 ± 1	
			0.6 ± 0.1
Ni in 1 M NaOD	0.337 ± 0.006	59 ± 1	
Co in 1 M NaOH	0.330 ± 0.007	57 ± 1	
			0.5 ± 0.1
Co in 1 M NaOD	0.285 ± 0.002	63 ± 1	

Tafel analysis is a widely accepted technique to interrogate the intrinsic kinetic parameters of electrocatalytic processes.[90] Table 1 lists the OER activity of Ni found in Figure 4.1a, the OER Tafel slope obtained at the low overpotential region from Tafel analysis (Figure 4.1b), and k_H/k_D of Ni in proteo and deutero solutions. The KIE of OER was determined from the voltammograms using the Tafel equation:

$$\eta = \frac{R\,T}{\alpha\, n_a\, F} ln\, j_0 - \frac{R\,T}{\alpha\, n_a\, F} ln\, j$$

$$j_0 = nFk_0C^*$$

where η = overpotential, R = ideal das constant, T = temperature, α = transfer coefficient, n_a = number of electrons transferred during the rate-determining step, F = Faraday's constant, j_0 = exchange current density, j = current density, n = total number of electrons transferred, k_0 = standard heterogeneous rate constant, and C^* = bulk concentration of species. Using the Tafel slopes found, the calculated KIE is 0.6. A k_H/k_D value of below 1 is indicative of an inverse KIE.[59,60,91]

4.3.2. Electrodeposited Co OER catalysts in proteo and deutero solutions

To test the generality of the inverse KIE in alkaline OER catalysis, we next evaluate the effect of deuteration on the OER on Co electrodes. Figures 4.5a-d display the iR-corrected CVs of Co obtained in basic proteo and deutero solutions and Figures S4a-d shows the corresponding uncorrected data. Our Co OER results match with previous reports.[30] Figure 4.5c compares the anodic peak positions of the Co(II/III) wave in proteo and deutero basic solutions. Comparing to the Ni case (*vide supra*), the Co(II/III) anodic peak in 1 M NaOD is at 0.987 V versus RHE, which is slightly more positive relative to that found in 1 M NaOH (0.978 V versus RHE). The difference between the OER current densities measured at high overpotential between proteo and deutero solutions found for Co is less apparent as compared to the Ni case. Although Ni and Co exhibit the same qualitative trends, the dissimilarities in the magnitude observed is likely due to the fact that Co forms multiple types of oxides and hydroxides before and during OER,[19] while Ni only forms $Ni(OH)_2$ and NiOOH in alkaline conditions.[23] Table 4.1 lists the OER overpotentials of Co at 0.5 mA cm^{-2} obtained in proteo and deutero basic solutions, which are similar to those found using Ni as the OER catalyst. Figure 4.6 shows the Tafel plots of Co at the low overpotential

region. The calculated KIE is about 0.5 (Table 4.1), which is similar to the KIE value found for the Ni case.

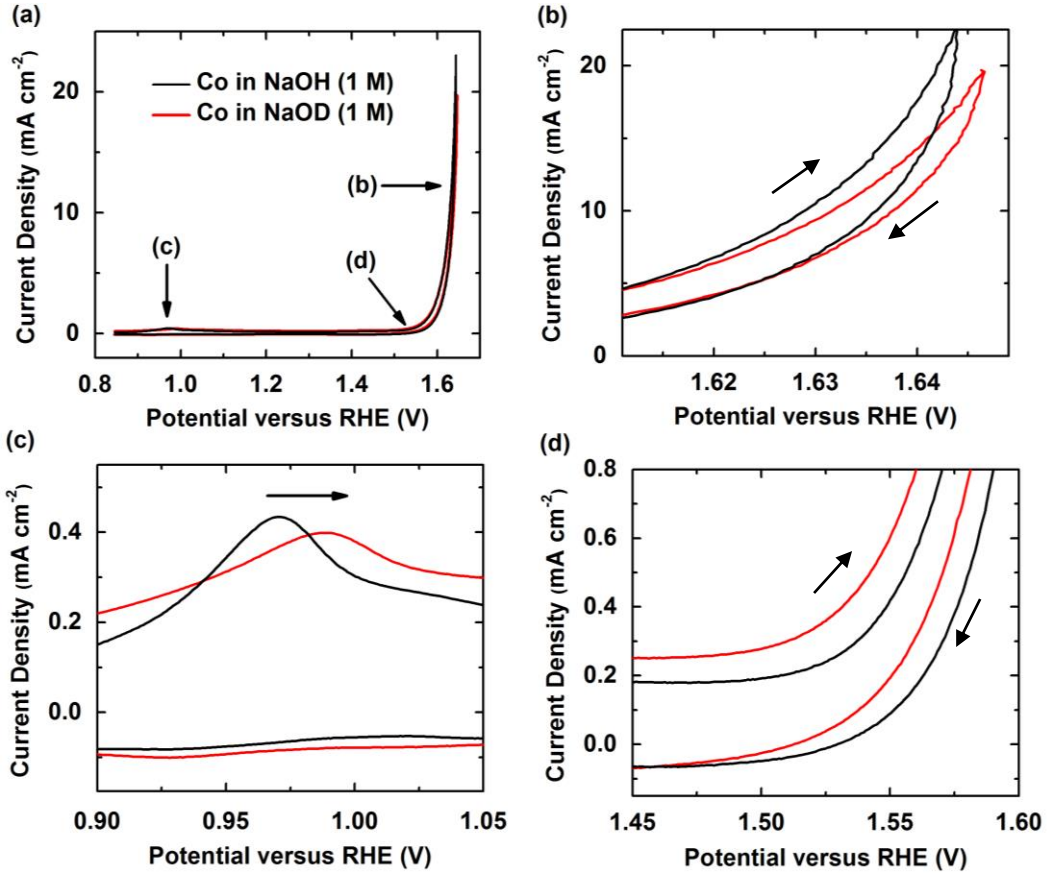

Figure 4.5. (a) IR-corrected CVs of Co in NaOH (1 M) and NaOD (1 M) solutions. (b), (c), and (d) display the blowups of the diffusion-controlled OER region, the Co(II/III) redox region, and the OER onset region, respectively.

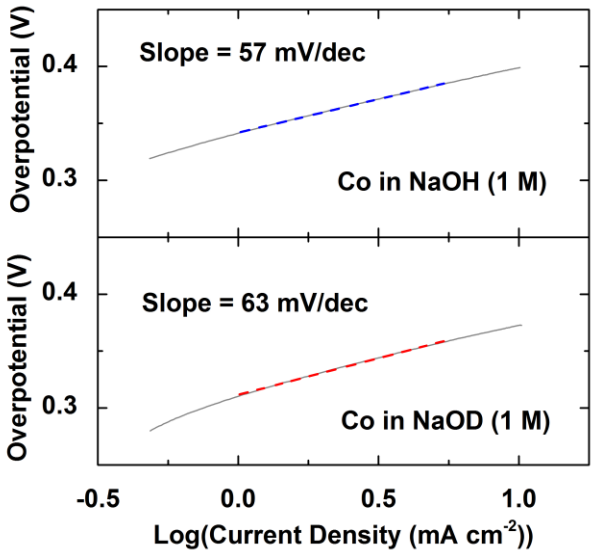

Figure 4.6. Tafel plots of Co in (top) 1 M NaOH and (bottom) 1 M NaOD solutions.

4.3.3. Au OER catalysts in proteo and deutero solutions

In order to confirm that these KIE less than 1 were a result of the catalysts being studied, we carried out similar experiments on a Au electrode.

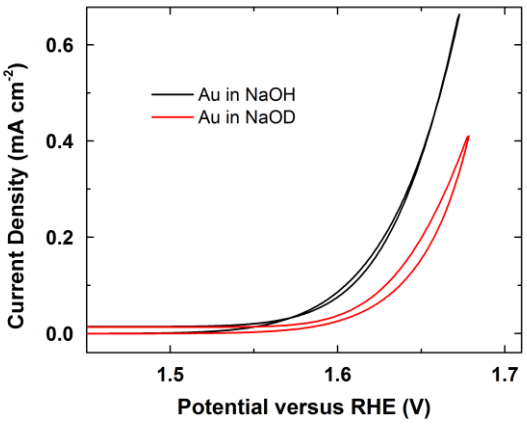

Figure 4.7. IR-uncorrected CVs of Au in NaOH (1 M) and NaOD (1 M) solutions at OER region.

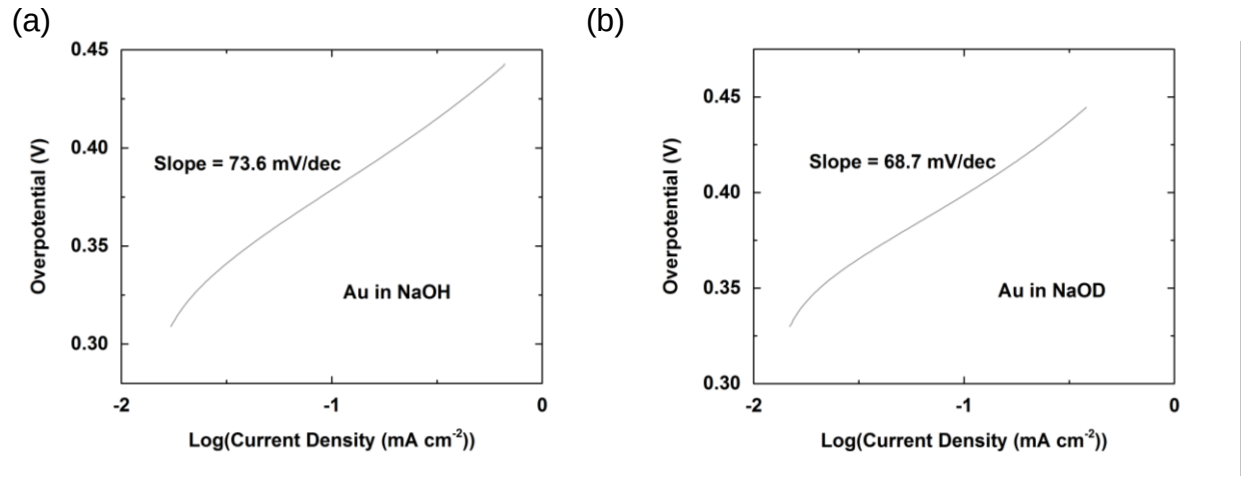

Figure 4.8. Tafel plots of Au in (a) 1 M NaOH and (b) 1 M NaOD solutions.

Figure 4.7 shows that OER activity of Au in 1M NaOH (black) is higher than Au in 1 M NaOD (red). The Tafel slope found in NaOH (Figure 4.8a) is (73 ± 1) mV dec^{-1}, which is larger than the corresponding slope (67 ± 2) mV dec^{-1} found in NaOD (Figure 4.8b). Using the Tafel slopes found, the calculated KIE is 1.09. A k_H/k_D value of above 1 is indicative of a normal KIE (Table 4.2).

Table 4.2. Summary of the overpotential at 0.5 mA cm^{-2}, Tafel slope and kinetic isotope effect of OER catalyzed by Au in 1 M NaOH and 1 M NaOD solutions.

Condition	**Overpotential at 0.5 mA cm^{-2} (V)**	**Tafel Slope (mV dec^{-1})**	**k_H/k_D**
Au in 1 M NaOH	0.428 ± 0.006	73 ± 1	1.09 ± 0.05
Au in 1 M NaOD	0.484 ± 0.026	67 ± 2	

The normal KIE of Au in alkaline solution is in agreement with previous reports.[79] The normal KIE found in the Au case indicates that the RDS of the OER of Au involves forming or

breaking of O-H or O-D bonds (Scheme 4.1). This result agrees with OER mechanism of Au suggested previously.[16,17]

$$\mathrm{Au(III)(OH)_3} \rightarrow [\mathrm{Au(III)(OH)_3}]^+ + \mathrm{e}^- \quad (1)$$

$$[\mathrm{Au(III)(OH)_3}]^+ + \mathrm{OH}^- \rightarrow [\mathrm{Au(III)(OH)}(OOH)]^+ + H_2O + \mathrm{e}^- \quad (2)$$

$$[\mathrm{Au(III)(OH)}(OOH)]^+ + \mathrm{OH}^- \rightarrow [\mathrm{Au(III)(OH)}]^{2+} + H_2O + O_2 + 2\mathrm{e}^- \quad (3)$$

$$[\mathrm{Au(III)(OH)}]^{2+} + 2\mathrm{OH}^- \rightarrow \mathrm{Au(III)(OH)_3} \quad (4)$$

Scheme 4.1. An OER mechanism that involves Au. A plausible RDS is denoted in red.

4.3.4. Raman of a Ni, Co and Au OER catalysts in proteo and deutero solutions

To further investigate the KIE, we studied electrodeposited thin films of Ni and Co on roughened Au surfaces using potential-dependent SERS. Figure 4.9a shows potential-dependent Raman spectra of a Ni thin film electrodeposited on Au acquired in 1 M NaOH. The two distinct bands at 480 cm^{-1} and 560 cm^{-1} which can be assigned to M-O bands are consistent with previous results.[30,31] We compared the location of these bands in 1 M NaOH and 1 M NaOD and did not observe a redshift, which if observed would indicate strongly bound metal-hydroxide/deuteroxide species (Table 4.3). The absence of an apparent redshift has been confirmed previously for several studies using similar systems.[32,92,93] Figure 4.9c displays Raman spectra of a Co thin film electrodeposited on Au collected in 1 M NaOH under potential control. The two bands at 489 cm^{-1} and 616 cm^{-1} match with values reported in the literature.[94] Analogous to the Ni case, these Co-related bands do not redshift significantly upon deuteration (Figure 4.9d), suggesting that the phenomenon could be a common feature for transition metal oxyhydroxide thin films. The lack of a redshift in NPM thin films is explained by the absence of strongly associated protons in the

layered structure of the porous first-row transition metal electrocatalysts.[95-97] By contrast, for precious third-row transition metal catalysts, such as Au, we observed a redshift in their corresponding OH^- associated Raman band upon deuteration (Figure 4.10).[98]

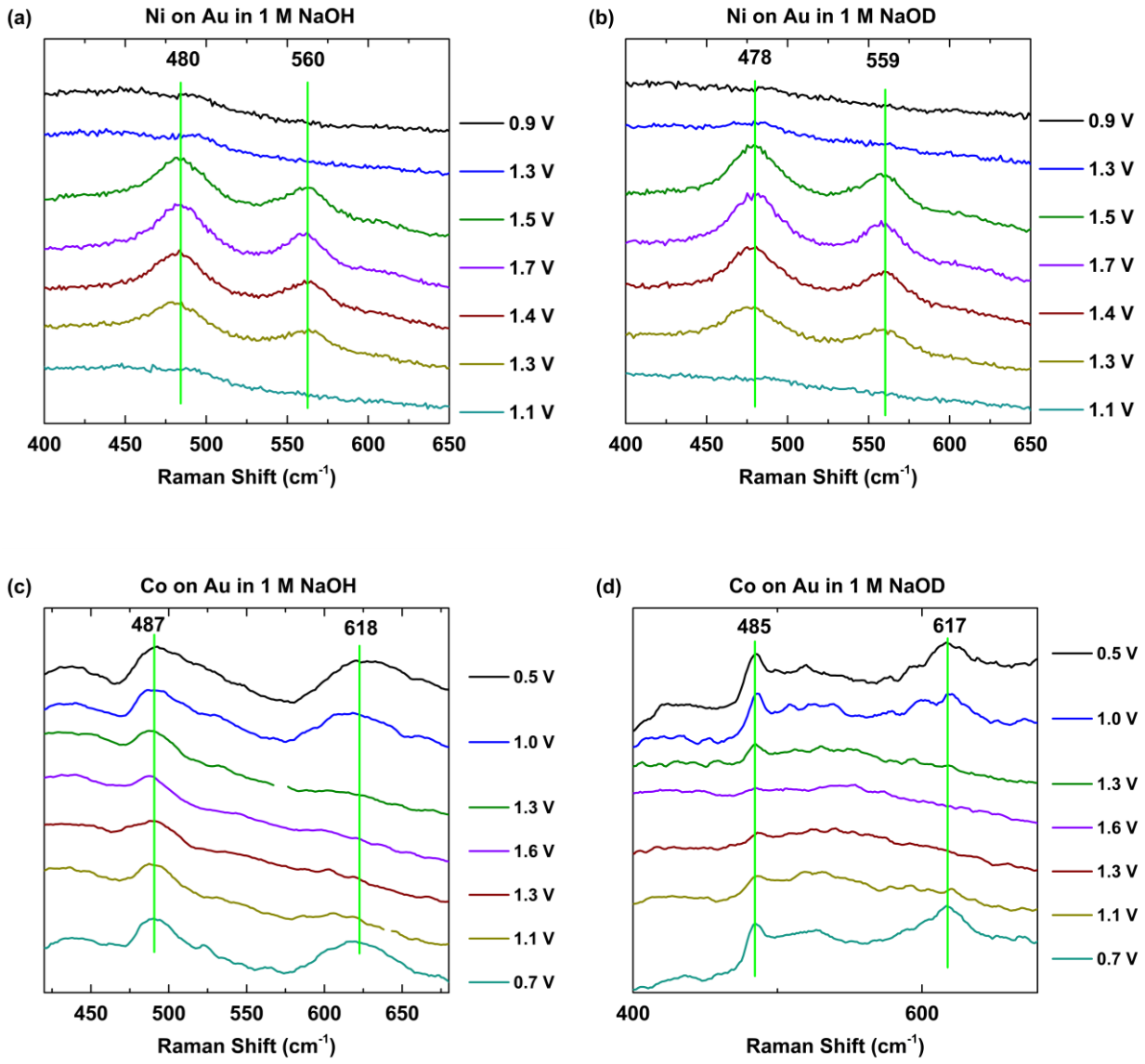

Figure 4.9. *In situ* SERS of Ni on Au in (a) 1 M NaOH and (b) 1 M NaOD, and Co on Au in (c) 1 M NaOH and (d) 1 M NaOD.

Table 4.3. Expected Raman shift upon deuteration of alkaline solution for Ni, Co and Au electrodes.

	Ni		Co		Au	
M	58.7		58.9		197	
OH	17.0		17.0		17.0	
OD	18.0		18.0		18.0	
μM-OH	13.2		13.2		15.7	
μM-OD	13.8		13.8		16.5	
υM-OH (cm^{-1})	480[18-20]	560[18-20]	487[20,21]	618[20,21]	425[22,23]	555[22,23]
υM-OD (cm^{-1})	470	548	476	605	414	541
Shift Δυ (cm^{-1})	**10**	**12**	**11**	**13**	**11**	**14**

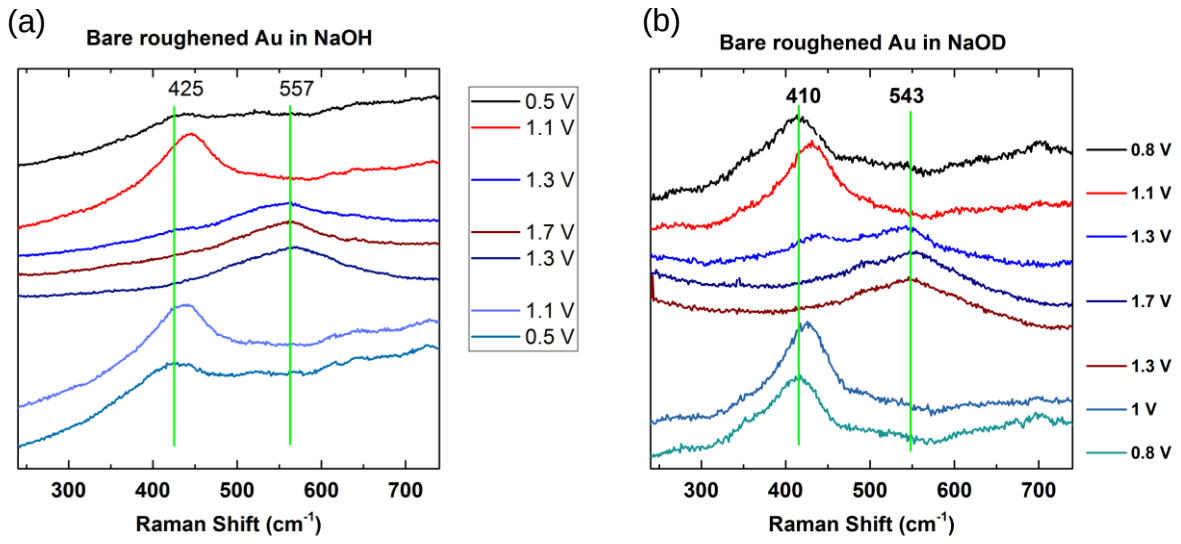

Figure 4.10. *In situ* SERS of Au in (a) 1 M NaOH and (b) 1 M NaOD.

4.3.5. Origins of the inverse KIE during the OER

We next address the possible origins of the inverse KIE found for the OER on Ni and Co in basic solutions. First, inverse KIEs are usually associated with differences in the steric environment of the active site caused by deuteration during the rate-determining step (RDS).[60] For example, interconversions of sterically-hindered biaryls typically exhibit inverse KIEs of ca. 0.8.[60,99-102] A comparison between the racemization rates of 2,2'-dibromo-4,4'-dicarboxybiphenyl and its 6,6'-dideutero derivative gives an inverse KIE of 0.85.[103-105] Another comparison of the inversion rates of 9,10-dihydroxy-4,5-dimethylphenanthrene and its derivative with the two methyl groups fully deuterated yields an inverse KIE of 0.86.[106,107] Translating this steric argument to the OER leads to a possible scenario shown in Figures 4.11a and 4.11b where surface crowding could lead to an inverse KIE. Literature study reveals that a O-D bond is shorter than a O-H bond,[108] meaning that the O-D bond in MO(OD) is likely shorter than the O-H bond in MO(OH), where M = Ni or Co. The shorter O-D bond could lead to a less occluded active site, resulting in a less hindered pathway for reactants to diffuse to the MO(OD) surface as compared to the MO(OH) surface. As a result, the less bulky MO(OD) structure would exhibit faster OER kinetics. Our model shows a particular case in which a single metal center is the locus of reactivity, but this idea could easily be extended to a multi-metallic active site, as has been proposed in other work.[18,19,23,109-111]

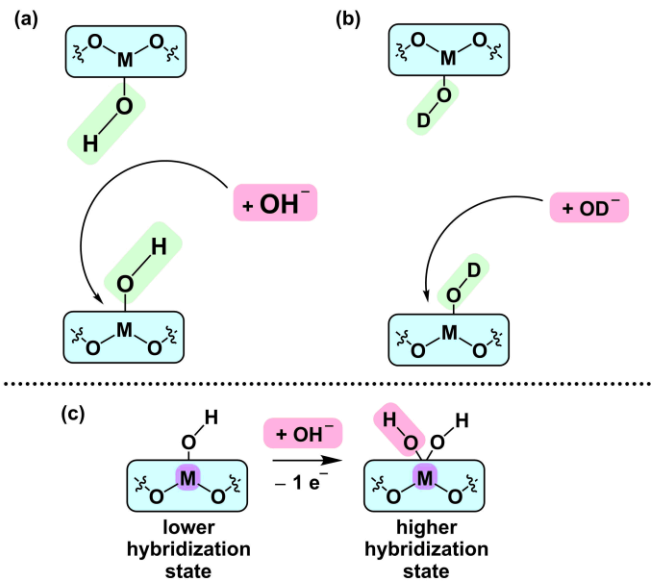

Figure 4.11. A possible scenario of the OER process catalyzed by M (Ni or Co) surface oxyhydroxides in which an inverse KIE can be observed highlighting (a) the hydroxide and (b) deuteroxide (green) that impart KIE on the adjacent bond forming or breaking site, and (c) the change in coordination environment and the corresponding rehybridization of the metal center (violet) upon accommodating an incoming OH^- species (pink).

A second origin of an inverse KIE results from a change from a less hybridized state to a more hybridized state (e.g. sp^2 to sp^3) during the RDS.[60] The typical observed KIE relating to this type of rehybridization is about 0.9. For example, solvolyses of methyl esters containing iodide and their deuterated derivatives lead to inverse KIEs of ca. 0.87.[112] A change in the hybridization state during the RDS leads to a larger difference in the Δ zero point energy (Δ ZPE) of the transition state than in the ΔZPE in the ground state. Figure 4.11c displays a possible scenario where a change in the coordination environment of M (Ni or Co) could result in an inverse KIE. In this model, the MO(OH) changes hybridization state upon binding of a OH^-. Therefore, the ΔZPE for the case involving OD^- as the incoming species may be larger than that for the OH^- case.

A third explanation for an inverse KIE invokes an electronic argument.[60] The magnitude of an inductive KIE is typically about 0.95, a less significant effect than the two types of inverse KIEs previously discussed.[60,113] Deuterium substitution at a position more remote than β to the reaction center along an alkyl chain yields an inverse KIE of 0.97.[114,115] D is more electropositive than H, meaning that D is more electron releasing.[116,117] Due to the difference in electron donating ability, OD^- is more polar than OH^-, resulting in a higher OD^- flux towards the positively charged metal centers.

Each of the previously reported explanations has an inverse KIE with a value c.a. 0.9. However, our observations of the KIE on Ni and Co for the OER indicate a value much lower at 0.5. At this point, it is not possible to distinguish between the different origins of the inverse KIE as it applies to the OER but the relatively large inverse KIEs that we report here might suggest that multiple effects could be present, as has been demonstrated in other systems.[59,114]

4.3.6. Mechanistic implications for the OER

Next, we evaluate possible OER mechanisms in the context of the inverse KIE based on the many OER mechanisms which have been proposed in literature.[111] The lack of a primary normal KIE indicates that O-H or O-D bonds are not cleaved during the RDS of the OER. Instead, by applying the rationales presented in Section 4.3.5, the observed inverse KIE suggests that the RDS involves forming or breaking of a bond (1) without a direct involvement of H or D, (2) within the vicinity of an OH or OD moiety, and/or (3) with a change of the metal center or the bound oxygen atom from a less hybridized state to a more hybridized state.

The question of whether oxygen contained in the metal oxide surface participates directly in the formation of molecular O_2 is still controversial. Therefore, in literature, there are two categories of mechanism, one only focusing on the adsorbed species and ignoring metal oxides on the surface, and the second involving the evolution of metal oxides during the catalytic cycle. The observation of an inverse KIE indicates that there must be bond breaking/forming with a proton adjacent. Thus, the reaction of weakly adsorbed species, particularly OH^- might not be strong enough to show effects on KIE of the OER. Metal oxyhydroxide, which is widely accepted as the active material for the OER, should be the starting species in the OER catalytic cycle. In consideration of this information, we believe that one feasible pathway for OER is as follows:

$$M(III)O(OH) + OH^- \rightarrow M(IV)O(OH)_2 + e^- \quad (1)$$

$$M(IV)O(OH)_2 \rightarrow [M(IV)O(OH)_2]^+ + e^- \quad (2)$$

$$[M(IV)O(OH)_2]^+ + 2OH^- \rightarrow [M(III)O]^+ + O_2 + 2H_2O + 2e^- \quad (3)$$

$$[M(III)O]^+ + OH^- \rightarrow M(III)O(OH) \quad (4)$$

Scheme 4.2. An OER mechanism that involves metal oxides (M = Ni or Co).[18,109,118] A plausible RDS is denoted in red. A proton that imparts an inverse KIE on the adjacent bond forming or breaking site is denoted in green.

Scheme 4.2 shows an OER mechanism that involves the addition of a OH^- to the metal center coupled with electron transfer, a so-called electrochemical-chemical (EC) step, which changes the geometry and the coordination number of the metal center.[18,109,118] The expected Tafel slope for step 1 is 60 mV/dec, which is consistent with the ~54 mV/dec Tafel slope observed experimentally. Step 1 is a plausible RDS because this EC step involves the formation of a M-O bond next to an existing OH moiety, which provides the steric crowding required for the observed

inverse KIE.[60,119] We emphasize that the new data we provide here does not uniquely specify the mechanism of the OER on Ni and Co, but certainly provides constraints consistent with Eqs 1-4 above. For example, the results from our KIE studies cannot differentiate between the mechanism with a coupled EC step in concert and the mechanism with sequential electrochemical (E) and chemical (C) steps in tandem. It is noteworthy to point out that a flip in the order of the reaction, i.e. a C step followed by an E step, would not yield the observed Tafel slope regardless of whether C or E is rate-limiting.[119] Step 2 is a E step that does not satisfy the KIE requirement.[120] A rate-limiting E step preceded by a EC step would result in a Tafel slope different from the experimentally observed value.[119] Step 3 cannot be the RDS because it contains a deprotonation step and direct cleavage of an O-H bond should give a measurable normal KIE.[59] Step 4 is not a RDS because it involves the addition of a OH^- to M without neighboring OH functionalities.

$$M(III)O(OH) + OH^- \rightarrow M(IV)O(OH)_2 + e^- \quad (5)$$

$$M(IV)O(OH)_2 \rightarrow [M(IV)O]^+H_2O_2 + e^- \quad (6)$$

$$[M(IV)O]^+H_2O_2 + 2OH^- \rightarrow [M(III)O]^+ + O_2 + 2H_2O + 2e^- \quad (7)$$

$$[M(III)O]^+ + OH^- \rightarrow M(III)O(OH) \quad (8)$$

Scheme 4.3. An OER mechanism that entails a H_2O_2 intermediate species.[18,19,109] A plausible RDS is represented in red. A proton that imparts KIE on the adjacent bond forming or breaking site is represented in green.

Scheme 4.3 shows an intriguing pathway that invokes the involvement of a H_2O_2 intermediate.[18,19,109] Analogous to step 1 in Scheme 4.2, step 5 in Scheme 4.3 is a plausible RDS because the formation of a M-O bond close to an existing OH group fits the criteria required to yield an inverse KIE and the observed Tafel slope.[60] Similar to step 2 in Scheme 4.2, step 6 in

Scheme 4.3 is likely not rate-limiting because the step involves a single electron transfer which is not consistent with the results from both the KIE study and the Tafel slope analysis. Step 7 includes a deprotonation step, and step 8 entails the addition of a OH^- to M without neighboring OH functionalities. Therefore, the likelihood of steps 7 and 8 to be rate-limiting is low.

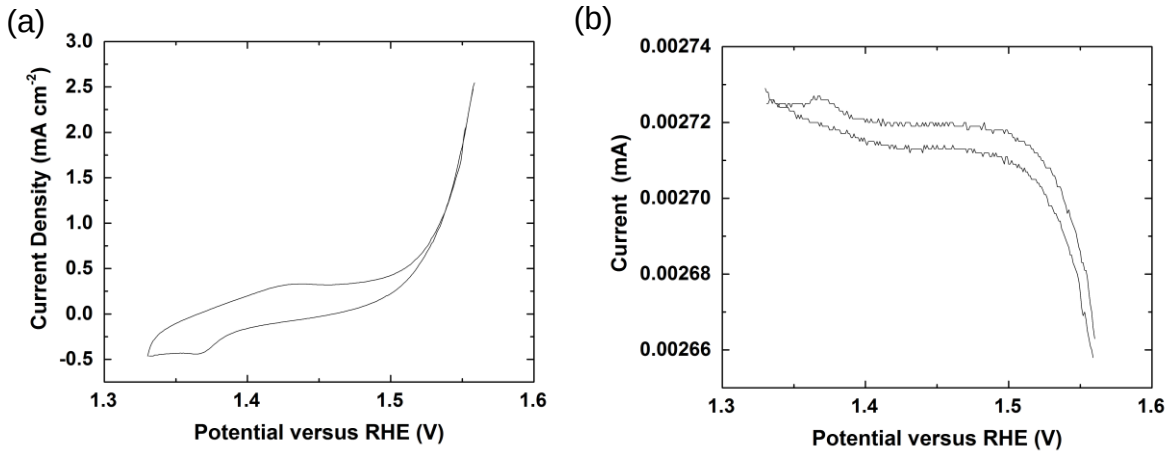

Figure 4.12. Rotating ring-disk electrode voltammograms recorded using a Ni disk and a Pt ring in 1 M NaOH at 1600 r.p.m. (a) disk current density at a scan rate of 10 mV/s, and (b) ring current at constant 1.3 V vs. RHE.

A question remains as to whether the H_2O_2 generated *in situ* stays bound on the catalyst active site. A release of H_2O_2 likely results in a change of the metal center from a more hybridized state to a less hybridized step, which would lead to a normal KIE if it was the RDS.[59] To further investigate the possibility of H_2O_2 dissolution, we performed rotating ring-disk electrode (RRDE) experiments using a Ni disk and a Pt ring to detect any free peroxide produced during the OER. Figure 4.12 shows that over a wide range of Ni electrode potentials from 1.0 V to 1.7 V vs. RHE involving the oxidation of Ni and water, no H_2O_2 was detected as evidenced by the lack of ring current at the Pt ring held at 1.3 V vs. RHE. This result indicates that no H_2O_2 is released into the bulk solution as a side product suggesting that any mechanism involving H_2O_2 generation (such

as that suggested in Scheme 4.3) must require the H_2O_2 bound adduct to be oxidized efficiently so that it is not released.

$$^{-}OH \longrightarrow (OH)_{ads} + e^{-} \quad (1)$$

$$(OH)_{ads} + {}^{-}OH \longrightarrow (O^{-})_{ads} + H_2O \quad (2)$$

$$(O^{-})_{ads} \longrightarrow (O)_{ads} + e^{-} \quad (3)$$

$$2\,(O^{-})_{ads} \longrightarrow O_2 \quad (4)$$

Scheme 4.4. An OER mechanism focusing on the adsorbed species.[86,87]

We further examined a mechanism that focuses primarily on the adsorbates and applied the insights we gained from this KIE study to exclude this mechanism as a plausible OER mechanism on Ni and Co electrodes (see Scheme 4.4). Given the evidence presented here, Schemes 4.2 and 4.3 are plausible mechanisms for the OER on Ni and Co catalysts. Both schemes satisfy the main requirements of the observed Tafel slope and an inverse KIE, namely the forming or breaking of a bond that is adjacent to OH/OD with a change from a less to a more hybridized state on the metal or oxygen center but that does not involve H or D directly.

4.4. Conclusions

In this report, we investigated the effect of deuteration on the OER activities of NPM catalysts. We found inverse KIEs of 0.6 and 0.5 for OER on Ni and Co, respectively. The KIE results suggest that a rate-limiting bond breaking or forming event, which does not involve the direct cleavage of an O-H bond, likely occurs at an occluded site on the electrode surface with adjacent OH functionalities. Additionally, our RRDE experiments suggest that H_2O_2 is not released as a stable intermediate during OER. Our results, including KIE experiments, Tafel slope analyses, RRDE data, and Raman spectroscopy, provide important constraints for the nature of the

RDS during the OER, which must be considered during the search for more competent OER catalysts. The mechanistic insight gained from the KIE in our OER experiments will be useful to the broad community interested in both the fundamental aspects of PCET processes and the development of active, robust, and inexpensive electrocatalysts.

4.5. References

(1) Costentin, C.; Robert, M.; Savéant, J.-M. *Chem. Rev.* **2010**, 110, PR1-PR40.

(2) Mayer, J. M.; Rhile, I. J. *BBA-Bioenergetics* **2004**, 1655, 51-58.

(3) Hammes-Schiffer, S.; Soudackov, A. V. *J. Phys. Chem. B* **2008**, 112, 14108-14123.

(4) Weinberg, D. R.; Gagliardi, C. J.; Hull, J. F.; Murphy, C. F.; Kent, C. A.; Westlake, B. C.; Paul, A.; Ess, D. H.; McCafferty, D. G.; Meyer, T. J. *Chem. Rev.* **2012**, 112, 4016-4093.

(5) Barile, C. J.; Tse, E. C. M.; Li, Y.; Sobyra, T. B.; Zimmerman, S. C.; Hosseini, A.; Gewirth, A. A. *Nat. Mater.* **2014**, 13, 619-623.

(6) Jiang, J.; Zhang, A.; Li, L.; Ai, L. *J. Power Sources* **2015**, 278, 445-451.

(7) Song, F.; Hu, X. *Nat. Commun.* **2014**, 5, 4477.

(8) Long, X.; Wang, Z.; Xiao, S.; An, Y.; Yang, S. *Mater. Today* **2016**, 19, 213-226.

(9) Mavros, M. G.; Tsuchimochi, T.; Kowalczyk, T.; McIsaac, A.; Wang, L.-P.; Voorhis, T. V. *Inorg. Chem.* **2014**, 53, 6386-6397.

(10) Laguna-Bercero, M. A. *J. Power Sources* **2012**, 203, 4-16.

(11) Man, I. C.; Su, H.-Y.; Calle-Vallejo, F.; Hansen, H. A.; Martínez, J. I.; Inoglu, N. G.; Kitchin, J.; Jaramillo, T. F.; Nørskov, J. K.; Rossmeisl, J. *ChemCatChem* **2011**, 3, 1159-1165.

(12) Doyle, R. L.; Godwin, I. J.; Brandon, M. P.; Lyons, M. E. G. *Phys. Chem. Chem. Phys.* **2013**, 15, 13737-13783.

(13) Carmo, M.; Fritz, D. L.; Mergel, J.; Stolten, D. *Int. J. Hydrogen Energy* **2013**, 38, 4901-4934.

(14) Han, N.; Zhao, F.; Li, Y. *J. Mater. Chem. A* **2015**, 3, 16348-16353.

(15) Katsounaros, I.; Cherevko, S.; Zeradjanin, A. R.; Mayrhofer, K. J. J. *Angew. Chem. Int. Ed.* **2014**, 53, 102-121.

(16) Zhang, J.; Xie, Z.; Zhang, J.; Tang, Y.; Song, C.; Navessin, T.; Shi, Z.; Song, D.; Wang, H.; Wilkinson, D. P.; Liu, Z.-S.; Holdcroft, S. *J. Power Sources* **2006**, 160, 872-891.

(17) Gewirth, A. A.; Thorum, M. S. *Inorg. Chem.* **2010**, 49, 3557-3566.

(18) Lyons, M. E. G.; Brandon, M. P. *Int. J. Electrochem. Sci.* **2008**, 3, 1386-1424.

(19) Lyons, M. E. G.; Brandon, M. P. *Int. J. Electrochem. Sci.* **2008**, 3, 1425-1462.

(20) Reier, T.; Oezaslan, M.; Strasser, P. *ACS Catal.* **2012**, 2, 1765-1772.

(21) Hall, D. E. *J. Electrochem. Soc.* **1985**, 132, 41C-48C.

(22) Dau, H.; Limberg, C.; Reier, T.; Risch, M.; Roggan, S.; Strasser, P. *ChemCatChem* **2010**, 2, 724-761.

(23) Lyons, M. E. G.; Brandon, M. P. *J. Electroanal. Chem.* **2010**, 641, 119-130.

(24) Miles, M. H.; Kissel, G.; Lu, P. W. T.; Srinivasan, S. *J. Electrochem. Soc.* **1976**, 123, 332-336.

(25) Godwin, I. J.; Lyons, M. E. G. *Electrochem. Commun.* **2013**, 32, 39-42.

(26) Rossmeisl, J.; Logadottir, A.; Nørskov, J. K. *Chem. Phys.* **2005**, 319, 178-184.

(27) Hoang, T. T. H.; Gewirth, A. A. *ACS Catal.* **2016**, 6, 1159-1164.

(28) Jaksic, M. M.; Johansen, B.; Tunold, R. *Int. J. Hydrogen Energy* **1994**, 19, 321-335.

(29) Behl, W. K.; Toni, J. E. *J. Electroanal. Chem. Interfacial Electrochem.* **1971**, 31, 63-75.

(30) Yeo, B. S.; Bell, A. T. *J. Phys. Chem. C* **2012**, 116, 8394-8400.

(31) Melendres, C. A.; Xu, S. *J. Electrochem. Soc.* **1984**, 131, 2239-2243.

(32) Desilvestro, J.; Corrigan, D. A.; Weaver, M. J. *J. Electrochem. Soc.* **1988**, 135, 885-892.

(33) Bewick, A.; Gutiérrez, C.; Larramona, G. *J. Electroanal. Chem.* **1992**, 333, 165-175.

(34) Ismail, K. M.; Badawy, W. A. *J. Appl. Electrochem.* **2000**, 30, 1303-1311.

(35) Kötz, R.; Neff, H.; Stucki, S. *J. Electrochem. Soc.* **1984**, 131, 72-77.

(36) Peuckert, M. *Electrochim. Acta* **1984**, 29, 1315-1320.

(37) Foelske, A.; Strehblow, H.-H. *Surf. Interface Anal.* **2002**, 34, 125-129.

(38) Medway, S. L.; Lucas, C. A.; Kowal, A.; Nichols, R. J.; Johnson, D. *J. Electroanal. Chem.* **2006**, 587, 172-181.

(39) Pralong, V.; Delahaye-Vidal, A.; Beaudoin, B.; Gerand, B.; Tarascon, J. M. *J. Mater. Chem.* **1999**, 9, 955-960.

(40) Hillman, A. R.; Skopek, M. A.; Gurman, S. J. *Phys. Chem. Chem. Phys.* **2011**, 13, 5252-5263.

(41) Totir, D.; Mo, Y.; Kim, S.; Antonio, M. R.; Scherson, D. A. *J. Electrochem. Soc.* **2000**, 147, 4594-4597.

(42) Mo, Y.; Stefan, I. C.; Cai, W.-B.; Dong, J.; Carey, P.; Scherson, D. A. *J. Phys. Chem. B* **2002**, 106, 3681-3686.

(43) Li, X.; Walsh, F. C.; Pletcher, D. *Phys. Chem. Chem. Phys.* **2011**, 13, 1162-1167.

(44) Yau, S.-L.; Fan, F.-R. F.; Moffat, T. P.; Bard, A. J. *J. Phys. Chem.* **1994**, 98, 5493-5499.

(45) Kong, F.; Kostecki, R.; McLarnon, F.; Muller, R. H. *Thin Solid Films* **1998**, 313–314, 775-780.

(46) Lu, P. W. T.; Srinivasan, S. *J. Electrochem. Soc.* **1978**, 125, 1416-1422.

(47) Hu, Y.; Scherson, D. A. *J. Phys. Chem. B* **1997**, 101, 5370-5376.

(48) Kowal, A.; Niewiara, R.; Perończyk, B.; Haber, J. *Langmuir* **1996**, 12, 2332-2333.

(49) Mo, Y.; Hwang, E.; Scherson, D. A. *J. Electrochem. Soc.* **1996**, 143, 37-43.

(50) Birss, V. I.; Elzanowska, H.; Gottesfeld, S. *J. Electroanal. Chem. Interfacial Electrochem.* **1991**, 318, 327-333.

(51) Juodkazytė, J.; Šebeka, B.; Stalnionis, G.; Juodkazis, K. *Electroanalysis* **2005**, 17, 1734-1739.

(52) Zhen, C.-H.; Sun, S.-G.; Fan, C.-J.; Chen, S.-P.; Mao, B.-W.; Fan, Y.-J. *Electrochim. Acta* **2004**, 49, 1249-1255.

(53) Hoang, T. T. H.; Cohen, Y.; Gewirth, A. A. *Anal. Chem.* **2014**, 86, 11290-11297.

(54) Burke, M. S.; Enman, L. J.; Batchellor, A. S.; Zou, S.; Boettcher, S. W. *Chem. Mater.* **2015**, 27, 7549-7558.

(55) Bergmann, A.; Martinez-Moreno, E.; Teschner, D.; Chernev, P.; Gliech, M.; de Araujo, J. F.; Reier, T.; Dau, H.; Strasser, P. *Nat. Commun.* **2015**, 6, 8625.

(56) Christensen, N. J.; Fristrup, P. *Synlett* **2015**, 26, 508-513.

(57) Klinman, J. P. *FEBS Journal* **2014**, 281, 489-497.

(58) Nelson, S. D.; Trager, W. F. *Drug Metab. Dispos.* **2003**, 31, 1481-1497.

(59) Gómez-Gallego, M.; Sierra, M. A. *Chem. Rev.* **2011**, 111, 4857-4963.

(60) Saunders, W. H.; Melander, L. R. *Reaction Rates of Isotopic Molecules*; Wiley: New York, 1980.

(61) Conway, B. E.; Salomon, M. *J. Chem. Phys.* **1964**, 41, 3169-3177.

(62) Salomon, M.; Conway, B. E. *Ber. Bunsen-Ges. Phys. Chem.* **1965**, 69, 669-674.

(63) Krishtalik, L. I. *Electrochim. Acta* **2001**, 46, 2949-2960.

(64) Ghoneim, M. M.; Clouser, S.; Yeager, E. *J. Electrochem. Soc.* **1985**, 132, 1160-1162.

(65) Jaksic, M. M.; Johansen, B.; Tunold, R. *Int. J. Hydrogen Energy* **1993**, 18, 817-837.

(66) Jaksic, M. M.; Johansen, B.; Tunold, R. *Int. J. Hydrogen Energy* **1993**, 18, 111-124.

(67) Jaksic, M. M.; Johansen, B.; Tunold, R. *Int. J. Hydrogen Energy* **1994**, 19, 35-51.

(68) Diaz-Morales, O.; Ferrus-Suspedra, D.; Koper, M. T. M. *Chem. Sci.* **2016**, 7, 2639-2645.

(69) Bard, A. J.; Faulkner, L. R. *Electrochemical Methods: Fundamentals and Applications, 2nd Edition*; Wiley: New York, 2000.

(70) van der Vliet, D.; Strmcnik, D. S.; Wang, C.; Stamenkovic, V. R.; Markovic, N. M.; Koper, M. T. M. *J. Electroanal. Chem.* **2010**, 647, 29-34.

(71) Tse, E. C. M.; Gewirth, A. A. *J. Phys. Chem. A* **2015**, 119, 1246-1255.

(72) Weaver, M. J.; Nettles, S. M. *Inorg. Chem.* **1980**, 19, 1641-1646.

(73) Tse, E. C. M.; Barile, C. J.; Kirchschlager, N. A.; Li, Y.; Gewargis, J. P.; Zimmerman, S. C.; Hosseini, A.; Gewirth, A. A. *Nat. Mater.* **2016**, 15, 754-759.

(74) Tse, E. C. M.; Schilter, D.; Gray, D. L.; Rauchfuss, T. B.; Gewirth, A. A. *Inorg. Chem.* **2014**, 53, 8505-8516.

(75) Thorseth, M. A.; Letko, C. S.; Tse, E. C. M.; Rauchfuss, T. B.; Gewirth, A. A. *Inorg. Chem.* **2012**, 52, 628-634.

(76) Gao, P.; Gosztola, D.; Leung, L.-W. H.; Weaver, M. J. *J. Electroanal. Chem. Interfacial Electrochem.* **1987**, 233, 211-222.

(77) Thorum, M. S.; Anderson, C. A.; Hatch, J. J.; Campbell, A. S.; Marshall, N. M.; Zimmerman, S. C.; Lu, Y.; Gewirth, A. A. *J. Phys. Chem. Lett.* **2010**, 1, 2251-2254.

(78) Schultz, Z. D.; Feng, Z. V.; Biggin, M. E.; Gewirth, A. A. *J. Electrochem. Soc.* **2006**, 153, C97-C107.

(79) Jaksic, M. M.; Johansen, B.; Tunold, R. *Int. J. Hydrogen Energy* **1993**, 18, 91-110.

(80) Zhang, Y.; Gao, X.; Weaver, M. J. *J. Phys. Chem.* **1993**, 97, 8656-8663.

(81) Lyons, M. E. G.; Doyle, R. L.; Godwin, I.; O'Brien, M.; Russell, L. *J. Electrochem. Soc.* **2012**, 159, H932-H944.

(82) Trotochaud, L.; Ranney, J. K.; Williams, K. N.; Boettcher, S. W. *J. Am. Chem. Soc.* **2012**, 134, 17253-17261.

(83) Pourbaix, M. *Atlas of Electrochemical Equilibria in Aqueous Solutions*; National Association of Corrosion Engineers: Houston, 1974.

(84) Weaver, M. J.; Tyma, P. D.; Nettles, S. M. *J. Electroanal. Chem.* **1980**, 114, 53-72.

(85) Frank, H. S.; Wen, W.-Y. *Discuss. Faraday Soc.* **1957**, 24, 133-140.

(86) Boyarkin, O. V.; Koshelev, M. A.; Aseev, O.; Maksyutenko, P.; Rizzo, T. R.; Zobov, N. F.; Lodi, L.; Tennyson, J.; Polyansky, O. L. *Chem. Phys. Lett.* **2013**, 568–569, 14-20.

(87) Lyons, M. E. G.; Cakara, A.; O'Brien, P.; Godwin, I.; Doyle, R. L. *Int. J. Electrochem. Sci.* **2012**, 7, 11768-11795.

(88) Franks, F. *The Physics and Physical Chemistry of Water*; Springer: New York, 2012.

(89) Liu, H.; Macedo, E. A. *J. Supercrit. Fluids* **1995**, 8, 310-317.

(90) Costentin, C.; Drouet, S.; Robert, M.; Savéant, J.-M. *J. Am. Chem. Soc.* **2012**, 134, 11235-11242.

(91) Solomon, E. I.; Augustine, A. J.; Yoon, J. *Dalton Trans.* **2008**, 3921-3932.

(92) Desilvestro, J.; Corrigan, D. A.; Weaver, M. J. *J. Phys. Chem.* **1986**, 90, 6408-6411.

(93) Oblonsky, L. J.; Devine, T. M. *J. Electrochem. Soc.* **1995**, 142, 3677-3682.

(94) Yeo, B. S.; Bell, A. T. *J. Am. Chem. Soc.* **2011**, 133, 5587-5593.

(95) Melendres, C. A.; Paden, W.; Tani, B.; Walczak, W. *J. Electrochem. Soc.* **1987**, 134, 762-763.

(96) Kostecki, R.; McLarnon, F. *J. Electrochem. Soc.* **1997**, 144, 485-493.

(97) Johnston, C.; Graves, P. R. *Appl. Spectrosc.* **1990**, 44, 105-115.

(98) Zou, S.; Chan, H. Y. H.; Williams, C. T.; Weaver, M. J. *Langmuir* **2000**, 16, 754-763.

(99) Carter, R. E.; Dahlgren, L. *Acta Chem. Scand.* **1969**, 23, 504-514.

(100) Bartell, L. S. *J. Am. Chem. Soc.* **1961**, 83, 3567-3571.

(101) Bartell, L. S. *Tetrahedron Lett.* **1960**, 1, 13-16.

(102) Carter, R. E.; Dahlgren, L. *Acta Chem. Scand.* **1970**, 24, 633-643.

(103) Melander, L.; Carter, R. E. *Acta Chem. Scand.* **1964**, 18, 1138-1149.

(104) Westheimer, F. H. *J. Chem. Phys.* **1947**, 15, 252-260.

(105) Westheimer, F. H.; Mayer, J. E. *J. Chem. Phys.* **1946**, 14, 733-738.

(106) Mislow, K.; Graeve, R.; Gordon, A. J.; Wahl, G. H. *J. Am. Chem. Soc.* **1964**, 86, 1733-1741.

(107) Mislow, K.; Graeve, R.; Gordon, A. J.; Wahl, G. H. *J. Am. Chem. Soc.* **1963**, 85, 1199-1200.

(108) Soper, A. K.; Benmore, C. J. *Phys. Rev. Lett.* **2008**, 101, 065502.

(109) Juodkazis, K.; Juodkazytė, J.; Vilkauskaitė, R.; Jasulaitienė, V. *J. Solid State Electrochem.* **2008**, 12, 1469-1479.

(110) Bocca, C.; Barbucci, A.; Cerisola, G. *Int. J. Hydrogen Energy* **1998**, 23, 247-252.

(111) Mom, R. V.; Cheng, J.; Koper, M. T. M.; Sprik, M. *J. Phys. Chem. C* **2014**, 118, 4095-4102.

(112) Llewellyn, J. A.; Robertson, R. E.; Scott, J. M. W. *Can. J. Chem.* **1960**, 38, 222-232.

(113) Shiner, V. J.; Humphrey, J. S. *J. Am. Chem. Soc.* **1963**, 85, 2416-2419.

(114) Collins, C. J.; Bowman, N. S. *Isotope Effects in Chemical Reactions*; Van Nostrand Reinhold: New York, 1970.

(115) Jewett, J. G.; Dunlap, R. P. *J. Am. Chem. Soc.* **1968**, 90, 809-810.

(116) Clough, S. A.; Beers, Y.; Klein, G. P.; Rothman, L. S. *J. Chem. Phys.* **1973**, 59, 2254-2259.

(117) Brittain, A. H.; Cox, A. P.; Duxbury, G.; Hersey, T. G.; Jones, R. G. *Mol. Phys.* **1972**, 24, 843-851.

(118) Cibrev, D.; Jankulovska, M.; Lana-Villarreal, T.; Gómez, R. *Int. J. Hydrogen Energy* **2013**, 38, 2746-2753.

(119) Fletcher, S. *J. Solid State Electrochem.* **2008**, 13, 537-549.

(120) Bakac, A. *Physical Inorganic Chemistry: Reactions, Processes, and Applications*; Wiley: New Jersey, 2010.

Chapter 5

Nano Porous Copper Films by Additive-Controlled Electrodeposition: CO_2 Reduction Catalysis

The work in this chapter was accomplished in collaboration with Sichao Ma, Jake I. Gold, Professor Paul J.A. Kenis, and Professor Andrew A. Gewirth.

5.1. Introduction

In a transition from fossil fuels to renewable energy, electrochemical energy conversion and energy storage play a critical role. A key challenge to commercializing electrochemical energy conversion and storage systems is developing electrocatalysts with low cost, high activity, and high stability.[1] Many studies have focused on designing and controlling morphology and compositions of either bulk catalyst (foil, disk, foam)[2-4] or nano particle catalyst[1,4-7]. While a bulk catalyst is easy to obtain, its activity is low due to the intrinsically small active surface area. Nanoparticles, while useful for schemes that seek to minimize precious metal usage and increase active surface area, are harder to fabricate, and require a binder when utilized in a real electrolyzer, the presence of which can inhibit reactivity, particularly when accompanied by substantial gas and/or product evolution.[8,9]

Recently, we fabricated Ni and NiFe catalysts for the oxygen evolution reaction (OER) by electrodepositing these materials in the presence of 3,5-diamino-1,2,4-triazole (DAT) as a deposition additive. The resulting nanostructured electrodeposit is a very active catalyst for OER.[10] However, these 'additive-controlled' electrodeposited Ni and NiFe films do not exhibit a

well-defined morphology because the electrodeposition process occurs simultaneously with vigorous H_2 evolution. We wondered whether our electrodeposition method could be used to control the morphology of a nanostructured film produced under gentler conditions. We also wondered whether our electrodeposition method could be suitable for other transition metals exhibiting electrocatalytic activity.

A promising transition metal for both electrodeposition and electrocatalysis is Cu. Cu has long history of electrodeposition in microelectronics contexts.[11,12] Cu is also used as an electrocatalyst for CO_2 and NO_3^- reduction.[13-22] Substantial effort has been extended to fabricate Cu nanoparticles and Cu foams, some of which exhibit high catalytic activity for CO_2 reduction.[2,6,23] While nanoparticles exhibit high active surface area hence high activity, their activity and stability are limited by the requirement for a binder to adhere the particles to an electrode. Metal foams with high porosity could be a way to provide high surface area catalyst without requirement of any binder.[2,8] However, most metal foams are made by either a metallization process on a foam substrate,[24] or by electrodeposition using hydrogen bubbles as the template.[2,23,25,26] Metal foams made by metallization on foam substrate are expensive and limited to the structures of available foam substrates. While the hydrogen bubble templating method has advantages of simplicity and low cost, the presence of vigorous hydrogen bubble evolution and the fast rate of deposition under high potential or current during foam synthesis puts constraints on the tunability of the film structure, and potentially compromises film stability, particularly at high loading. [2,16, 23] A new method of fabricating metal foams for electrocatalysis applications is desired.

Electrochemical reduction of CO_2 into value-added chemicals has attracted increasing attention for decades due to its potential to facilitate a sustainable redox cycle for intermittent

renewable energy conversion and storage.[13,19,20] Among the many catalysts for CO_2 reduction, Cu is the only known metal catalyst able to generate various products – particularly hydrocarbons and oxygenates -- and tune their relative quantities and Faradaic efficiencies (FEs) by changing structure and morphology of Cu catalysts.[3,6,19,20,27-32] Recently, Cu nanofoams have been reported that showed interesting results i for CO_2 reduction.[2] These Cu nanofoams exhibited enhancement in Faradaic efficiency of HCOOH (up to 37%) than those obtained from smooth Cu. However, the main product is H_2 (50-90% FE), leading to a low total CO_2 reduction efficiency to desirable products of 10-50%. While these Cu nanofoams were shown to be highly porous, the total observed reduction current density was only 2-2.6 times higher than those obtained from smooth Cu.[2]

In this work, we exploit our electrodeposition method to synthesize Cu films with high surface area and tunable morphology. We evaluate the ability of these films as catalysts for CO_2 electrodreduction. Remarkably we find these films to be among the most active for CO_2 reduction on a Cu catalyst.

5.2. Experimental section

5.2.1. Electrodeposition of metal

The Cu plating baths were made from 0.1 M $CuSO_4.5H_2O$ and 10 mM of additive, pH adjusted between pH 1-3 by using H_2SO_4. Additives tested were 3,5-diamino-1,2,4-triazole (DAT), dodecyltrimethyl ammonium bromide (DTAB), and thonzonium bromide (ThonB - hexadecyl-[2-[(4-methoxyphenyl)methyl-pyrimidin-2-ylamino]ethyl]-dimethylazanium bromide), all of which were obtained from Sigma Aldrich. Cu was electrodeposited galvanostatically at a constant current density ranging from 1 - 4 mA/cm^2 until a final deposition

charge was reached (typically 2 C/cm^2, unless otherwise stated). Pt wire was used as the counter electrode. The counter electrode was separated from the working electrode by using an ion exchange membrane (Fumatech® FAP-375-PP) in a two compartment electrochemical cell to avoid oxidation of additives at the counter electrode. A 'leakless' Ag/AgCl (eDAQ) electrode was placed near the working electrode to measure the potential.

Substrates for electrodeposition were cleaned just before used. Au (200 nm thickness, fabricated on one side of glass coverslips by e-beam deposition) was rinsed with Milli-Q water, and then flamed under H_2. Cu foil (Sigma Aldrich, thickness 0.125 mm, purity 99.9) was rinsed thoroughly with Milli-Q water. Carbon paper (GDL, Sigracet 35 BC, Ion Power) was activated either by immersing in conc. HNO_3 for 1h or sputter coated with ~ 10 nm of Cu (~ 0.01 mg/cm^2). Carbon paper pretreated by both methods exhibits similar morphologies and electrochemical activities.

For flow cell electrolysis experiments, Cu was electrodeposited on carbon paper and used as a gas diffusion electrode. However, HNO_3 treatment makes both side of the carbon paper become hydrophilic and allows liquid to easily pass through, which causes flooding of electrolyte into the gas chamber. Thus, the carbon paper was sputter coated with Cu instead of treated with HNO_3 before electrodeposition. Then 2 C/cm^2 of Cu was electrodeposited on the 1 × 2.5 cm^2 section of carbon paper.

5.2.2. Materials characterization

The amount of Cu electrodeposited was measured by ICP-OES (PerkinElmer 2000 DV optical emission spectrometer). Scanning electron microscope (SEM) images were obtained from a Hitachi A-4700 high resolution microscope. X-Ray Photoelectron Spectroscopy (XPS) was performed with a Physical Electronics PHI 5400. The thickness of the electrodeposited film was measured by surface profilometry (Sloan Dektak).[3]

5.2.3. Electrochemical measurements for CO_2 reduction

Cyclic voltammetry (CV), chronoamperometry (CA), and chronopotentiometry (CP) evaluating CO_2 reduction were performed at room temperature using a CHI 760D or Biologic SP-150 potentiostat with a Pt mesh counter electrode and an Ag/AgCl reference electrode. Before the electrochemical measurement, the electrolyte (1 M $KHCO_3$) was saturated with CO_2. The Ag/AgCl reference electrode was calibrated before each experiment with a normal hydrogen electrode (NHE) in 1M $HClO_4$. Potentials are reported with respect to reversible hydrogen electrode (RHE), unless otherwise stated. All voltammetry data was IR corrected. Flow cell measurements and product characterization were performed as previously reported.[6]

5.3. Results and discussion

5.3.1. Effects of additives on Cu deposition

Figure 5.1a shows CVs obtained from Au substrates in solutions containing 0.1 M $CuSO_4$ at pH 2 with and without 0.01 M of different additives. In absence of the additive, the voltammetry shows a strong cathodic feature commencing at ~ 0.11 V vs. RHE associated with the onset of

bulk Cu deposition. Upon addition of 0.01 M DAT, Cu deposition is inhibited until a potential of -0.18 V vs. RHE is reached (η = 0.25 V). The reverse scan exhibits negligible hysteresis, showing that the inhibitor does not break down at negative potentials. At positive potentials, voltammetry obtained in absence of DAT shows a substantial anodic feature associated with oxidation of the deposited Cu. Addition of DAT leads to a slightly higher overpotential for Cu oxidation, indicating that DAT is adsorbed on the surface at these potentials.

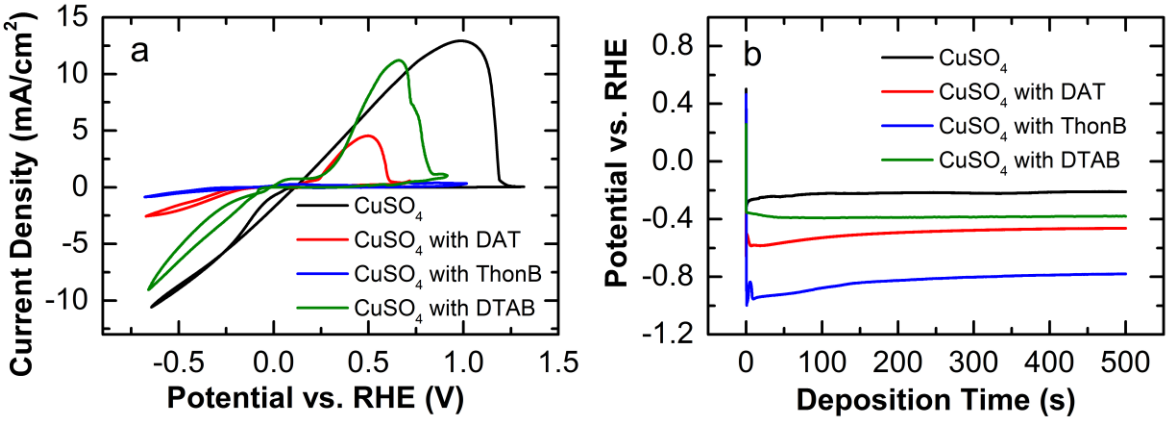

Figure 5.1. Influence of additives (a) on the CV of Cu redox reaction (scan rate 10 mV/s), and (b) on the Chronopotentiometry at – 4 mA/cm^2 of a Au substrate in a copper electrodeposition bath of 0.1 M $CuSO_4$ at pH 2 with and without 0.01 M additives (DAT, ThonB, DTAB).

Figure 5.1b shows the electrodeposition profile of Cu on Au substrates in solutions containing 0.1 M $CuSO_4$ at pH 2 with and without DAT for 500 seconds. A deposition current of – 4 mA/cm^2 was maintained at ~ -0.2 V without DAT and -0.5 V vs. RHE with DAT. CP and CV both indicate that DAT inhibits Cu deposition. ICP-OES data shows that the Coulombic efficiency of Cu electrodeposited in the additive-free solution is ~ 80 %, while the Coulombic efficiency of Cu electrodeposited with DAT is 44 ± 5 %. The low deposition efficiency of solutions containing DAT once again indicates that DAT inhibits Cu electrodeposition.

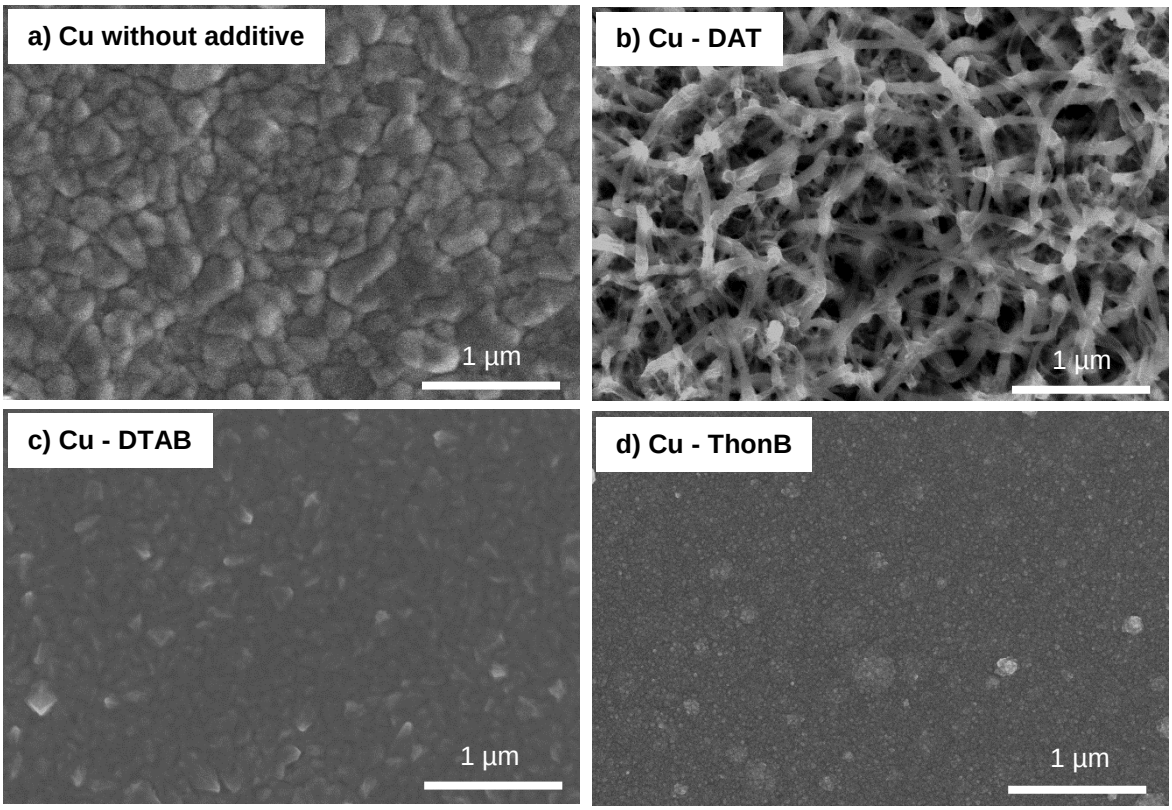

Figure 5.2. SEM of Cu electrodeposited (a) without additive, (b) with DTAB, and (c) with ThonB.

Upon the addition of ThonB and DTAB, Cu deposition is inhibited at an overpotential of 0.35 V and 0.15 V, respectively.[33] ThonB exhibits the strongest inhibitive effect on Cu deposition among the three additives, showing both a large overpotential and low deposition/stripping current density. In contrast, DTAB exhibits a higher current density and a lower overpotential for deposition onset.

Figure 5.2 shows SEM micrographs of Cu films electrodeposited with and without additives. Interestingly, while the Cu films electrodeposited with DAT (Figure 5.2b) exhibit a rough and porous surface, Cu films electrodeposited without additive (Figure 5.2a), with DTAB (Figure 5.2c), and with ThonB (Figure 5.2d) all exhibit smooth surfaces. In the presence of DTAB and

ThonB, Cu films exhibit an even smoother surface than in the absence of additives. All three additives inhibit Cu deposition, but ThonB and DTAB apparently act as deposition levelers as expected,[33] while DAT addition results in a rough surface. Interestingly, while UV-vis spectra obtained from solutions containing DAT and Cu exhibit the presence of what is likely a Ligand-to-metal Charge Transfer (LMCT) band confirming DAT-Cu coordination, such a feature is not present for solutions containing either DTAB or ThonB and Cu (Figure 5.3). The more facile coordination between Cu and DAT likely results from the presence of N coordination sites in DAT that are absent in the other two additives. Thus, while all three additives inhibit Cu deposition, only DAT coordinates to Cu, inhibiting surface diffusivity.

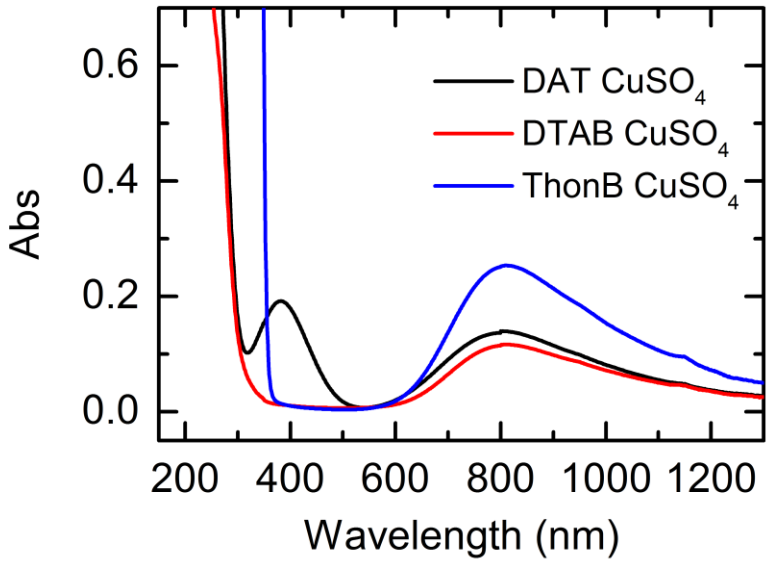

Figure 5.3. UV-Vis spectra of 10 mM $CuSO_4$ and 10 mM additive (DAT, or DTAB, or ThonB) solutions.

5.3.2. Effects of pH and deposition current on electrodeposition of Cu with DAT

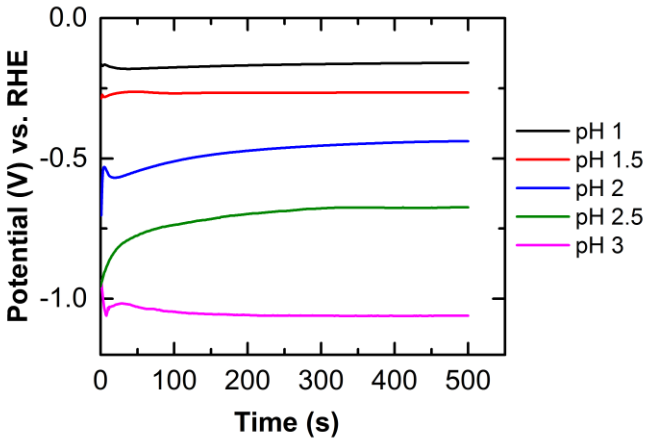

Figure 5.4. Influence of pH on deposition of Cu on Au substrate in electrodeposition bath containing 0.1 M $CuSO_4$ + 0.01 M DAT at i = -4 mA/cm^2.

In order to evaluate the effect of DAT protonation on Cu electrodeposition, we examined Cu deposition with DAT at different pH values. Figure 5.4 shows the electrodeposition profile of Cu on Au substrates in solutions containing 0.1 M $CuSO_4$ and 0.01M DAT at pH = 1, 1.5, 2, 2.5, and 3, values less than the pK_a of DAT = 4.43.[34] Increasing the pH from 1 to 3 resulted in an increase of ~ 0.9 V in deposition potential. This phenomenon suggests that inhibition of DAT increases with increasing pH. A solution of 0.1 M $CuSO_4$ and 0.01M DAT at pH 1 exhibits a blue color similar to that found in a solution containing $CuSO_4$ without DAT. As the pH is raised from pH 1 to pH 3, the color of the solution changes from blue to green. Additionally, the solution starts to become cloudy at pH 3, indicating the presence of precipitates in the solution. Thus, the increased inhibition of DAT with increasing pH likely results from more facile formation of Cu-DAT complexes, a result corroborated by UV-vis spectroscopy (Figure 5.5). Deposition solutions at pH higher than 3 did not yield reproducible and uniform deposits.

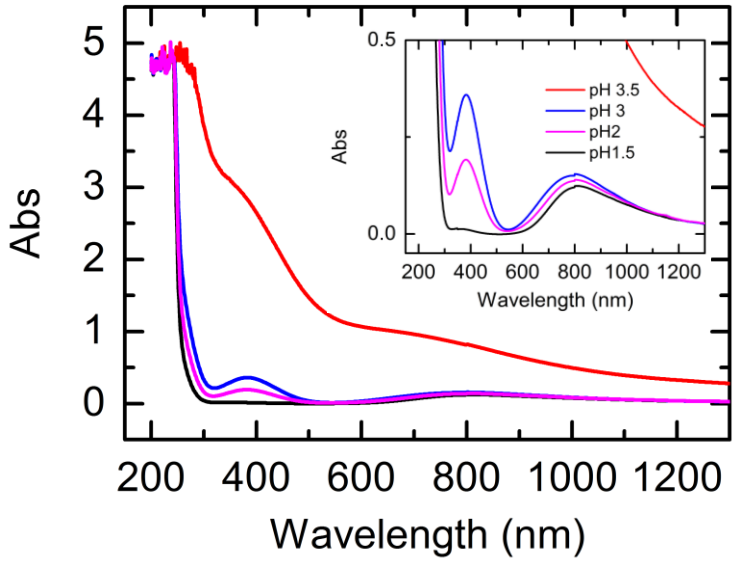

Figure 5.5. UV-Vis spectra of 10 mM $CuSO_4$ and 10 mM DAT solutions at different pHs.

Figure 5.6 shows SEM micrographs of Cu electrodeposits obtained with DAT at (a) pH 2.5 at -4 mA/cm^2, (b) pH 2.5 at -8 mA/cm^2, (c) pH 1.5 at -4 mA/cm^2, (d) pH 1.5 at -8 mA/cm^2, (e) pH 1 at -4 mA/cm^2, and (f) pH 1 at -8 mA/cm^2. Clearly different types of deposits are formed as a function of different pH and current density. At pH 2.5, the Cu deposit exhibits particles of ill-defined shape at deposition currents of -4 and -8 mA/cm^2 (Figure 5.6a, b). At pH 1.5 (Figure 5.6c, d), the deposit exhibits a wire-like shape, with wire diameters of 50-70 nm. At pH 1 the Cu films exhibit a dot shape (Figure 5.6f) or a mixture of wire and dot shapes (Figure 5.6e). Thus, pH has a strong effect on nanostructure shape and density of the whole film, a result likely explained by the differences in Cu coordination at these different pH values. At low pH where the deposited Cu particles exhibit a well-defined shape (pH 1.5 and pH 1), deposition currents show clear effects on particle size. Comparing the Cu film deposited at 4 mA/cm^2, pH 1 (Figure 5.6c) and the one deposited at 8 mA/cm^2, pH 1 (Figure 5.6d), the Cu film deposited at 4 mA/cm^2 shows larger and longer wire-like particles than the film deposited at 8 mA/cm^2. This result suggests that higher

deposition currents increase the nucleation density of Cu, resulting in smaller size Cu nanostructures.[35]

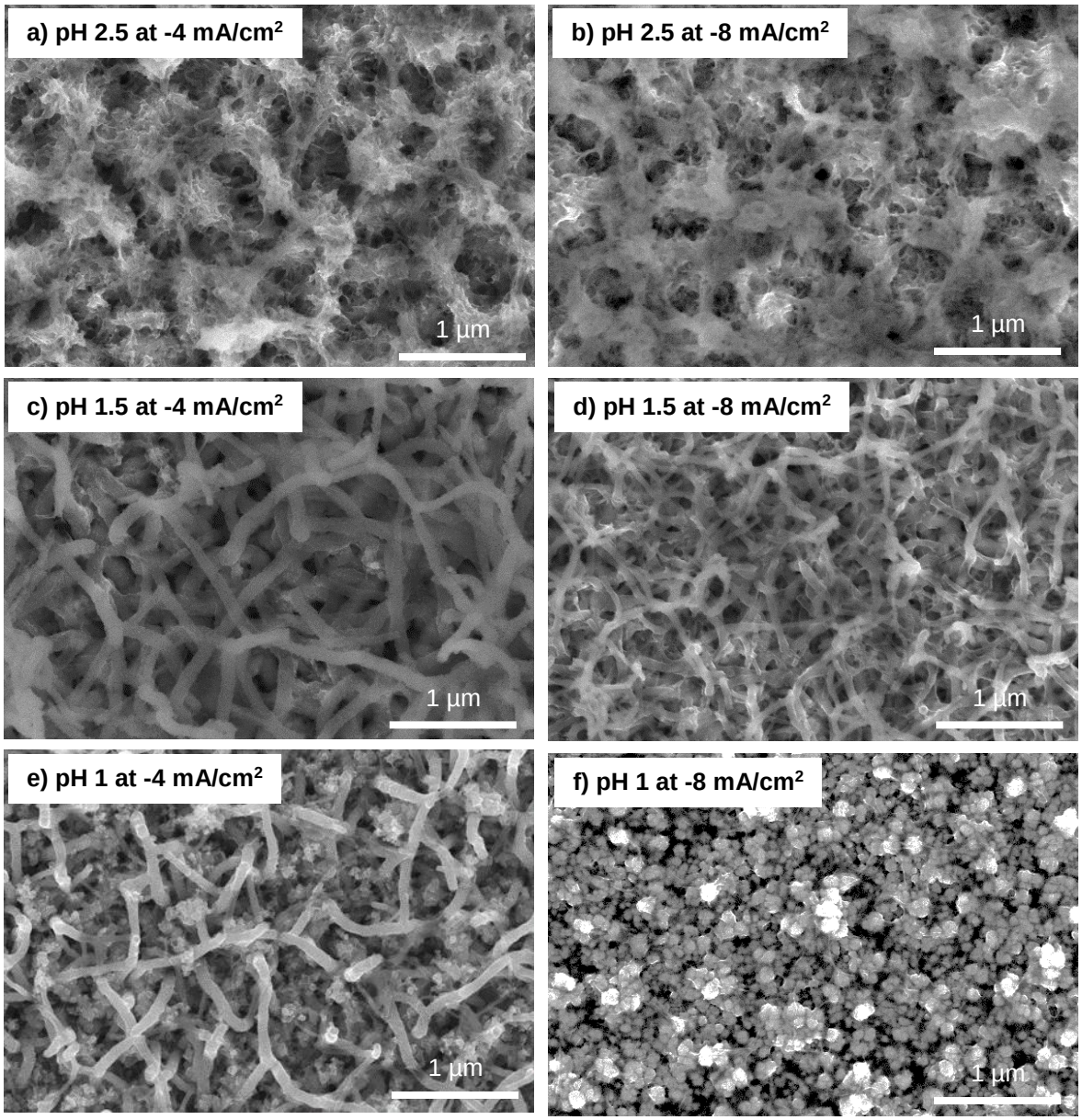

Figure 5.6. SEM micrographs of Cu film deposited in 0.1 M CuSO4 and 0.01M DAT solution at (a) pH 2.5 at -4 mA/cm^2, (b) pH 2.5 at -8 mA/cm^2, (c) pH 1.5-2 at -4 mA/cm^2, (d) pH 1.5-2 at -8 mA/cm^2, (e) pH 1 at -4 mA/cm^2, (f) pH 1 at -8 mA/cm^2.

The mechanism by which DAT modifies the electrodeposition process to yield the rough and porous Cu surfaces observed can be explained by invoking a diffusion-limited aggregation

(DLA) process,[36-38] similar to what we reported for NiDAT and NiFeDAT deposits recently.[10] In the Cu case, DAT binds to the substrate surface, reducing the number of nucleation sites for Cu deposition, thus initiating roughness. These rough areas experience a high local current density and grow exponentially, while other areas are still DAT-covered and diffusion inhibited. The growth of the deposit is further inhibited by the coordination of DAT to Cu, limiting subsequent diffusion both before and after reduction. As shown above, the inhibition of DAT is controlled by changing the pH of the deposition solution along with the deposition current density.

In the previously reported NiDAT and NiFeDAT cases,[10] the high surface roughness arises as a consequence of both inhibition of electrodeposition by DAT and H_2 adsorption on the electrode surface. In the Cu case studied here, however, the high surface roughness involves only DAT coordination, without formation and adsorption of H_2. The absence of vigorous H_2 bubbling during CuDAT electrodeposition could explain why cracks – clearly in evidence with the NiDAT and NiFeDAT films[10] – are not found in the Cu films reported here.

Through SEM images of the electrodeposited films obtained from different pH and different deposition current density, we found that by controlling these parameters, we could control the morphology of the Cu films. When the pH decreases from 2.5 to 1, DAT association to the substrate surface is weaker resulting in a dense film with larger particle sizes relative to films deposited at higher pH (Table 5.1). At pH 2.5 (Figure 5.6e and 5.6f), DAT binds strongly on the substrate surface, resulting in smaller particle size (Table 5.1). However, Cu and Cu oxides formed at the same time at this pH caused ill-defined shape of the film. At higher current density, the growth is faster so thinner wire structures are obtained. The morphology of the CuDAT films is not dependent on substrates.

5.3.3. Characterization of Cu films

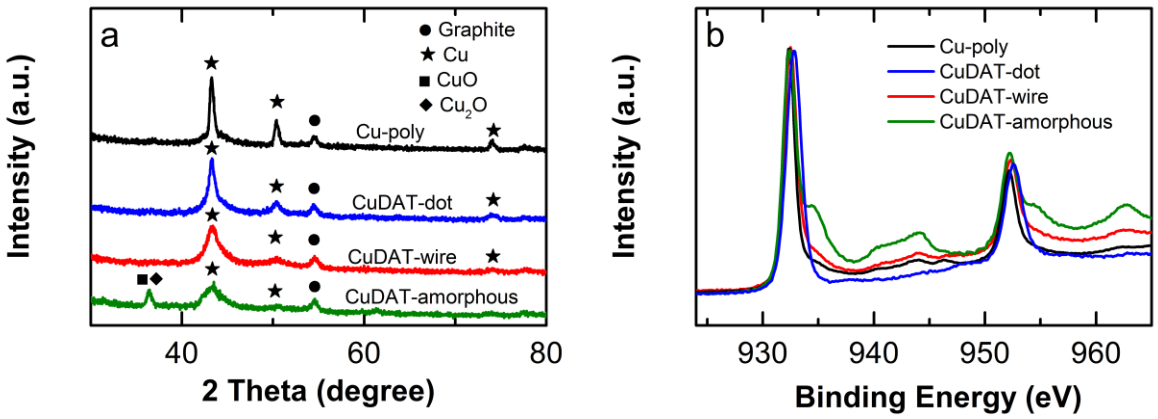

Figure 5.7. (a) XRD and (b) XPS patterns of Cu-poly, and CuDAT-dot, CuDAT-wire, and CuDAT-amorphous.

Figure 5.7a shows the XRD patterns of Cu-poly electrodeposited without DAT, as well as CuDAT-dot, CuDAT-wire, and CuDAT-amorphous, all electrodeposited with DAT. While Cu-poly, CuDAT-dot, and CuDAT-wire samples show only Cu peaks at $2\theta = 43.46^{o}$ (from Cu (111)), 50.62^{o} (from Cu (200)), and 74.40^{o} (from Cu (220)), CuDAT-amorphous samples electrodeposited at higher pH than other samples show an extra peak at $2\theta \approx 36^{o}$, which is associated with Cu oxides (Cu2O and/or CuO). The presence of Cu oxides in CuDAT-amorphous is also evident from a series of satellite peaks[39-41] in the XPS pattern shown in Figure 5.7b.

The Cu peaks in XRD patterns of CuDAT samples are broader and lower intensity than Cu-poly sample, indicating that CuDAT samples exhibit a smaller crystallite size than Cu-poly. The specific crystallite size of each sample, determined by the Scherer equation, is summarized in Table 5.1. The density (loading/ (area × thickness)) of Cu-poly samples is similar to Cu foil. In contrast, the density of CuDAT-dot samples is ~ 50% of the Cu foil density, while the density of CuDAT-wire and CuDAT-amorphous is ~ 18% of that of Cu foil. The electro-active surface area

of the different Cu samples was measured by using Pb underpotential deposition (PbUPD) to form a conformal coat on the accessible Cu deposit.[42,43] The results (Table 5.1) show that the Cu-poly sample electrodeposited without DAT exhibits a PbUPD charge similar to that from Cu bulk samples, i.e., the electro-active surface area is close to the geometric area.[43] The CuDAT samples exhibit a higher active surface area than Cu-poly, while the CuDAT-wire samples exhibit the highest active surface area among tested samples, around 7 times higher than the Cu-poly samples.

The low density and high surface areas found for the CuDAT samples suggest that they could be considering thin metallic foams. However, pore density and pore size are difficult to determine for these materials. The active surface area of these materials is significantly higher than their geometric area, suggesting that these materials are open-cell foams, which allow gas and electrolyte to transfer through the material to interact with deeper layers.

Table 5.1. Parameters of Cu samples obtained from 0.1 M $CuSO_4$ deposition baths.

Name	DAT mM	pH	I_{depo} mA/cm^2	Morphology	Loading[1] mg/cm^2	Thickness[2] µm	Density[3] g/cm^2	Crystallite size[4] nm	$\frac{A_{active}}{A_{geometric}}$ [5]
Cu foil	-	-	-	smooth	-	-	8.96	-	1
Cu-poly	-	2.0	-4	smooth	0.53±0.03	0.60±0.05	~.8.8	19.5±3.0	~1
CuDAT-amorphous	10	2.5	-4	amorphous	0.29+0.04	180±0.25	~ 1.6	2.2±15	~6
CuDAT-dot	10	1.0	-8	dot	0.31±0.03	0.70±0.10	~ 4.4	9.5±13	~5
CuDAT-wire	10	1.5	-4	wire	0.28±0.03	1.75±0.20	~ 1.6	4.6±9	~7

[1] Loading measured by ICP-OES

[2] Thickness of electrodeposited film was measured by surface profilometry

[3] Density was calculated from loading per cm^2 and thickness of the film

[4] Crystallite size was calculated from XRD patterns using the Scherer equation

[5] Active surface area was calculated from Lead UPD experiments

5.3.4. CO_2 reduction reaction activity of Cu films in H-cell

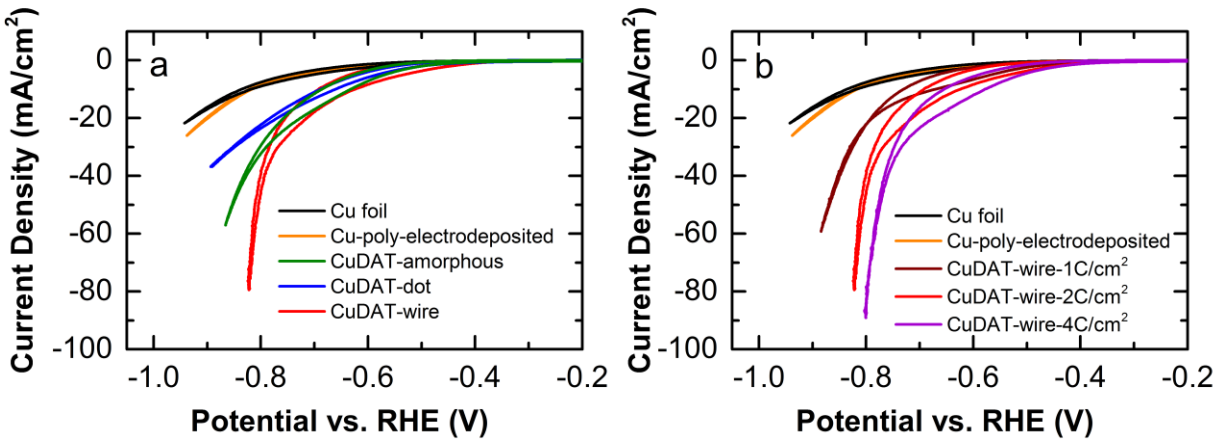

Figure 5.8. CV in H-cell at a scan rate 50 mV/s (iR corrected) in 1 M $KHCO_3$ saturated with CO_2 (a) from Cu foil, Cu-poly electrodeposited without DAT, CuDAT-dot, CuDAT-amorphous and CuDAT-wire; and (b) Cu foil, Cu film electrodeposited without DAT, and CuDAT-wire samples with a deposition charge of 1 C/cm^2, 2 C/cm^2, 4 C/cm^2.

Open-cell metallic foam is known to increase the catalytic activity of electrochemical systems due to their high surface area and permeability.[44,45] We evaluated the catalytic activity of our CuDAT samples for CO_2 reduction reaction. Figure 5.8a shows an iR corrected CV obtained from Cu and CuDAT samples in 1 M $KHCO_3$ saturated with CO_2 using an electrochemical H-cell. Reduction currents are associated with CO_2 reduction and H_2 evolution. The Cu foil and Cu-poly films electrodeposited without DAT (control samples) exhibit low activity in this potential region. In contrast, CuDAT samples exhibit lower onset and much higher reduction currents than the Cu-poly or Cu foil. CuDAT samples exhibit reduction onset at around -0.6V vs. RHE, while the onset of the Cu-poly and Cu foil are around -0.8V vs. RHE. The CuDAT-wire sample exhibits the highest reduction current density. Stability tests show that CuDAT samples maintain their catalytic activity for at least 8 hours (Figure 5.9).

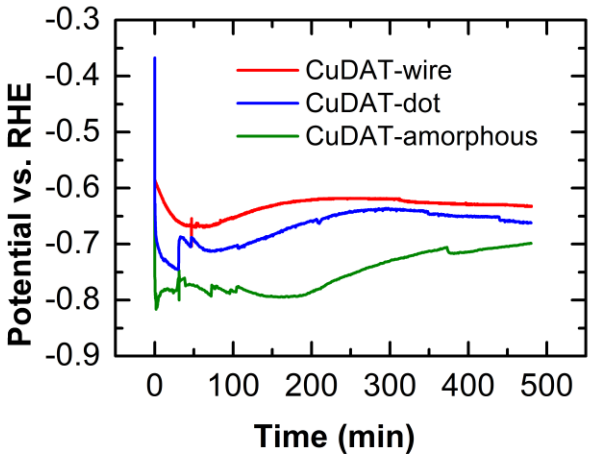

Figure 5.9. Stability test of Cu electrodeposited without DAT, CuDAT-dot and CuDAT-wire at 30mA/cm^2 in 1M $KHCO_3$ continuously sparged with CO_2.

The increased activity of the CuDAT samples compared to the Cu-poly sample might be explained by the increase in surface area of the catalysts. In particular, the current density exhibited by the CuDAT-wire sample is 6 times (at low potential) to 9 times (at high potential) larger than the current density from Cu-poly. The overall increase is consistent with the Pb_{upd} measurements where the active surface of the CuDAT-wire sample is shown to be 7 times larger than that of the Cu-poly. The small mismatch here suggests that (a) the current densities of the catalysts are dependent on not only surface area, but also on diffusion of CO_2 in and products out of catalyst (which is different with different catalysts and different at different potentials) and/or (b) Pb_{upd} is not a perfect method with which to measure surface area for porous materials (In particular, Pb diffusion is slow and the lower Pb concentration in confined areas might result in a shifting potential for upd).[46]

Next we evaluated the effects of Cu loading on the CO_2 reduction rate. Figure 5.8b shows that a Cu-poly electrodeposited without DAT and Cu foil both exhibit similar CO_2 reduction activity, indicating that CO_2 reduction is a surface process and independent of Cu film thickness.

However, the CO_2 reduction activity of CuDAT-wire samples is related to the deposition charge, *i.e.*, Cu loading. Figure 5.8b shows that as the loading is increased (from 1 C/cm^2 to 4 C/cm^2), the CO_2 reduction current density also increases. This behavior suggests that the surface area of the CuDAT-wire film increases while they maintain porosity and permeability with high loading. CuDAT-wire reaches -90 mA/cm^2 at ~ -0.8 V vs. RHE, which is 6-10 times higher than the current density observed for Cu foam catalysts reported previously.[2,23]

5.3.5. CO_2 reduction reaction activity and product distribution of Cu films in a flow cell

To evaluate the gas permeability of the CuDAT film and the relationship between its catalytic activity and product distribution during CO_2 reduction, we also tested CuDAT samples in a flow cell.[6] Figure 5.10 shows the Faradaic efficiency (FE) and partial current density for total CO_2 reduction and all major products (CO, C_2H_4, and C_2H_5OH) using Cu-poly electrodeposited without DAT, CuDAT-amorphous, CuDAT-dot, and CuDAT-wire in a 1 M KOH electrolyte as a function of cathode potential. In this study the CuDAT-wire sample exhibits a relatively high total CO_2 reduction current density as well as partial current density and FE for CO, C_2H_4, and C_2H_5OH at low cathode overpotentials.

Furthermore, CuDAT-wire exhibits a higher total CO_2 reduction FE and current density relative to CuDAT-amorphous, CuDAT-dot, and Cu-poly (Figure 5.10a, 5.10b). During CO_2 reduction measurements the CuDAT-wire (with high porosity, low density, see Figure 5.11d) little or no gas bubbles emerged from the electrolyte chamber, suggesting that the CuDAT-wire samples have good gas permeability for CO_2 into and products out of the electrolyte chamber. Cu-poly samples, in which particles do not cover the whole electrode surface (Figure 5.11a), also show good gas permeability. However, a large portion of the current is associated with H_2 evolution

and non-Faradic processes from that part of the carbon substrate not covered by the Cu-poly catalyst, leading to low total FE in this case. Both CuDAT-amorphous and CuDAT-dot catalysts cover the whole electrode surface as a low porosity film (Figure 5.11b and 5.11c). Consequently, these materials have poor gas permeability, which explains both the low CO_2 reduction current and low FE these catalysts relative to the CuDAT-wire films.

Figure 5.10c and 5.10d shows that for all catalysts, CO formation starts at ~ -0.2V and increases at more negative cathodic overpotentials. The FE for CO of CuDAT-wire and CuDAT-amorphous reaches a maximum value of ~ 40% at ~ -0.3V vs. RHE, which is much better than that found for the Cu-poly and CuDAT-dot samples. At potentials < -0.3 V the FE for CO production decreases while the FEs associated with C2 products including C_2H_4 (Figure 5.10e, 5.10f) and C_2H_5OH (Figure 5.10g, 5.10h) starts to increase. A possible explanation for this trend is that adsorbed CO is an important intermediate for the formation of C2 products, as has been suggested previously.[6,18-20,47,48] The FE for C_2H_4 production (Figure 5.10e) for the CuDAT-wire catalyst reaches and maintains a maximum value of 41% at a potential of –0.47V vs. RHE, which is a higher FE at a smaller overpotential relative to what is observed for the other Cu samples considered here. The CuDAT-wire catalyst also exhibits the highest FE and current density for C_2H_5OH production (Figure 5.10g) at lower overpotential than the other catalysts. The high activity for C2 products of CuDAT-wire is comparable to Cu-Cu oxide nanoparticle catalysts we reported recently[6], and at least one order of magnitude higher than what is found when using other Cu catalysts under similar potentials and conditions.[2,3,30,49] Interestingly, the CuDAT samples utilized here feature about three times lower Cu loading (~ 0.3 mg/cm^2) relative to the loadings utilized in other Cu systems (typically ~ 1 mg/cm^2) suggesting that the mass activity of the CuDAT systems studied here is very high.[3,5] In particular the mass activity for CO_2 reduction of CuDAT-

wire at -0.65V vs. RHE is ~ 720 A per gram of Cu, which to the best of our knowledge is among the best mass activities found from a Cu catalyst performing CO_2 reduction.

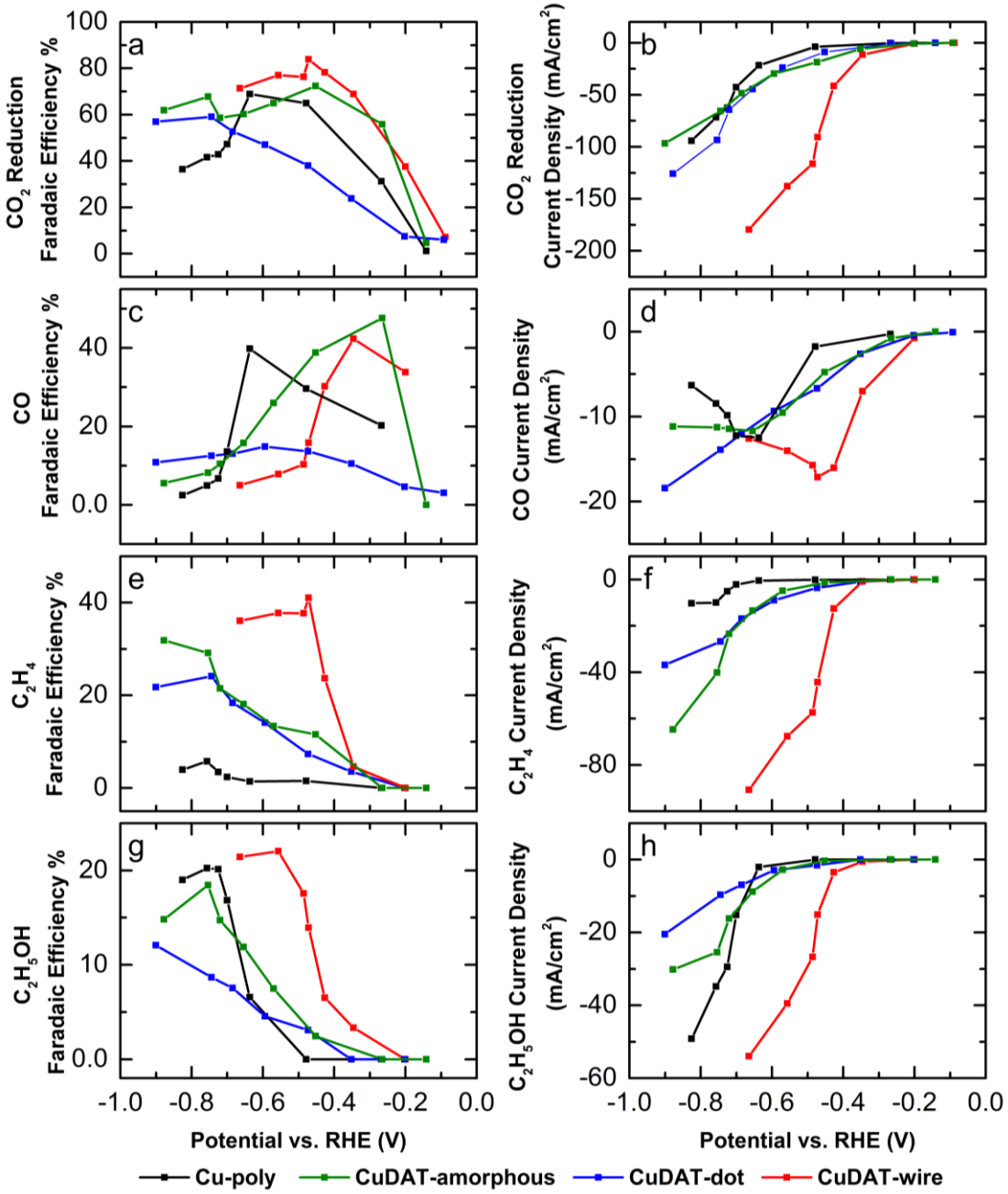

Figure 5.10. Faradaic efficiencies and corresponding current densities for (a,b) total CO_2 reduction, (c,d) CO production, (e,f) C_2H_4 production, and (g,h) C_2H_6OH production. Electrolyte 1 M KOH in electrolysis flow cell.

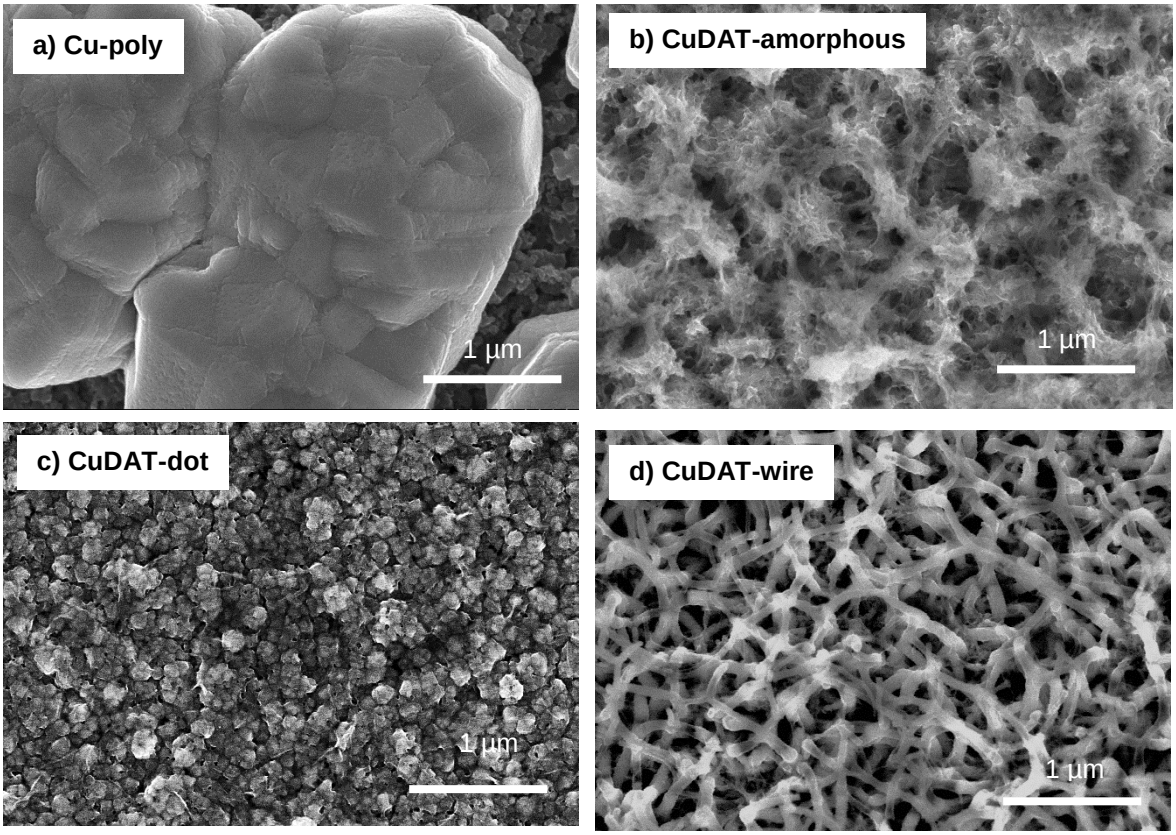

Figure 5.11. SEM of a) Cu-poly electrodeposited without DAT, b) CuDAT-amorphous, c) CuDAT-dot, and d) CuDAT-wire electrodeposited with DAT on carbon paper.

While the enhancement in current density of the CuDAT samples compared to the Cu-poly sample is related to the larger surface areas of the former, the enhancement in C2 product formation (both FE and current density) probably can be explained by the effect of 'nanosize' CuDAT particles. The nano porous CuDAT surfaces give rise to steps and edges with low-coordinated Cu atoms which have been postulated to be more active toward the reduction of CO_2 to C2 products: Steps and edges promote adsorption of C1 intermediates and facilitate their dimerization to form C2 products.[3,19,47,50-52]

5.4. Conclusion

We developed a facile method to electrodeposit high surface area Cu films onto conductive substrates. Our method relies on the inhibition of nucleation through the presence of an additive, DAT, the degree of which is controlled by pH and current density. The films exhibit active areas many times larger than that found absent the deposition additive. In contrast to porous Cu films made by exploiting H_2 bubbling during electrodeposition, our films exhibit small and stable pores and the resulting structures are tunable depending on deposition conditions. We showed that the electrodeposited Cu films exhibit high activity for CO_2 reduction, resulting in facile production of C_2H_4 and C_2H_5OH. Moreover, the films are stable and maintain their activity over a several hour timescale. Mass activity for CO_2 reduction of CuDAT-wire is as high as 720 A/g at -0.65 V vs. RHE. While we focused on CO_2 reduction activity here, the ability to tune the nature of the Cu electrodeposit raises interesting possibilities to control and enhance the (electro) catalytic activity of other metals.

5.5. References

(1) Guo, Y. G.; Hu, J. S.; Wan, L. J. *Advanced Materials* **2008**, *20*, 4384-4384.

(2) Sen, S.; Liu, D.; Palmore, G. T. R. *ACS Catalysis* **2014**, *4*, 3091-3095.

(3) Tang, W.; Peterson, A. A.; Varela, A. S.; Jovanov, Z. P.; Bech, L.; Durand, W. J.; Dahl, S.; Norskov, J. K.; Chorkendorff, I. *Physical Chemistry Chemical Physics* **2012**, *14*, 76-81.

(4) Zhu, S. Q.; Shao, M. H. *Journal of Solid State Electrochemistry* **2016**, *20*, 861-873.

(5) Feng, X. F.; Jiang, K. L.; Fan, S. S.; Kanan, M. W. *ACS Central Science* **2016**, *2*, 169-174.

(6) Ma, S. C.; Sadakiyo, M.; Luo, R.; Heima, M.; Yamauchi, M.; Kenis, P. J. A. *Journal of Power Sources* **2016**, *301*, 219-228.

(7) Mistry, H.; Varela, A. S.; Kuhl, S.; Strasser, P.; Cuenya, B. R. *Nature Reviews Materials* **2016**, *1*.

(8) Ji, J. Y.; Zhang, L. L.; Ji, H. X.; Li, Y.; Zhao, X.; Bai, X.; Fan, X. B.; Zhang, F. B.; Ruoff, R. S. *ACS Nano* **2013**, *7*, 6237-6243.

(9) Garg, G.; Basu, S. *Electrochimica Acta* **2015**, *177*, 359-365.

(10) Hoang, T. T. H.; Gewirth, A. A. *ACS Catalysis* **2016**, *6*, 1159-1164.

(11) Andricacos, P. C.; Uzoh, C.; Dukovic, J. O.; Horkans, J.; Deligianni, H. *Ibm Journal of Research and Development* **1998**, *42*, 567-574.

(12) Schlesinger, M.; Paunovic, M. *Modern electroplating*; 5th ed.; Wiley: Hoboken, NJ, 2010.

(13) Lim, R. J.; Xie, M. S.; Sk, M. A.; Lee, J. M.; Fisher, A.; Wang, X.; Lim, K. H. *Catalysis Today* **2014**, *233*, 169-180.

(14) Kapoor, A.; Viraraghavan, T. *Journal of Environmental Engineering-ASCE* **1997**, *123*, 371-380.

(15) Polatides, C.; Kyriacou, G. *Journal of Applied Electrochemistry* **2005**, *35*, 421-427.

(16) Gattrell, M.; Gupta, N.; Co, A. *Journal of Electroanalytical Chemistry* **2006**, *594*, 1-19.

(17) Bouzek, K.; Paidar, M.; Sadilkova, A.; Bergmann, H. *Journal of Applied Electrochemistry* **2001**, *31*, 1185-1193.

(18) Kuhl, K. P.; Cave, E. R.; Abram, D. N.; Jaramillo, T. F. *Energy & Environmental Science* **2012**, *5*, 7050-7059.

(19) Hori, Y. In *Modern Aspects of Electrochemistry*; Vayenas, C. G., White, R. E., Gamboa-Aldeco, M. E., Eds.; Springer New York: New York, NY, 2008, p 89-189.

(20) Kortlever, R.; Shen, J.; Schouten, K. J. P.; Calle-Vallejo, F.; Koper, M. T. M. *Journal of Physical Chemistry Letters* **2015**, *6*, 4073-4082.

(21) Wu, J. J.; Zhou, X. D. *Chinese Journal of Catalysis* **2016**, *37*, 999-1015.

(22) Jhong, H. R.; Ma, S. C.; Kenis, P. J. A. *Current Opinion in Chemical Engineering* **2013**, *2*, 191-199.

(23) Dutta, A.; Rahaman, M.; Luedi, N. C.; Broekmann, P. *ACS Catalysis* **2016**, *6*, 3804-3814.

(24) Davies, G. J.; Zhen, S. *Journal of Materials Science* **1983**, *18*, 1899-1911.

(25) Zhang, W. B.; Ding, C.; Wang, A. J.; Zeng, Y. W. *Journal of the Electrochemical Society* **2015**, *162*, D365-D370.

(26) Shin, H. C.; Liu, M. L. *Chemistry of Materials* **2004**, *16*, 5460-5464.

(27) Kas, R.; Hummadi, K. K.; Kortlever, R.; de Wit, P.; Milbrat, A.; Luiten-Olieman, M. W. J.; Benes, N. E.; Koper, M. T. M.; Mul, G. *Nature Communications* **2016**, *7*.

(28) Kas, R.; Kortlever, R.; Milbrat, A.; Koper, M. T. M.; Mul, G.; Baltrusaitis, J. *Physical Chemistry Chemical Physics* **2014**, *16*, 12194-12201.

(29) Li, C. W.; Kanan, M. W. *Journal of the American Chemical Society* **2012**, *134*, 7231-7234.

(30) Manthiram, K.; Beberwyck, B. J.; Aivisatos, A. P. *Journal of the American Chemical Society* **2014**, *136*, 13319-13325.

(31) Mistry, H.; Varela, A. S.; Bonifacio, C. S.; Zegkinoglou, I.; Sinev, I.; Choi, Y. W.; Kisslinger, K.; Stach, E. A.; Yang, J. C.; Strasser, P.; Cuenya, B. R. *Nature Communications* **2016**, *7*, *12123*.

(32) Ma, M.; Djanashvili, K.; Smith, W. A. *Angewandte Chemie-International Edition* **2016**, *55*, 6679-6683.

(33) Hatch, J. J.; Willey, M. J.; Gewirth, A. A. *Journal of the Electrochemical Society* **2011**, *158*, D323-D329.

(34) Efimenko, I. A.; Shishilov, O. N. *Russian Journal of Inorganic Chemistry* **2012**, *57*, 1695-1722.

(35) Vandenbrande, P.; Winand, R. *Surface & Coatings Technology* **1992**, *52*, 1-7.

(36) Witten, T. A.; Sander, L. M. *Physical Review Letters* **1981**, *47*, 1400-1403.

(37) Godorr, S. A.; Young, B. D.; Bryson, A. W. *Chemical Engineering Communications* **1992**, *117*, 307-335.

(38) Russ, J. C. *Fractal surfaces*; Plenum Press New York 1994.

(39) Biesinger, M. C.; Lau, L. W. M.; Gerson, A. R.; Smart, R. S. C. *Applied Surface Science* **2010**, *257*, 887-898.

(40) Zhu, C. Q.; Osherov, A.; Panzer, M. J. *Electrochimica Acta* **2013**, *111*, 771-778.

(41) Yin, M.; Wu, C. K.; Lou, Y. B.; Burda, C.; Koberstein, J. T.; Zhu, Y. M.; O'Brien, S. *Journal of the American Chemical Society* **2005**, *127*, 9506-9511.

(42) Wu, G. Y.; Bae, S. E.; Gewirth, A. A.; Gray, J.; Zhu, X. D.; Moffat, T. P.; Schwarzacher, W. *Surface Science* **2007**, *601*, 1886-1891.

(43) Yu, L.; Akolkar, R. *Journal of the Electrochemical Society* **2016**, *163*, D247-D249.

(44) Lefebvre, L. P.; Banhart, J.; Dunand, D. C. *Advanced Engineering Materials* **2008**, *10*, 775-787.

(45) Giani, L.; Groppi, G.; Tronconi, E. *Industrial & Engineering Chemistry Research* **2005**, *44*, 4993-5002.

(46) Liu, Y.; Bliznakov, S.; Dimitrov, N. *Journal of Physical Chemistry C* **2009**, *113*, 12362-12372.

(47) Schouten, K. J. P.; Kwon, Y.; van der Ham, C. J. M.; Qin, Z.; Koper, M. T. M. *Chemical Science* **2011**, *2*, 1902-1909.

(48) Montoya, J. H.; Shi, C.; Chan, K.; Norskov, J. K. *Journal of Physical Chemistry Letters* **2015**, *6*, 2032-2037.

(49) Kim, D.; Lee, S.; Ocon, J. D.; Jeong, B.; Lee, J. K.; Lee, J. *Physical Chemistry Chemical Physics* **2015**, *17*, 824-830.

(50) Ren, D.; Deng, Y. L.; Handoko, A. D.; Chen, C. S.; Malkhandi, S.; Yeo, B. S. *ACS Catalysis* **2015**, *5*, 2814-2821.

(51) Durand, W. J.; Peterson, A. A.; Studt, F.; Abild-Pedersen, F.; Norskov, J. K. *Surface Science* **2011**, *605*, 1354-1359.

(52) Hori, Y.; Takahashi, I.; Koga, O.; Hoshi, N. *Journal of Molecular Catalysis a-Chemical* **2003**, *199*, 39-47.

Chapter 6

Nano Porous Copper-Silver Alloys by Additive-Controlled Electrodeposition for High Selectivity of CO_2 Reduction to Ethylene

The work in this chapter was accomplished in collaboration with Sumit Verma, Sichao Ma, Tim T. Fister, Janis Timoshenko, Professor Anatoly I. Frenkel, Professor Paul J.A. Kenis, and Professor Andrew A. Gewirth.

6.1. Introduction

CO_2, mostly as a result of human activities involving the burning of fossil fuels for electricity, heat and transportation, has been emitted and increased exponentially in the atmosphere. The elevated level of CO_2 in the atmosphere has been linked to many serious environmental threats including but not limited to global warming, rising sea levels, and more erratic weather patterns. A common method to decrease the CO_2 level in the atmosphere is to capture then sequester it underground or under sea,[1,2] or convert it into value-added chemicals.[1,3-5] Another method to minimize the emission of CO_2 is to utilize clean renewable energy such as wind and solar, which are attracting increasing attention. However, renewable energy output and energy consumption are intermittent, thus requiring efficient energy conversion and energy storage systems to be coupled to energy generation. A promising approach to both mitigate CO_2 levels and utilize excess electricity from renewable sources is to capture CO_2 and electrochemically reduce it to value-added chemicals or synthetic fuels.[6-8]

While Cu is the only known metal catalyst that is able to generate various products for the electroreduction of CO_2, and it is by far the most active one for generating C_2H_4 and C_2H_5OH, Cu is generally unselective. In the past few years, several studies have been focusing on tuning activities and selectivities of CO_2 reduction on Cu catalyst by changing composition and morphology of Cu catalysts.[7-20] For example, Cu_2O or "oxide-derived" Cu catalysts have been reported to enhance reduction of CO_2 to C2 products (including C_2H_4 and C_2H_5OH).[11,12,21] Single crystal Cu catalysts such as Cu(100)[22] and Cu (100) terrace surface with introduction of Cu(111) or Cu(110) steps have been also reported to promote ethylene formation.[23] Recently, many studies have reported that addition of other metals in Cu catalysts could promote adsorption of different intermediates, leading to enhancement in selectivity of CO_2 reduction toward various products; for instance, high selectivity toward CO formation on CuAg[18] and CuAu[19,20], or HCOOH formation on CuSn and CuPb,[24] or C_2H_5OH formation on CuZn.[17]

In this study, our strategy to enhance C2 production from CO_2 electroreduction focus on fabricating CuAg catalyst with nanoporous structure and low Ag contents (<10%) using additive-controlled electrodeposition method. The CuAg catalyst exhibits wire structure with large active surface and high selectivity of CO_2 reduction to C_2H_4 (~60% Faradaic efficiency - FE) and C_2H_5OH (~25% FE) at relatively low overpotential (~ -0.7V vs RHE).

6.2. Experimental section

6.2.1. Preparation of catalysts

Cu and CuAg samples were electrodeposited in a plating bath made from 0.1 M $CuSO_4.5H_2O$ + 10 mM of 3,5-diamino-1,2,4-triazole (DAT), with or without 0.5-1.5 mM Ag_2SO_4,

at pH = 1.5 adjusted by using H_2SO_4. All chemicals were obtained from Sigma Aldrich. Cu was electrodeposited galvanostatically at a constant current density of 4 mA/cm^2 until a final deposition charge of 2 C/cm^2 was reached (unless otherwise stated). Pt wire was used as the counter electrode, separated from the working electrode by using an ion exchange membrane (Fumatech® FAP-375-PP) in a two compartment electrochemical cell to avoid oxidation of additives. A 'leakless' Ag/AgCl (eDAQ) electrode was placed near the working electrode to measure the potential. Substrates for electrodeposition were cleaned or pretreated just before used.

For CO_2 reduction in flow cell measurements, Cu and CuAg were electrodeposited on carbon paper and used as a gas diffusion electrode. Carbon paper (GDL, Sigracet 35 BC, Ion Power) was activated either by immersing in conc. HNO_3 for 1h or sputter coated with ~ 10 nm of Cu (~ 0.01 mg/cm^2) before the electrodeposition step. Carbon paper pretreated by both methods exhibits similar morphologies and electrochemical activities. However, the HNO_3 treatment makes both side of the carbon paper hydrophilic, allowing liquid transport through the paper, which occasionally results in flooding of electrolyte into the gas chamber. Thus, the carbon paper coated with Cu was used as the substrate, then 2 C/cm^2 of Cu or CuAg was electrodeposited on the 1 × 2.5 cm^2 section of the coated carbon paper.

6.2.2. Materials characterization

The amount of Cu and Ag electrodeposited was measured by using a ICP-OES (PerkinElmer 2000 DV optical emission spectrometer). Scanning electron microscope (SEM) images were obtained from a Hitachi A-4700 high resolution microscope. X-Ray Photoelectron Spectroscopy (XPS) was performed with a Physical Electronics PHI 5400. The %Ag in the CuAg

samples was measured by using Energy Dispersive Spectroscopy (EDS) during SEM and by using XPS.

X-ray absorption spectroscopy was carried out at sector 9 beamline sector (BM) at the Advanced Photon Source at Argonne National Laboratory with a beam cross section of 2.6 × 0.75 mm. Samples were studied *ex situ* by layering 12 sheets of carbon paper electrodeposited with sample. All measurements were recorded in transmission mode using a double-crystal Si (111) monochromator run at 50% detuning and ion chamber detectors filled with a mixture of He/N_2.

Pb upd was used to determine electroactive surface areas.[25] Measurements were obtained from electrodeposits on both Au and carbon paper. While the results were similar between the two substrates, the error in repeat measurements was higher using the carbon paper relative to the Au substrate, presumably due to the smoother and more reproducible surface presented by the freshly flamed Au.

6.2.3. CO_2 reduction in flow cell

Electrochemical measurements and product detection were conducted in flow cell set up described previously.[11] The activity of each catalyst for CO_2 reduction was measure by controlling the cell potential (-1.6 V, -1.75 V, -2 V, -2.25 V, -2.5 V, -2.75 V, -3 V, -3.5 V) using an Autolab PGSTAT-30, EcoChemie potentiostat. The electrolyte was 1 M KOH. Potentials were reported with respect to reversible hydrogen electrode (RHE): E (vs. RHE) = E (vs. Ag/AgCl) + 0.209 V + 0.0591 V/pH × pH − η_{IRdrop}. The gaseous product stream was sampled automatically and diverted and analyzed in a gas chromatograph (Thermo Finnegan Trace GC) equipped with both the thermal

conductivity detection (TCD) and flame ionization detector (FID). The exit electrolyte containing liquid products was collected and analyzed using ^{1}H NMR technique as described previously. [11] For normal CO_2 reduction reaction, flow rate of CO_2 was set at 7 SCCM. For CO_2 reduction reaction in the presence of CO, flow rate of CO_2 and CO were 7 SCCM and 1 SCCM, respectively.

6.3. Results and discussion

6.3.1. Characterization of Cu films

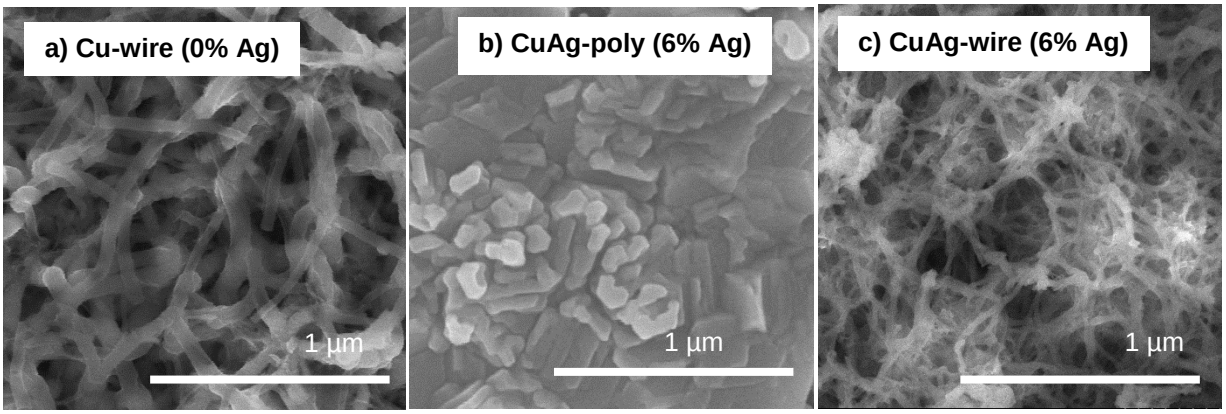

Figure 6.1. SEM of a) Cu-wire (0% Ag) electrodeposited with DAT, (b) CuAg-poly (6% Ag) electrodeposited without DAT, and (c) CuAg-wire (6% Ag) electrodeposited with DAT.

Cu and bimetallic CuAg samples with various quantities of Ag dopant were prepared by electrodeposition with and without the present of additive DAT. Previously we showed that electrodeposition of Cu in the presence of DAT at pH = 1.5 leads to a wire-like morphology for the Cu deposit, shown in Figure 6.1a. We wondered how added Ag might change the deposit morphology. Figure 6.1b shows a CuAg film (CuAg poly) containing nominally 6% Ag deposited without DAT in solution. The film exhibits large particles, similar to deposits reported previously. Addition of DAT to the Cu-Ag plating bath leads to a different morphology. Figure 6.1c shows a CuAg-wire deposit containing a nominal 6% Ag. The image shows the presence of wire-like

deposit exhibiting substantial porosity. The wires are approximately a factor of ~ 2 smaller in diameter relative to the deposit formed from Cu alone.

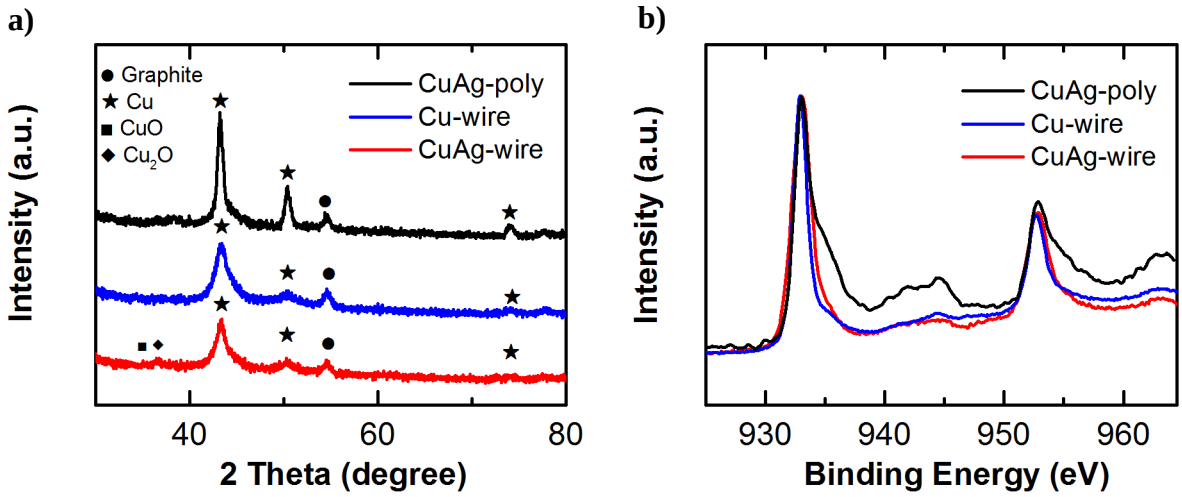

Figure 6.2. (a) XRD and (b) XPS patterns of CuAg-poly (6% Ag) electrodeposited without DAT, Cu-wire (0% Ag) electrodeposited with DAT, and CuAg-wire (6% Ag) electrodeposited with DAT.

Figure 6.2a shows XRD patterns obtained from CuAg-poly (6% Ag) electrodeposited without DAT, Cu-wire (0% Ag) electrodeposited with DAT, and CuAg-wire (6% Ag) electrodeposited with DAT. The XRD shows the presence of mostly metallic Cu with Cu peaks at $2\theta = 43.46^{o}$ (from Cu (111)), 50.62^{o} (from Cu (200)), and 74.40^{o} (from Cu (220)). No Ag-related peaks are found, due to the relatively small amount of Ag present. The CuAg-wire sample also exhibits a small peak at $2\theta = 36.95^{o}$ associated with the presence of Cu_2O. The Cu peaks in XRD patterns of CuAg-wire and Cu-wire samples are broader and lower intensity than that found in the Cu-poly sample, indicating that CuAgDAT and CuDAT samples exhibit a smaller crystallite size than Cu-poly. The crystallite size of CuAg, CuDAT, CuAgDAT samples calculated from XRD patterns using the Scherer equation are 21.1nm, 4.6 nm and 3.7 nm respectively, as given in Table 6.1.

Figure 6.2b shows the XPS patterns obtained from the CuAg, CuDAT, CuAgDAT samples. While CuDAT and CuAgDAT show only 2 main peaks of Cu (0), the CuAg poly material exhibits a series of satellite peaks[26-28] from CuO, suggesting that CuAg poly contains more oxide (at least on the surface) than the others. While the XRD reported on the presence of Cu_2O for the CuAg wire sample, peaks associated with Cu(I) are difficult to distinguish from those for Cu(0) in XPS.

Table 6.1. Parameters obtained from Cu and CuAg samples.

	$\frac{A_{active}}{A_{geometric}}$	Crystalline size nm	Loading mg/cm^2
CuAg	1.3	21.1	~0.5
CuDAT	7.3	4.6	~0.3
CuAgDAT-6%Ag	8.1	3.7	~0.3

The electro-active surface area of the different Cu and CuAg samples was measured by using Pb underpotential deposition (PbUPD) to form a conformal Pb coat on the accessible part of the Cu deposit[25,29] The results (Table 6.1) show that CuAg sample electrodeposited without DAT exhibits an electro-active surface area similar to the geometric area, as expected due to the large particles seen in the SEM. Alternatively, the Cu wire and CuAg (6%) wire samples exhibit electro-active surface area 7-8 times larger than geometric area. CuAg wire exhibits ~10% larger surface area than the Cu samples (Figure 6.1, Table 6.1).

Cu and Ag K-edge EXAFS and XANES spectra and analysis (Figure 6.3 and Table 1) were utilized to determine the local bonding environment of Cu and Ag in the samples containing Ag. The data shows that both CuAg-wire and CuAg-poly samples appear to be metallic since both the XANES spectra and Fourier transforms (FT) of EXAFS spectra for CuAg samples are similar to those for corresponding metallic foil.

For CuAg-poly samples, the contribution of Ag-Cu bonds to the total EXAFS spectra is not significant, and cannot be detected within the uncertainties of our analysis (Figure 6.3). The structure parameters of CuAg-poly (Table 6.2) that characterize the environment around Ag, as well as ΔE_0 parameter that characterizes the electronic state of Ag atoms within error bars coincide with those for bulk silver material. Similarly, the average interatomic distances of Cu-Cu are the same as in bulk copper metal. These findings indicate that Cu and Ag atoms are completely segregated in the CuAg-poly samples.

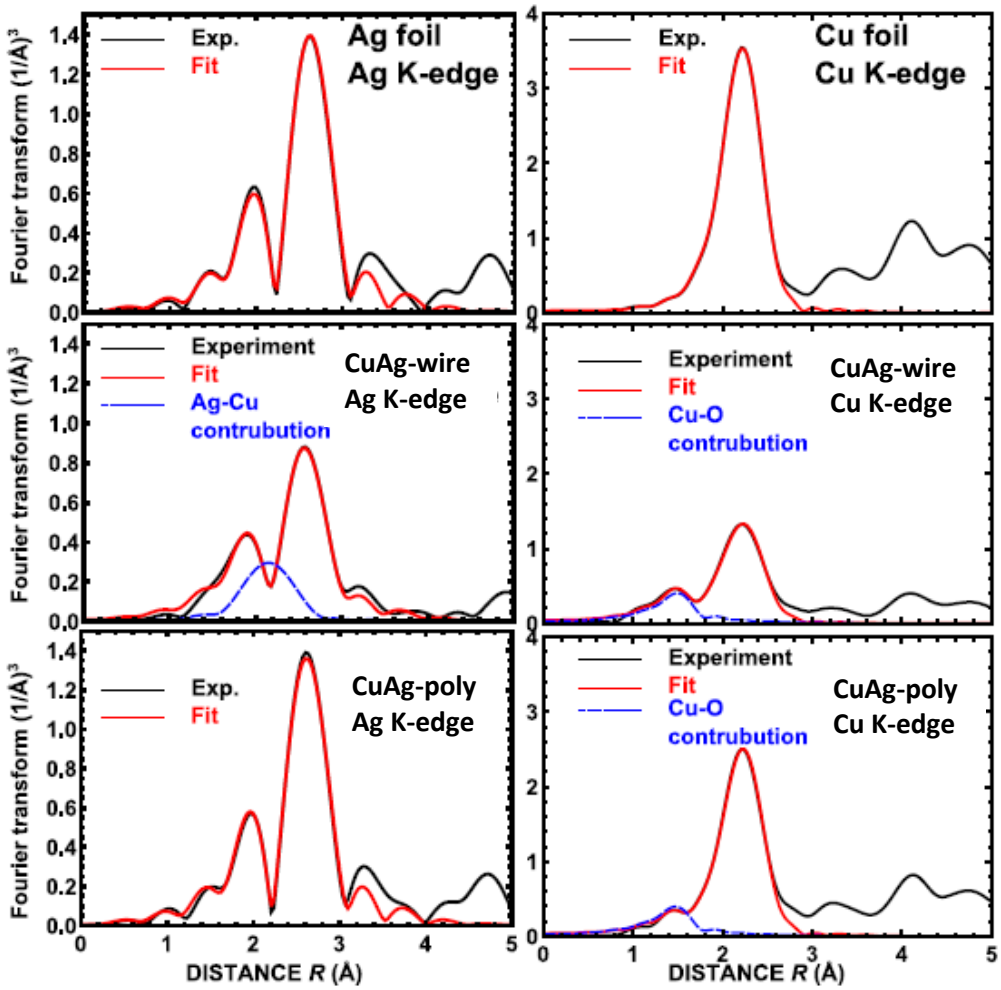

Figure 6.3. Best fit for Ag K-edge and Cu K-edge EXAFS data for CuAg-wire and CuAg-poly samples and Cu and Ag foils: Fourier transforms (FTs) for experimental and modelled EXAFS data.

CuAg-wire, in turn, exhibits Ag-Cu bonds (Figure 6.3) with distance value between those for pure copper and pure silver (Table 6.2), as expected for alloys. Also the Ag-Ag distance is slightly reduced in CuAg-wire sample, suggesting at least partial alloying of Ag atoms with smaller Cu atoms. The average interatomic distance for Cu-Cu is close to those in bulk material, which is reasonable with large contents of Cu comparing to Ag in the CuAg-wire samples.

Table 6.2. Values of structural parameters for the first coordination shell of Cu and Ag atoms in CuAg-wire and CuAg-poly samples, obtained from the fits of Cu K-edge and Ag K-edge EXAFS data.

	Ag foil	Cu foil	CuAgDAT	CuAg
ΔE_0 (ev), Ag K-edge	-8.6(1)	-	-10.2(4)	-8.8(1)
ΔE_0 (ev), Cu K-edge	-1.1(4)	-	0.5(6)	-0.4(5)
$N_{\text{Ag-Ag}}$	12		11.0(4)	12
$N_{\text{Ag-Cu}}$	-	-	2.0(6)	0
$N_{\text{Cu-Cu}}$	-	12	4.6(2)	8.6(4)
$N_{\text{Cu-O}}$	-	-	0.8(1)	0.4(2)
$\langle R \rangle_{\text{Ag-Ag}}$ (Å)	2.864(1)	-	2.822(6)	2.858(2)
$\langle R \rangle_{\text{Ag-Cu}}$ (Å)	-	-	2.641(7)	-
$\langle R \rangle_{\text{Cu-Cu}}$ (Å)	-	2.537(2)	2.542(4)	2.540(4)
$\langle R \rangle_{\text{Cu-O}}$ (Å)	-	-	1.87(1)	1.85(2)
$\sigma^2_{\text{Ag-Ag}}$ (Å^2)	0.0104(2)	-	0.0156(8)	0.0106(1)
$\sigma^2_{\text{Ag-Cu}}$ (Å^2)	-	-	0.011(4)	-
$\sigma^2_{\text{Cu-Cu}}$ (Å^2)	-	0.0086(2)	0.0087(5)	0.0086(4)
$\sigma^2_{\text{Cu-O}}$ (Å^2)	-	-	0.003(2)	0.003(5)

6.3.2. CO_2 reduction in flow cell

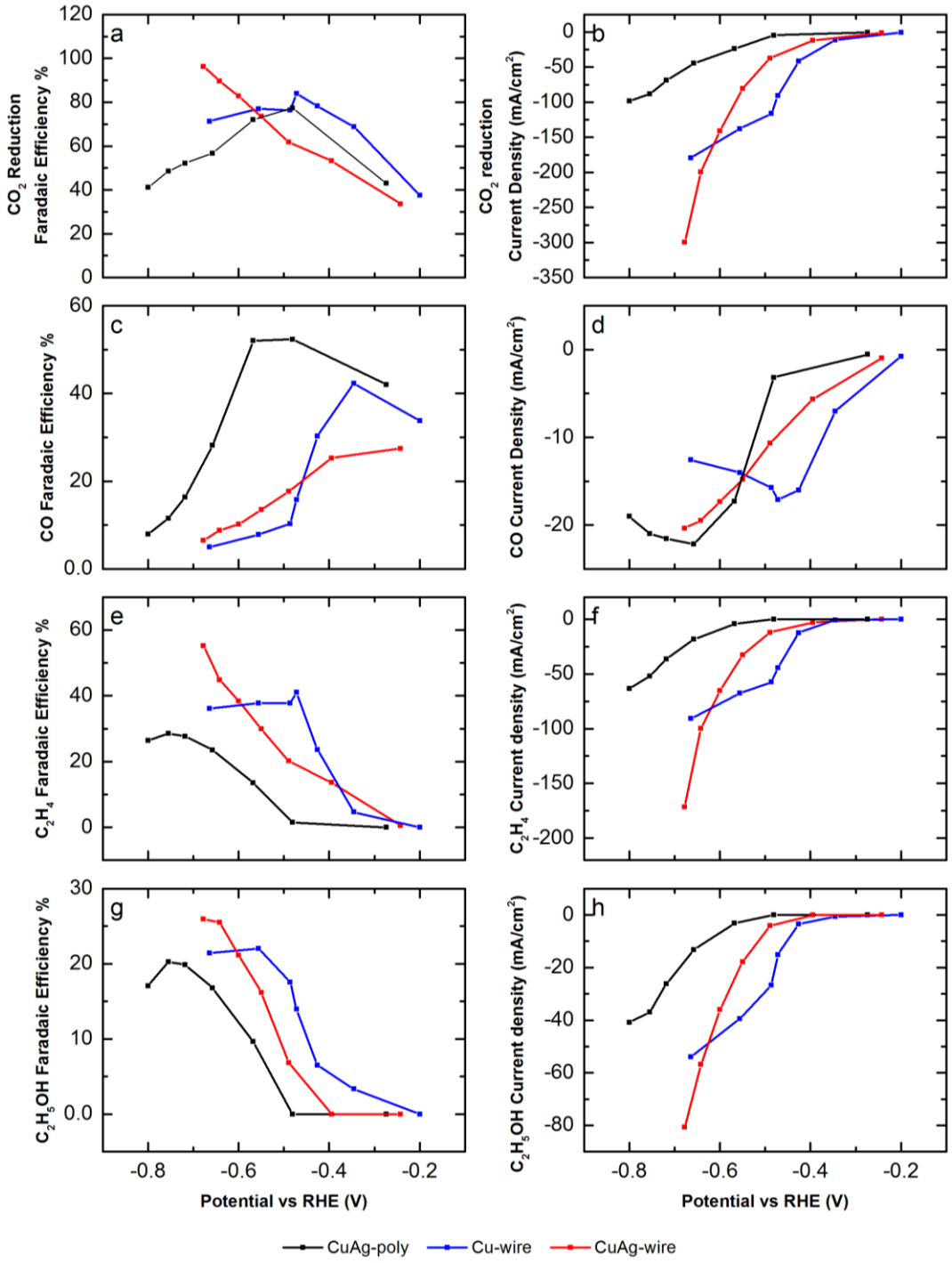

Figure 6.4. Faradaic efficiencies and corresponding current densities for (a,b) total CO_2 reduction, (c,d) CO production, (e,f) C_2H_4 production, and (g,h) C_2H_6OH production from CuAg-poly (6% Ag) (black), Cu-wire (0% Ag), and CuAg-wire (6% Ag)samples.

To evaluate the catalytic activity and product distribution during CO_2 reduction of Cu and CuAg samples, we also tested them in a flow electrolysis system. Figure 6.4 shows Faradaic efficiency (FE) and partial current density for CO_2 reduction reaction and all major products (CO, C_2H_4, and C_2H_5OH) using CuAg-poly electrodeposited without DAT, Cu-wire (0% Ag) electrodeposited with DAT and CuAg-wire (6% Ag) electrodeposited with DAT in a 1 M KOH electrolyte as a function of cathode potential.

Figure 6.4a-b show that, the Cu-wire and CuAg-wire electrodeposited with DAT exhibits ~ 5-6 times higher CO_2 reduction current densities than that from CuAg-poly electrodeposited without DAT. This enhancement in activity could be explained by differences in their surface areas (Table 6.1). Particularly, CO_2 reduction current densities of CuAg-poly, Cu-wire and CuAg-wire at ~ -0.7V are ~ -50 mA/cm^2, ~-180 mA/ cm^2, and ~-300 mA/ cm^2, respectively. Interestingly, while the active surface area of CuAg-wire is only ~ 10% higher than that of Cu-wire (Table 6.1), the current density of CuAg-wire is ~ 60% higher than that obtained from Cu-wire. This phenomenon suggests that differences in active surface area is not the only reason for enhancement in CO_2 reduction activity between Cu-wire and CuAg-wire.

Figure 6.4c-d show that for all catalysts, CO formation starts at ~ -0.2V vs. RHE. The FE for CO production decreases with increases of the FEs associated with C2 products including C_2H_4 (Figure 6.4e-f) and C_2H_5OH (Figure 6.4g-h). A possible explanation for this trend is that adsorbed CO is an important intermediate for the formation of C2 products, as has been suggested previously.[7,8,11,30-32]

Figure 6.4e-h show that CuAg-poly samples exhibit lowest Faradaic efficiency and current density for C_2 formation among CuAg-poly, Cu-wire and CuAg-wire, which probably can be explained by the effect of 'nanosize' Cu-wire and CuAg-wire particles. The nano porous surfaces

of Cu-wire and CuAg-wire give rise to steps and edges with low-coordinated metal atoms which have been postulated to be more active toward the reduction of CO_2 to C2 products: Steps and edges promote adsorption of C1 intermediates and facilitate their dimerization to form C2 products.[8,9,31,33-35]

Figure 6.4e-h also show that both Cu-wire and CuAg-wire exhibit high Faradaic efficiency and current density for C_2 formation. While Cu-wire samples reach 40% FE for C_2H_4 and 20% FE for C_2H_5OH at relatively low potential (~ -0.5V vs. RHE), the FE maintains at this level even at more negative potential. On the other hand, the CuAg-wire reach the same FE for C2 products at ~ -0.6 V vs. RHE, their FE continuously increases with increasing negative potential. Consequently, at high negative potential, CuAg-wire exhibits higher activity and selectivity for C2 products (C_2H_4 and C_2H_5OH) than those obtained from Cu-wire. Particularly, at ~ -0.7 V vs. RHE, the FE for C_2H_4 of CuAg-wire (~ 60%) is higher than that of Cu-wire (~ 40%), and the current density for C_2H_4 of CuAg-wire (~180 mA/cm^2) is approximately a factor of ~ 2 higher than that obtained from Cu-wire (~90 mA/cm^2). Similarly, at ~ -0.7 V vs. RHE, the FE for C_2H_5OH of CuAg-wire (~ 25%) is higher than that of Cu-wire (~ 20%), and the current density for C_2H_5OH of CuAg-wire (~80 mA/cm^2) is higher than that obtained from Cu-wire (~55 mA/cm^2).

6.4. Conclusion

In this work, we developed a facile method to co-electrodeposit high surface area CuAg alloys, resulting from the inhibition of nucleation through the presence of an additive, DAT. EXAFS data demonstrated that while Cu and Ag atoms in CuAg-poly samples that are electrodeposited without DAT are completely segregated, those in CuAg-wire samples are more

homogeneously mixed. Flow cell experiments show that the CuAg-wire samples exhibit higher high activity and selectivity of CO_2 reduction to C2 products (C_2H_4 and C_2H_5OH) than CuAg-poly and Cu-wire samples.

6.5. References

(1) Whipple, D. T.; Kenis, P. J. A. *Journal of Physical Chemistry Letters* **2010**, *1*, 3451-3458.

(2) Yang, H.; Xu, Z.; Fan, M.; Gupta, R.; Slimane, R. B.; Bland, A. E.; Wright, I. *Journal of Environmental Sciences-China* **2008**, *20*, 14-27.

(3) Appel, A. M.; Bercaw, J. E.; Bocarsly, A. B.; Dobbek, H.; DuBois, D. L.; Dupuis, M.; Ferry, J. G.; Fujita, E.; Hille, R.; Kenis, P. J. A.; Kerfeld, C. A.; Morris, R. H.; Peden, C. H. F.; Portis, A. R.; Ragsdale, S. W.; Rauchfuss, T. B.; Reek, J. N. H.; Seefeldt, L. C.; Thauer, R. K.; Waldrop, G. L. *Chemical Reviews* **2013**, *113*, 6621-6658.

(4) Olah, G. A.; Prakash, G. K. S.; Goeppert, A. *Journal of the American Chemical Society* **2011**, *133*, 12881-12898.

(5) Costentin, C.; Robert, M.; Saveant, J.-M. *Chemical Society Reviews* **2013**, *42*, 2423-2436.

(6) Lim, R. J.; Xie, M. S.; Sk, M. A.; Lee, J. M.; Fisher, A.; Wang, X.; Lim, K. H. *Catalysis Today* **2014**, *233*, 169-180.

(7) Kortlever, R.; Shen, J.; Schouten, K. J. P.; Calle-Vallejo, F.; Koper, M. T. M. *Journal of Physical Chemistry Letters* **2015**, *6*, 4073-4082.

(8) Hori, Y. In *Modern Aspects of Electrochemistry*; Vayenas, C. G., White, R. E., Gamboa-Aldeco, M. E., Eds.; Springer New York: New York, NY, 2008, p 89-189.

(9) Tang, W.; Peterson, A. A.; Varela, A. S.; Jovanov, Z. P.; Bech, L.; Durand, W. J.; Dahl, S.; Norskov, J. K.; Chorkendorff, I. *Physical Chemistry Chemical Physics* **2012**, *14*, 76-81.

(10) Kas, R.; Hummadi, K. K.; Kortlever, R.; de Wit, P.; Milbrat, A.; Luiten-Olieman, M. W. J.; Benes, N. E.; Koper, M. T. M.; Mul, G. *Nature Communications* **2016**, *7*.

(11) Ma, S. C.; Sadakiyo, M.; Luo, R.; Heima, M.; Yamauchi, M.; Kenis, P. J. A. *Journal of Power Sources* **2016**, *301*, 219-228.

(12) Kas, R.; Kortlever, R.; Milbrat, A.; Koper, M. T. M.; Mul, G.; Baltrusaitis, J. *Physical Chemistry Chemical Physics* **2014**, *16*, 12194-12201.

(13) Li, C. W.; Kanan, M. W. *Journal of the American Chemical Society* **2012**, *134*, 7231-7234.

(14) Manthiram, K.; Beberwyck, B. J.; Aivisatos, A. P. *Journal of the American Chemical Society* **2014**, *136*, 13319-13325.

(15) Mistry, H.; Varela, A. S.; Bonifacio, C. S.; Zegkinoglou, I.; Sinev, I.; Choi, Y. W.; Kisslinger, K.; Stach, E. A.; Yang, J. C.; Strasser, P.; Cuenya, B. R. *Nature Communications* **2016**, *7*.

(16) Ma, M.; Djanashvili, K.; Smith, W. A. *Angewandte Chemie-International Edition* **2016**, *55*, 6679-6683.

(17) Ren, D.; Ang, B. S.-H.; Yeo, B. S. *Acs Catalysis* **2016**, 8239-8247.

(18) Choi, J.; Kim, M. J.; Ahn, S. H.; Choi, I.; Jang, J. H.; Ham, Y. S.; Kim, J. J.; Kim, S. K. *Chemical Engineering Journal* **2016**, *299*, 37-44.

(19) Kim, D.; Resasco, J.; Yu, Y.; Asiri, A. M.; Yang, P. D. *Nature Communications* **2014**, *5*.

(20) Christophe, J.; Doneux, T.; Buess-Herman, C. *Electrocatalysis* **2012**, *3*, 139-146.

(21) Mistry, H.; Varela, A. S.; Bonifacio, C. S.; Zegkinoglou, I.; Sinev, I.; Choi, Y. W.; Kisslinger, K.; Stach, E. A.; Yang, J. C.; Strasser, P.; Cuenya, B. R. *Nature Communications* **2016**, *7*.

(22) Schouten, K. J. P.; Qin, Z. S.; Gallent, E. P.; Koper, M. T. M. *Journal of the American Chemical Society* **2012**, *134*, 9864-9867.

(23) Hori, Y.; Takahashi, I.; Koga, O.; Hoshi, N. *Journal of Molecular Catalysis A: Chemical* **2003**, *199*, 39-47.

(24) Watanabe, M.; Shibata, M.; Kato, A.; Azuma, M.; Sakata, T. *Journal of the Electrochemical Society* **1991**, *138*, 3382-3389.

(25) Wu, G. Y.; Bae, S. E.; Gewirth, A. A.; Gray, J.; Zhu, X. D.; Moffat, T. P.; Schwarzacher, W. *Surface Science* **2007**, *601*, 1886-1891.

(26) Biesinger, M. C.; Lau, L. W. M.; Gerson, A. R.; Smart, R. S. C. *Applied Surface Science* **2010**, *257*, 887-898.

(27) Zhu, C. Q.; Osherov, A.; Panzer, M. J. *Electrochimica Acta* **2013**, *111*, 771-778.

(28) Yin, M.; Wu, C. K.; Lou, Y. B.; Burda, C.; Koberstein, J. T.; Zhu, Y. M.; O'Brien, S. *Journal of the American Chemical Society* **2005**, *127*, 9506-9511.

(29) Yu, L.; Akolkar, R. *Journal of the Electrochemical Society* **2016**, *163*, D247-D249.

(30) Kuhl, K. P.; Cave, E. R.; Abram, D. N.; Jaramillo, T. F. *Energy & Environmental Science* **2012**, *5*, 7050-7059.

(31) Schouten, K. J. P.; Kwon, Y.; van der Ham, C. J. M.; Qin, Z.; Koper, M. T. M. *Chemical Science* **2011**, *2*, 1902-1909.

(32) Montoya, J. H.; Shi, C.; Chan, K.; Norskov, J. K. *Journal of Physical Chemistry Letters* **2015**, *6*, 2032-2037.

(33) Ren, D.; Deng, Y. L.; Handoko, A. D.; Chen, C. S.; Malkhandi, S.; Yeo, B. S. *Acs Catalysis* **2015**, *5*, 2814-2821.

(34) Durand, W. J.; Peterson, A. A.; Studt, F.; Abild-Pedersen, F.; Norskov, J. K. *Surface Science* **2011**, *605*, 1354-1359.

(35) Hori, Y.; Takahashi, I.; Koga, O.; Hoshi, N. *Journal of Molecular Catalysis a-Chemical* **2003**, *199*, 39-47.

Appendix A

Experimental procedures and cell designs

A.1. Cantilever fabrication

Cantilevers used for stress measurements (Chapter 2), and for electrochemical experiments (Chapter 3, 4, 5) were fabricated from glass microscope cover-slips modified on one side by physical vapor deposition (electron beam deposition or sputter deposition) of Ti (as adhesion layer) followed by the metal of interest (Au, Ni or Cu). Glass microscope cover-slips were obtained from Gold Seal No.1, 150 µm thick and used without further cleaning. Glass cover-slips were secured to sample holders by carbon tape.

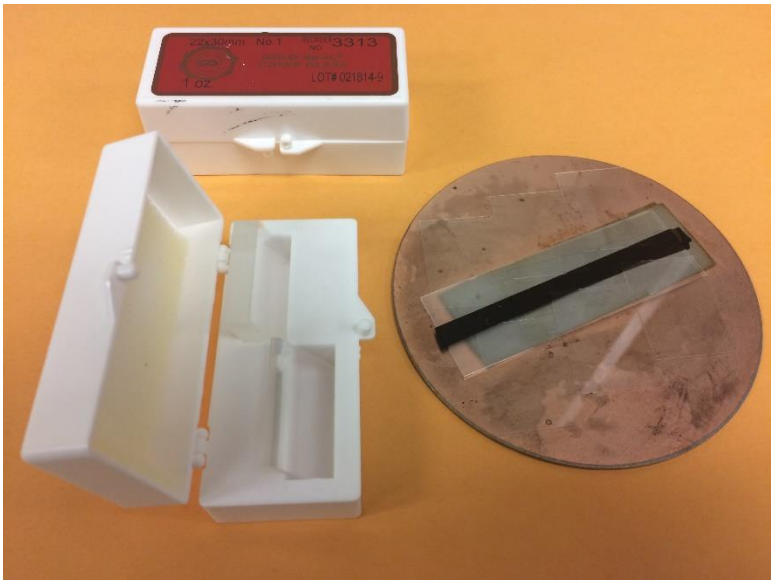

Figure A.1. Glass microscope cover-slips (Gold Seal No.1, 150 µm thick).

Au, Ni and Cu cantilevers were fabricated by electron beam deposition using the "E-beam evaporator 2" instrument in the Material research lab (MRL). First, Ti, as an adhesion layer

between glass substrate and the metal of interest, was e-beamed at deposition rate of 0.3 Å/s until reaching 20 nm thickness. Then Au, or Ni, or Cu was e-beamed at rate of 0.3 Å/s for first 10 nm, then increased to 0.5 Å/s until the desired thickness was achieved (100-150 nm). After the ebeam process, cantilevers were cooled down in the deposition chamber for at least 30 minutes before they were exposed to air (to prevent oxidation process of metal at high temperature).

Pt cantilevers were fabricated by DC magnetron sputter using "AJA Sputter Coater 2" instrument in MRL with the following parameter: sample height = 30 mm, rotation rate 50 rpm, Ar gas flow = 3 sccm, baratron gauge pressure = 3 mTorr. Ti, as an adhesion layer, was sputtered at 100 W with 5 mins of pre-sputter (shutter was closed) and 10 mins of sputter (shutter was open). The thickness of Ti layer was ~ 10 nm. Pt was sputtered at 35 W with 5 mins of pre-sputter and 20 mins of sputter. The thickness of Pt layer was ~ 100 nm. After sputtered, cantilevers were cooled down in the deposition chamber for at least 30 minutes before they were exposed to air.

A.2. Electrodeposition with DAT additive

A.2.1. Electrodeposition of Ni and NiFe in sulfate bath with DAT additive

Ni, NiFe, and Co were electrodeposited galvanostatically at a constant current density of -4 mA/cm^2 until a final deposition charge was reached (typically 2 C/cm^2, unless otherwise stated). A 10 sec resting time after passage of each 0.8 - 1 C/cm^2 was applied in order to minimize formation of deleterious concentration gradients. Au, Pt, Ni foil, Ni foam, stainless steel, and Fluorine-doped Tin Oxide (FTO) were used as the deposition substrates. Pt or glassy carbon were used as counter electrodes and separated from the working electrode by a glass frit in an

electrochemical H-cell (Figure A.2). A 'leakless' Ag/AgCl (eDAQ) electrode was placed near the working to measure the deposition potential.

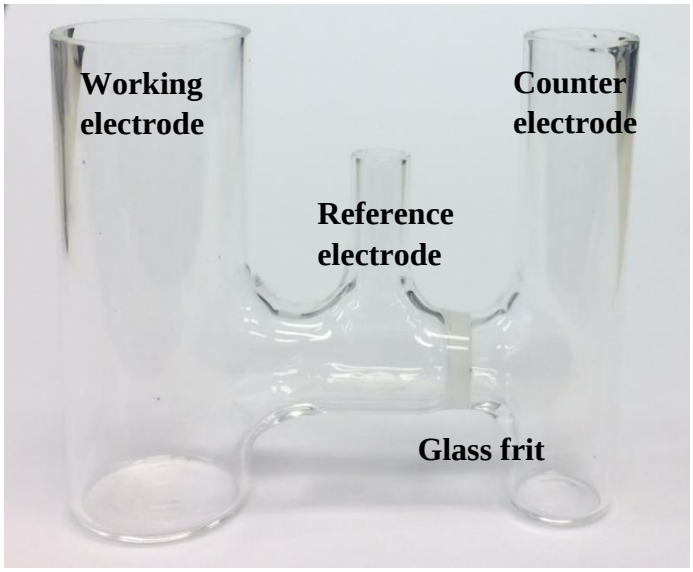

Figure A.2. Electrochemical H-cell with a glass frit for electrodeposition.

Substrates for electrodeposition were cleaned just before used. Au (200 nm thickness, fabricated on one side of glass coverslips by e-beam deposition) was rinsed with Milli-Q water, and then flamed under H_2. Stainless steel disk was mechanically polished with sand paper, immersed in 0.1 M H_2SO_4 for 2 minutes to remove the native oxide layer, and then rinsed thoroughly with Milli-Q water. Ni foil (Sigma Aldrich, thickness 0.125 mm, purity 99.9%) and Ni foam (MTI corporation, purity 99.99%, density 346 g/m^2, 80-110 pores per inch, average hole diameter 0.25mm) were immersed in 0.1 M H_2SO_4 for 2 minutes to remove the native oxide layer, and then rinsed thoroughly with Milli-Q water. Deposition current was calculated from the geometric area of each substrate, which was typically ~ 1 cm^2. Each deposition bath contained typically ~ 15 ml solution.

The Ni plating baths were made from 0.5 M $NiSO_4.6H_2O$ + 0.4 M H_3BO_3 adjusted to pH 3 with H_2SO_4 and plating was performed either without an additive, or with 4 mM of 3,5-diamino-1,2,4-triazole (DAT), 10 mM of 3-Amino-1,2,4-triazole (AT), or 30 mM of 1,2,4-triazole-3,4,5-

triamine (TAT). The Ni and NiFe plating baths were made from (0.5 M - 0.25 M) $NiSO_4.6H_2O$ + 0.4 M H_3BO_3 + $FeSO_4.7H_2O$ (0 M - 0.25 M), adjusted to pH 3 with H_2SO_4 and plating was performed either without an additive, or with 3,5-diamino-1,2,4-triazole (DAT). Concentration of metal ions (Ni^{2+} and Fe^{2+}) in deposition solutions equaled to 0.5 M in total. The Co plating baths were made from 0.5 M $CoSO_4.7H_2O$ + 0.4 M H_3BO_3, adjusted to pH 3 with H_2SO_4 and plating was performed either without an additive, or with 4 mM of 3,5-diamino-1,2,4-triazole (DAT).

A.2.2. Electrodeposition of Cu in sulfate bath with DAT additive

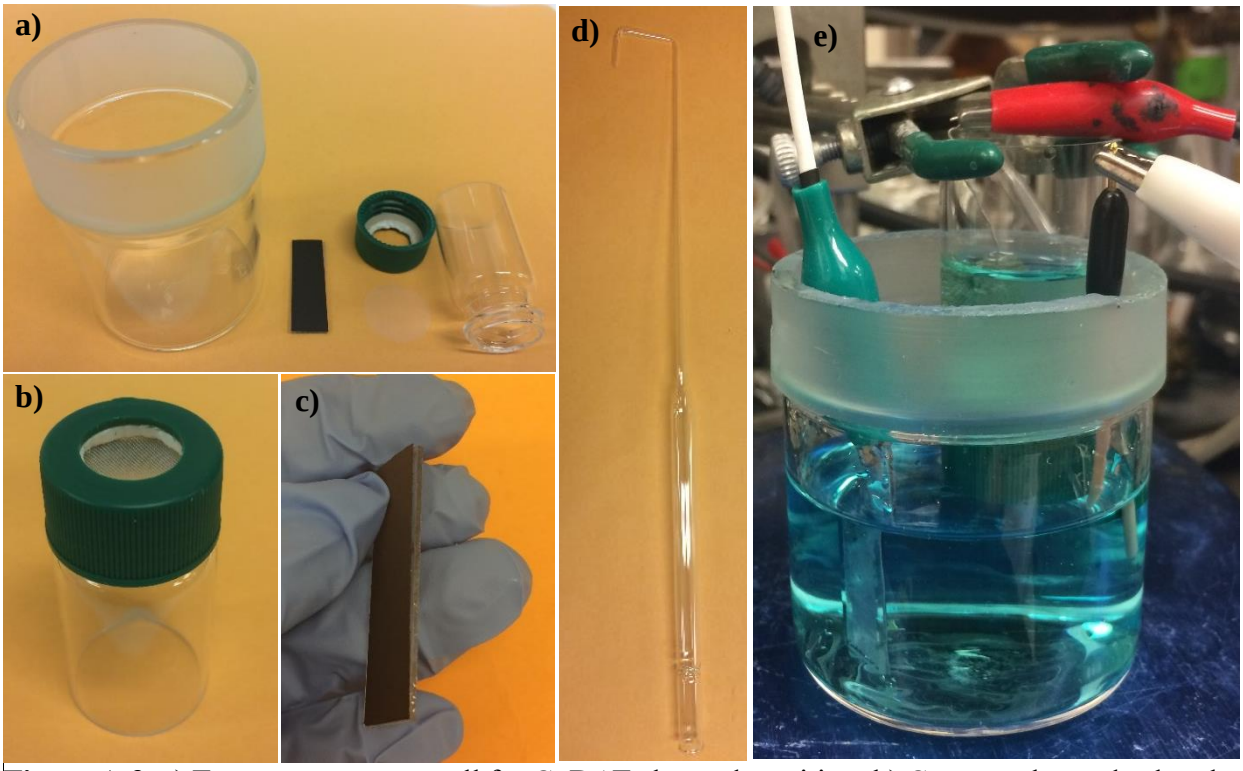

Figure A.3. a) Two-compartment cell for CuDAT electrodeposition, b) Counter electrode chamber with anion-exchange membrane, c) Carbon electrode taped on a piece of glass slide, d) hooked pipet to remove bubble trapped between 2 chambers, d) Electrochemical set up for CuDAT electrodeposition.

The Cu plating baths were made from 0.1 M $CuSO_4.5H_2O$ and 10 mM of 3,5-diamino-1,2,4-triazole (DAT) additive, pH adjusted between pH 1-3 by using H_2SO_4. Cu was electrodeposited galvanostatically at a constant current density ranging from 1 - 4 mA/cm^2 until a final deposition charge was reached (typically 2 C/cm^2, unless otherwise stated). Pt wire was used as the counter electrode. The counter electrode was separated from the working electrode by using an ion exchange membrane (Fumatech® FAP-375-PP) in a two compartment electrochemical cell to avoid oxidation of additives at the counter electrode (Figure A.3). A 'leakless' Ag/AgCl (eDAQ) electrode was placed near the working electrode to measure the potential.

Substrates for electrodeposition were cleaned just before used. Au (200 nm thickness, fabricated on one side of glass coverslips by e-beam deposition) was rinsed with Milli-Q water, and then flamed under H_2. Cu foil (Sigma Aldrich, thickness 0.125 mm, purity 99.9) was rinsed thoroughly with Milli-Q water. Carbon paper (GDL, Sigracet 35 BC, Ion Power) was activated either by immersing in conc. HNO_3 for 1h or electron beam coated with ~ 10 nm of Cu (~ 0.01 mg/cm^2). Carbon paper was used immediately after pretreated either by HNO_3 or e-beam or sputter. Carbon paper pretreated by both methods exhibits similar morphologies and electrochemical activities.

For flow cell electrolysis experiments, Cu was electrodeposited on carbon paper and used as a gas diffusion electrode. However, HNO_3 treatment makes both side of the carbon paper become hydrophilic and allows liquid to easily pass through, which causes flooding of electrolyte into the gas chamber. Thus, the carbon paper was sputter coated with Cu instead of treated with HNO_3 before electrodeposition. Then 2 C/cm^2 of Cu was electrodeposited on the 1 × 2.5 cm^2 section of carbon paper.

A.2.3 General notes for electrodeposition with DAT additive to fabricate nanoporous film

Formation of nanoporous deposit from DAT deposition bath could be explained by diffusion-limited aggregation growth in which nano structures occur when the material accretion onto the surface is limited by diffusion, and deposition occurs preferentially on protuberances. It is importance to avoid the presence of any other factors that could affect diffusion of metal ions in the deposition bath.

The presence of strong accelerator factors in the deposition bath, such as Cl^-, stirring, and high temperature, can counter the inhibition effects of DAT and lead to smooth metal film. Therefore, there should be no heating, stirring solution or moving electrodes during the electrodeposition process. Deposition solutions after sonicated need to be cooled down to room temperature before using. A 'leakless' Ag/AgCl (eDAQ) reference electrode is used instead of conventional Ag/AgCl to avoid Cl^- contamination.

NO_3^- if presenting in the deposition bath will cause the formation of unwanted metal hydroxides from metal ions near the electrode and OH^- produced during NO_3^- reduction. Therefore, glassware for electrodeposition should not be cleaned in HNO_3 bath. The glassware should be cleaned in a bath of H_2SO_4 with Nochromix for at least 2 hours, then rinsed thoroughly with DI water and boiling MiliQ water.

Fumatech anion-exchange membrane is used to separate counter electrode from the main deposition chamber, avoiding DAT to be oxidized at the counter. Fumatech® FAP-375-PP membrane, which has no counter ion, is used instead of other membranes with Cl^- or Br^- counter ions to avoid the contamination.